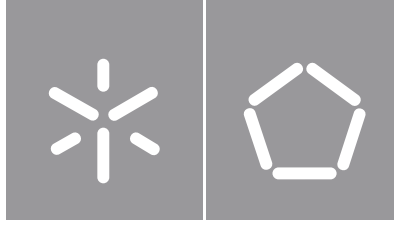Universidade do Minho
Escola de Engenharia

Edward Alexis Baron Corredor

Structural damage identification for
robustness assessment of railway
infrastructure under flood effects

Structural damage identification for robustness assessment of railway infrastructure under flood effects

Edward Alexis Baron Corredor

UMinho | 2022

Universidade do Minho
Escola de Engenharia

Edward Alexis Baron Corredor

Structural damage identification for robustness assessment of railway infrastructure under flood effects

Tese de Doutoramento
Doutoramento em Engenharia Civil
Engenharia Civil

Trabalho efetuado sob a orientação do(a)
Professor Doutor José António Campos e Matos
Professor Doutor Rui Artur Bartolo Calçada
Professor Doutor Kenneth Gavin

janeiro de 2023

DIREITOS DE AUTOR E CONDIÇÕES DE UTILIZAÇÃO DO TRABALHO POR TERCEIROS

Este é um trabalho académico que pode ser utilizado por terceiros desde que respeitadas as regras e boas práticas internacionalmente aceites, no que concerne aos direitos de autor e direitos conexos. Assim, o presente trabalho pode ser utilizado nos termos previstos na licença abaixo indicada. Caso o utilizador necessite de permissão para poder fazer um uso do trabalho em condições não previstas no licenciamento indicado, deverá contactar o autor, através do RepositóriUM da Universidade do Minho.

ACKNOWLEDGMENTS

FINANCIAL SUPPORT

Cofinanciado por:

STATEMENT OF INTEGRITY

I hereby declare having conducted this academic work with integrity. I confirm that I have not used plagiarism or any form of undue use of information or falsification of results along the process leading to its elaboration.

I further declare that I have fully acknowledged the Code of Ethical Conduct of the University of Minho.

RESUMO

Devido à importância das infraestruturas ferroviárias na Europa, sejam económicas ou culturais, vários investimentos têm sido feitos para melhorar as atuais redes. Um desses investimentos está no programa Shift2Rail, que tem como objetivo a gestão de ativos de estruturas de alta capacidade com precisão e confiabilidade. Atingir este objetivo principal é priorizado por métodos inovadores para determinar a segurança e prolongar a vida útil da infraestrutura ferroviária. A partir desta perspetiva, esta investigação apresenta uma estrutura de trabalho de uma metodologia baseada em modelos substitutos para uma avaliação de robustez de pontes ferroviárias com o objetivo de analisar o tipo de ponte mais padrão na Europa e a causa comum da falha estrutural, priorizando a simplificação da coleta de dados e cálculos computacionais enquanto se concentra em complexidades específicas da análise da estrutura. Para tal foram desenvolvidas quatro vertentes de trabalho: i) avaliação do risco de inundação, que entre todos os perigos conhecidos para pontes, os efeitos das inundações são a principal causa de colapso para este tipo de estrutura. Por esta razão, a estimativa de risco tem o objetivo de desenvolver um modelo hidráulico alimentado por uma metodologia de machine learning capaz de modelar variáveis hidrológicas considerando as incertezas das mudanças climáticas. ii) A análise de falhas de pontes considera os diferentes efeitos das inundações que causam diferentes mecanismos de colapso. Portanto, uma visão geral da interação ponte-inundação foi feita em relação aos problemas estruturais e geotécnicos para quantificar a causa e o tipo de falha. iii) A análise estrutural não linear tem o objetivo de apresentar uma abordagem de modelagem usando diferentes elementos 2D e 3D do software DIANA FEA, permitindo um alto grau de detalhamento na análise não linear. iv) A avaliação de robustez apresenta uma aplicação de uma metodologia baseada em modelos substitutos para obter a probabilidade de falha na estimativa de um indicador de robustez do perigo estudado. Consequentemente, a estrutura de trabalho proposta é aplicada a uma ponte em arco de pedra existente em Portugal para testar a sua eficiência, precisão e aplicabilidade.

Palavras-chave: avaliação de pontes; modelagem substituta; alterações climáticas; infraescavação; confiabilidade estrutural.

ABSTRACT

Due to the importance of railway infrastructure in Europe, whether economically or culturally, several investments have been made to improve the existing networks. One of these investments is taking place within the Shift2Rail program, which aims at the asset management of high-capacity structures with accuracy and reliability. The achievement of this main objective is prioritized by innovative methods to determine the safety and extend the life of railway infrastructures. From this perspective, this research presents a framework of a surrogate model- based methodology for a robustness assessment of railway bridges, aiming to analyze the most common bridge type and causes of failure in Europe, prioritizing the simplification of data collection and computational effort, while focusing on specific complexities of structural analysis. To achieve this, four workstreams have been developed: i) Flood hazard assessment, which is the main cause of collapse of this type of structures among all known hazards for bridges. For this reason, the hazard assessment aims to develop a hydraulic model fed by a machine learning method capable of modeling hydrological variables, considering the uncertainties of climate change. ii) The analysis of bridge failure considers the different effects of flooding that cause different collapse mechanisms. Therefore, an overview of the interaction between flooding and the bridge in terms of structural and geotechnical problems has been made in order to quantify the cause and nature of the failure. iii) The nonlinear structural analysis aims to present a modeling approach using different 2D and 3D elements of the software DIANA FEA that allows a high level of detail of the structural behavior. iv) Robustness evaluation presents an application of a surrogate model based methodology to obtain the probability of failure and estimate a robustness indicator for the hazard under study. Consequently, the proposed framework is applied to an existing stone arch bridge in Portugal to test its efficiency, accuracy, and applicability.

Keywords: bridge assessment; surrogate modeling; climate change; scour; structural reliability.

LIST OF CONTENTS

LIST OF FIGURES

LIST OF TABLES

INTRODUCTION

1.1 BACKGROUND AND MOTIVATION

The transport network is highly significant to the socio-economic development of a country. Therefore, the European Commission has a vision for European transport to overcome current societal issues such as increasing transport demand, congestion, energy security and climate change. To achieve a more competitive and resource-efficient transport system, an innovative, sustainable, and inclusive growth strategy is needed. In the case of rail transport, great progress has been made in the creation of a Single European Railway Area, focusing on three areas that make it possible to remove the obstacles that hinder the rail sector: i) the opening of the domestic passenger transport market, ii) infrastructure management, and iii) interoperability and safety. Therefore, several investments in railway infrastructure have been made across Europe. One of these investments is under the Shift2Rail program, where their resources are dedicated to the development, integration, demonstration, and validation of innovative rail technologies and solutions for the rail sector in Europe [1]. The Shift2Rail program aims at asset management of high-capacity structures with high accuracy and reliability. This main objective can be achieved by innovating the current methods for determining the safety and extending the service life of rail infrastructures (e.g., tracks and bridges).

Rail transportation expends approximately one-third of its operating costs on infrastructure. For instance, in 2012, EU member states spent between EUR 29 billion and EUR 34 billion on

rail infrastructure. Most of these costs are related to maintenance. However, interventions are also required when components fail, which can be particularly costly and disruptive. In addition, the expected growth (passenger and freight traffic) and aging of the existing infrastructure will significantly increase costs and maintenance requirements in the coming years [1], [2].

Public information on railway transport provided by the European Commission offers general statistics on freight, transport of people, traffic, transport safety, business, employment, infrastructure, and equipment. Nevertheless, the current demographics of rail bridges have yet to be determined due to their importance to the rail network. For this reason, the Sustainable Bridges project technical report produced a survey that estimated the total number of railway bridges in the European Union at 220,000. Figure 1 summarizes the statistics by bridge type, age profile, and span profile [3].
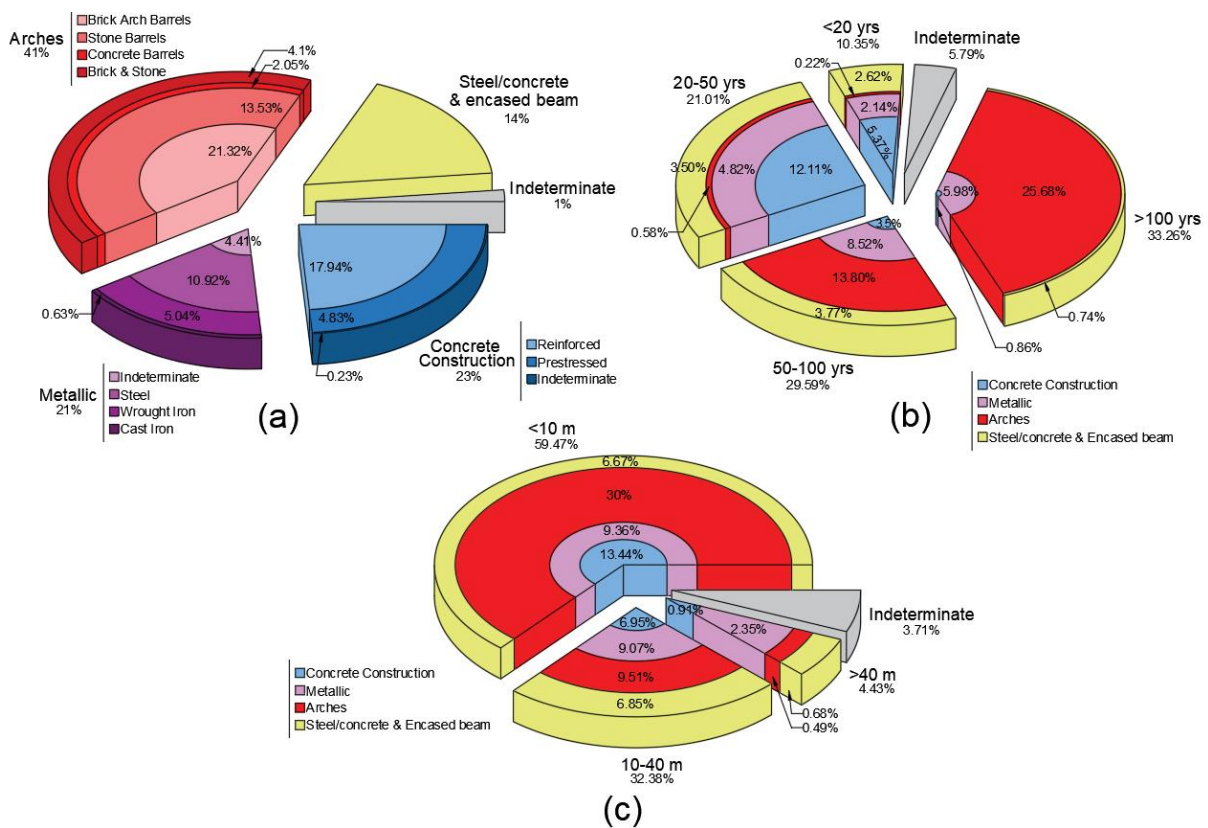
Figure 1. Demography of European railway bridges. (a) Types of bridges. (b) Age structure of bridges. (c) Bridge span profile.

To ensure the lifetime and safety of railway bridges, it is crucial to determine the most common cause of failure. For example, flooding is responsible for about 14% of global bridge

collapses between 1966 and 2016, based on data collected from WC1 members, COST action TU 1406 members, IABSE (International Association for Bridge and Structural Engineering) members, and other respondents (see Figure 2). In recent years, the damage caused by floods is a relevant problem due to the frequency of occurrence, resulting in economic losses and human fatalities, which are the most common impacts [4].

(a)   (b)
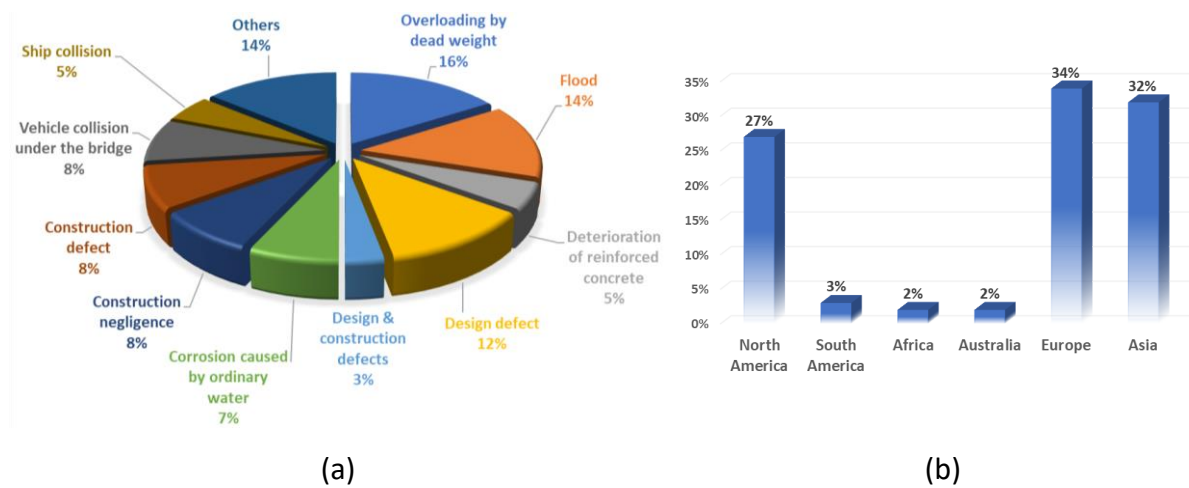
Figure 2. Statistics of bridge collapses between 1966 and 2016. (a) Causes of failure. (b) Continental distribution.

According to Proske [5], collapses caused by flooding contribute to almost 40% of collapses in the United States, a conclusion based on several publications summarizing the relative frequency of collapses. Figure 3 illustrates the histogram results related to the principal causes of bridge collapses [6]–[14].
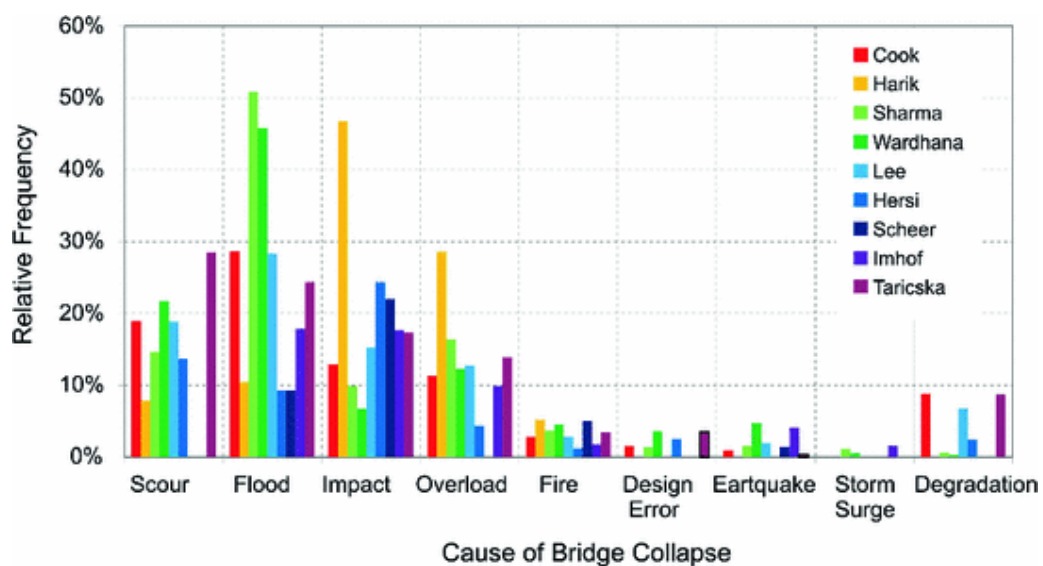
Figure 3. Causes of bridge failures in the USA as identified by different authors. Image adapted from [5].

Smith [15] presented a study of 143 bridges that had collapsed between 1847 and 1975 and classified the causes of collapse into nine categories. In this database, 77 of the collapses were due to the action of water flow, and scour problems occurred in 66 of them. Otherwise, 46% of the bridges studied were affected by this hazard (see Figure 4). Moreover, several authors [5], [9], [16]–[18] conclude that flooding is the main cause of bridge failure, which makes it the most relevant natural phenomenon. For these reasons, an integrated structural damage identification framework is proposed by applying robustness criteria to improve the quality assessment of railway bridges considering flood effects (e.g., local scour, water loads, and debris).
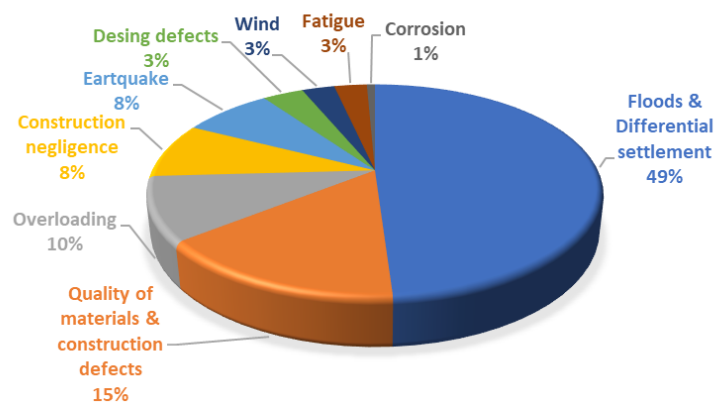
Figure 4. Statistic of bridges collapses between 1847 to 1975.

1.2 OBJECTIVES AND RESEARCH METHODOLOGY

A well-structured research methodology is fundamental to producing an excellent doctoral thesis. Doctoral research involves creating a review of the literature to state the current work that has been done under the area of research, putting forward an innovative idea to solve un-explored solutions that address society's problems. Therefore, this research attempted to explore aspects recommended for further investigation related to climate change considerations under flood analysis and reliability assessment on infrastructure.

To define the research focus, the relationship between the theoretical keywords "flood impacts" and "damage assessment" was pursued. From this perspective, floods are the main hazard for structures such as bridges due to the recorded collapse frequency. Thus, the impacts lead to a series of problems for bridges, causing structural damages and instabilities. Therefore, the impact of flooding is being studied to improve the estimation methods, since

current methods for quality control plans of railway networks do not consider complex hazard estimation procedures. In addition, current issues such as the effects of climate change affectation on weather patrons represent a challenge to researchers. Subsequently, damage detection research applies methods to identify and predict vulnerability to hazards based on inspection or monitoring. Then, maintenance or strengthening scenarios can then be implemented to manage the structure's service life. However, evaluating a structure requires applying several studies based on on-site measurements and complex calculations traduced in computation time, where simulations could take minutes, hours, or even days. Moreover, a simple parameter variation means inefficient changes in the modeling and calculation processes.

This thesis aims to develop an efficient framework based on accuracy and applicability to estimate and detect damages caused by floods influenced by climate change. It is also expected to contribute knowledge by testing and improving modeling techniques for structural damage and soil-structure interaction and integrating machine learning algorithms into the various disciplines of civil engineering such as hydrology, hydraulics, geotechnics, and structural reliability. Therefore, in order to successfully describe the framework, it is divided into four main workstreams, shown in Figure 5.
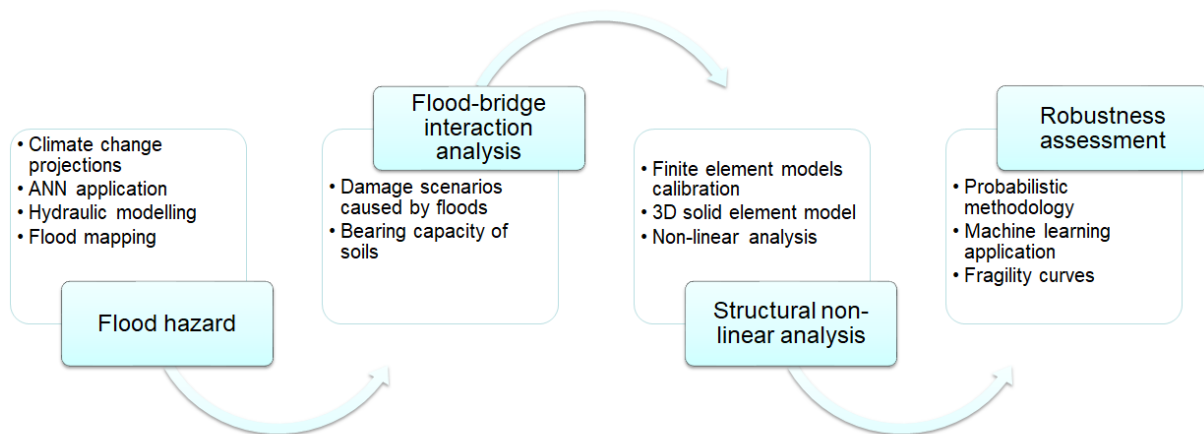
Figure 5. Proposed general framework.

1.2.1 WORKSTREAM 1 – FLOOD HAZARD

The main objective of a hydrologic report for flood estimation for bridge design and quality control is to estimate the critical flow based on the probability of occurrence or return period.

This workstream aims to propose a methodology for an artificial neural network capable of estimating peak flow discharge considering a rainfall projection database based on various parameters related to climate change uncertainties. The machine learning results can then be fed into a hydraulic model to identify relevant outcomes such as flood-prone areas using a geographic information system and estimate hydraulic parameters (e.g., flow velocity, water column height). Figure 6 summarizes the workstream procedure.
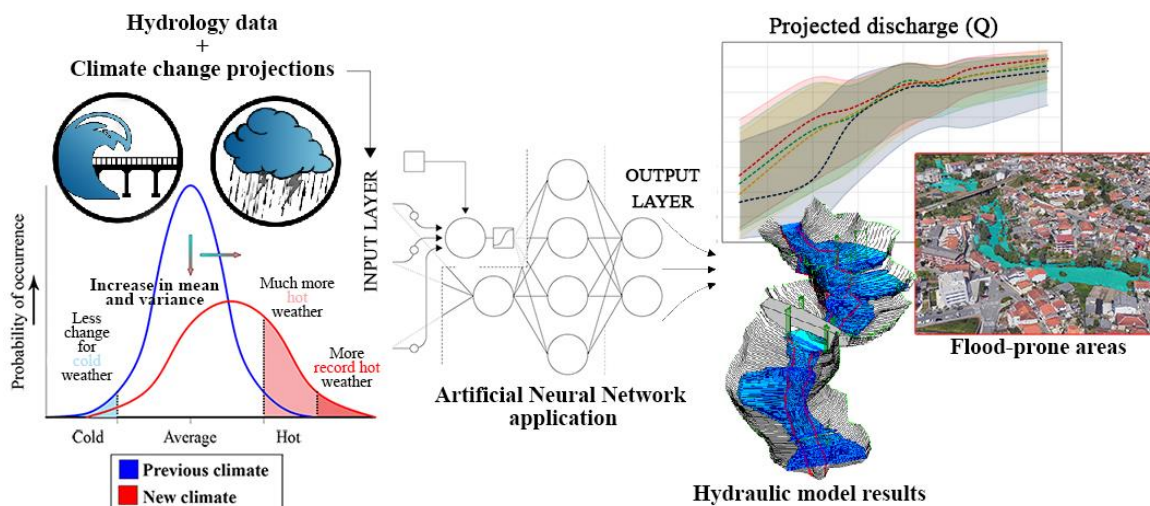
Figure 6. Graphical description of Workstream 1.

1.2.2 WORKSTREAM 2 – BRIDGE FAILURE ANALYSIS CAUSED BY FLOODS

This workstream aims to classify damage scenarios based on the assessed impacts of floods. Therefore, the methods to analyze and quantify these hydraulic impacts on bridges are presented. Then, the most significant and recurrent scenario (scour) is evaluated and treated as a geotechnical problem. In this sense, it is contemplated a method based on the bearing capacity of the soil considering the material remotion on the foundation, whether it is a shallow foundation (footings) or a deep foundation (pile foundation with a rigid pile cap).

1.2.1 WORKSTREAM 3 – STRUCTURAL NON-LINEAR ANALYSIS

The objective of this workstream is to perform a nonlinear structural analysis considering the soil-structure interaction through a finite element model. Consideration of the structural components of the bridge and the soil in the numerical model allows the simulation of damage

scenarios due to scour by direct removal of soil material. Therefore, it is expected that the failure mechanism due to induced instabilities and stiffness reduction can be analyzed.

1.2.2 WORKSTREAM 4 – ROBUSTNESS ASSESSMENT

The specific objective of this workstream is to calculate the robustness indicator through a metamodeling-based methodology. Therefore, it is necessary to compute the reliability index through a probabilistic analysis considering different uncertainties (random variables) related to the material properties of the structure. However, the key to tackling this step is to reduce the computational effort by applying a machine learning algorithm to simulate the ultimate load-carrying capacity resulting from workstream 3. Figure 7 shows the procedure in this workstream.
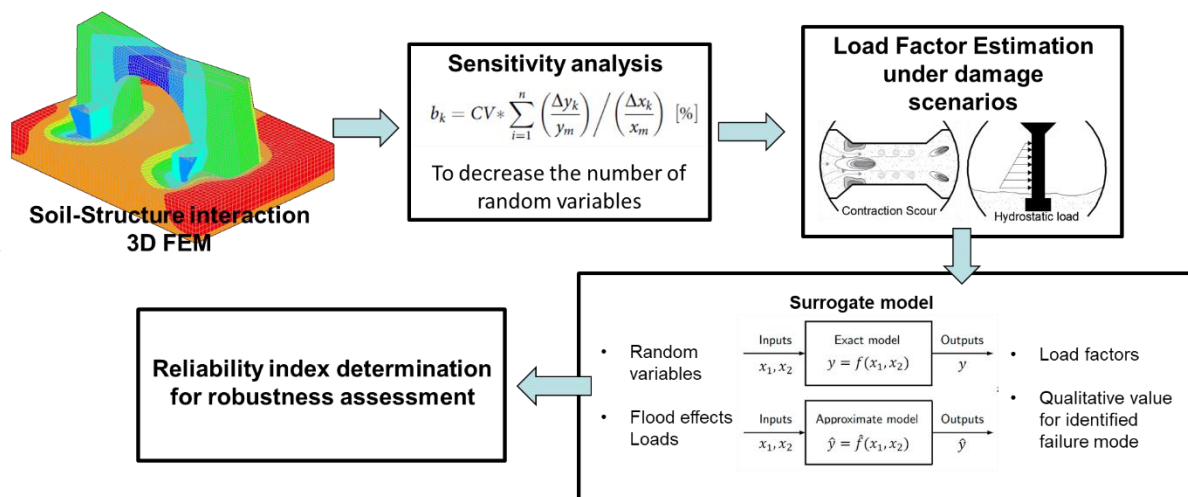
Figure 7. Graphical description of Workstream 4.

1.3 THESIS OUTLINE

Following this section, Chapter 2 is dedicated to the development of workstream 1 of the proposed framework. Therefore, an overview of flood assessment in terms of hydrological and hydraulic calculations is provided. In this way, a surrogate model-based climate change methodology is applied to a practical study area. Finally, an overview of flood mapping using GIS as a result of a hydraulic model is given, showing the vulnerability of the study area.

Chapter 3 focuses on workstream 2 of the proposed framework. In this sense, an overview of the interactions between hazard and structure is given, treating the issue as a hydraulic-

geotechnical problem. Therefore, current practices applied at the design industry level are applied in two practical cases.

Chapter 4 deals with the current evaluation of existing bridges, which implies the procedural methodology to develop work steps 3 and 4 of the framework. First, the adopted key performance indicators (reliability and robustness) were analyzed using state-of-the-art procedures. Following the literature review, two practical cases were evaluated, focusing on the estimation of the probability of failure.

Chapter 5 is dedicated to the implementation of the proposed framework in a specific case study. workstream 1 and 2 serve as preliminary information on the hazard whose results were estimated in the previous chapters. Then, workstream 3 and 4 focus on the evaluation of the bridge structure. The chapter aims to describe the proposed modeling technique to simulate the soil-structure interactions affected by scour scenarios in a calibrated model. Finally, the application of surrogate modeling to the reliability and robustness methods was implemented.

To conclude this document, Chapter 6 concludes the thesis with the final remarks on the research and the ideas for future work to improve and increase the contribution to the knowledge of the studied topics.
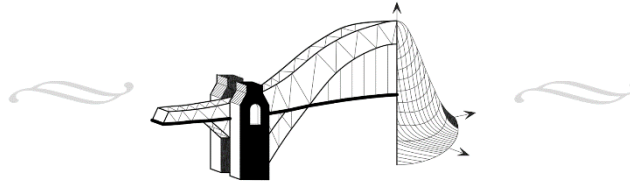
FLOOD ASSESSMENT

2.1 INTRODUCTION

Causes of flooding include numerous events (e.g., lack of vegetation, melting snow and ice, tsunamis, and typhoons). In addition, flooding can lead to phenomena that affect the strength and stability of infrastructure (e.g., scour, erosion, river convergence, insufficient embedment depth, overtopping or hydraulic jump, softened bedrock, sand mining, debris impact or abrasion on bridge foundations, etc.) [17].

Due to the economic or cultural importance of historical masonry arch bridges (the most typical bridge type in Europe) [19]. It is necessary to ensure their safety and functionality. According to the statistics presented by several authors [15], [20], [21], flood is the most frequent cause of bridge failure. Considering this extreme event, several authors [22]–[24] confirm that the frequency of floods has increased worldwide. This leads to economic losses and human casualties. Considering pluvial floods, the above statement can be related to the effects of global warming. Therefore, global climate change implies uncertainty due to the influence of local weather patterns, which is one of the consequences of changing river flow regimes that affect the behavior of extreme weather events, including extreme precipitation and river flows [25], [26]. Evidence presented by Katz [27] and Boulent [28] suggests that the statistical properties and distribution of critical climatic parameters (e.g., temperature, precipitation) may change as a temporary affectation (see Figure 8).
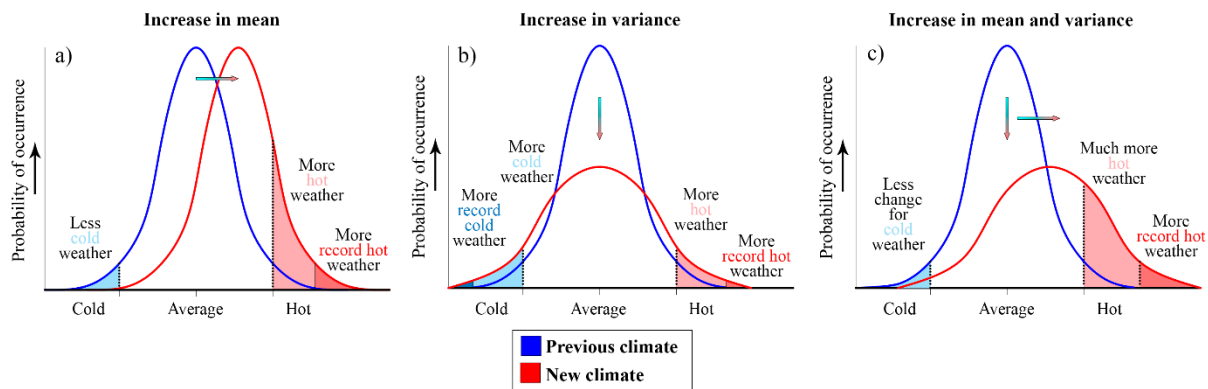
Figure 8. Statistical variability of climate change **[28]***.*

As the mean cause of climate change is greenhouse gases, potential emission scenarios are proposed by the Intergovernmental Panel on Climate Change (IPCC) [29] developed for future adaptation strategies until the end of the 21st century, which cover the quantification of the potential effects of climate change (e.g., Increase of frequency and magnitude of flooding). In addition, it can be used as a basis to define the statistical variability of global or regional weather [28].

This chapter aims to use projected climate models to integrate and complement the hydraulic models of the watershed case study, proposing an artificial neural network (ANN) model to simplify the calculations and reduce the time-consuming process. The introduction of artificial intelligence algorithms as a surrogate model in many engineering fields provides the opportunity to replace conventional models by achieving the desired results and reducing the investment in terms of computations time and effort. Moreover, due to its accuracy and effectiveness, ANN technology has proven to be an effective tool in various hydrological problems. To confirm this, Tanty and Desmukh [30] investigated the state of the art in the acquisition of applications such as rainfall and runoff modeling and streamflow modeling.

2.2 PROPOSED METHODOLOGY

The proposed method of an artificial neural network application capable of estimating peak flow discharge considering a rainfall projection database based on various parameters related to climate change uncertainties. After applying the ANN, the resulting information can be used to estimate the flow peak discharge of the case study zone. Then, in the next steps, a hydraulic model can be defined. First, the geographical data of the study area must be collected and

processed using Geographic Information System (ArcGIS) software developed and distributed by ESRI (Environmental Systems Research Institute). Second, all the information is exported from GIS to HEC-RAS to build the hydraulic model with the calculated discharges considering different return periods. Third, the flooding simulations are performed. Figure 9 summarizes the described workflow for the hydraulic model, the required input data, and the expected results.
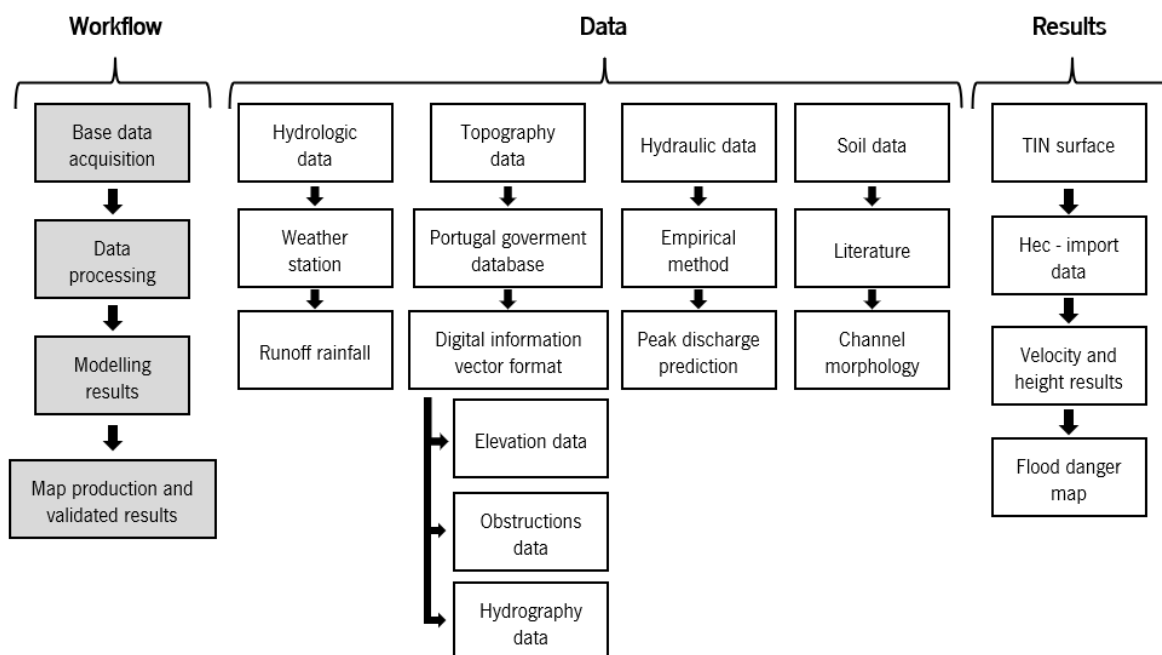
Figure 9. Research methodology applied for flood assessment.

2.2.1 FLOOD FREQUENCY ANALYSIS AND PEAK DISCHARGE ESTIMATION

Traditional flood computation methods assume that climate and/or land use are unchanged (steady-state flood time series). Therefore, uncertainties related to climate change, intensification of human activities, land cover changes, and water management activities in the watershed are not considered, affecting the mechanism of flood generation, resulting in a non-stationary flood time series [31].

Debele et al. [32] compared three different approaches for analyzing nonstationary flood frequency: i) maximum likelihood (ML), ii) two-stage (WLS/TS), and iii) GAMLSS (generalized additive model for location, scale, and shape parameters). According to Strupczewski [33] the ML method is the most theoretically correct method for fitting probability distributions to

data. It leads to asymptotically efficient and unbiased parameter estimates, i.e., estimates of the population parameters with the lowest average error. The estimates of distribution parameters are obtained by maximizing the log-likelihood function according to equation (1), where f is the density function, θ is the vector of trend model parameters and k is the shape parameter.

$$ln\, L(\theta, k) = \sum_{i=1}^{T} ln(f(y_i; \theta, k)) \tag{1}$$

The WLS/TS method defined by Kochanek et al. [34] is a hybrid method and consists of a separate estimation of time-dependent mean and standard deviation performed by the Weighted Least Squares (WLS) method, thus, it estimates the shape parameter and time-dependent quantiles. This method incorporates non-negative weights corresponding to each data point, restricted by the fitting criterion. A nonstationary mean value cannot be assessed separately of the trend in the standard deviation. Moreover, an unknown nonstationary variance indicates that the system of equation (2) ought to be solved for the linear form of trends in the mean and the standard deviation. where y_t are the elements of time series, m_t represents the mean value in time t, s_t is the standard deviation in time t. The equations are solved in respect of unknown trend model parameters ($m_t = a_t + b$; $s_t = c_t + b$).

$$\begin{cases} \sum_{t=1}^{T} \dfrac{t}{s_t^2}(y_t - m_t) = 0 \\ \sum_{t=1}^{T} \dfrac{1}{s_t^2}(y_t - m_t) = 0 \\ \sum_{t=1}^{T} \dfrac{t}{s_t^3}\{(y_t - m_t)^2 - s_t^2\} = 0 \\ \sum_{t=1}^{T} \dfrac{1}{s_t^3}\{(y_t - m_t)^2 - s_t^2\} = 0 \end{cases} \tag{2}$$

GAMLSS models proposed by Rigby et al. [35] are statistical models for a univariate response variable, assuming independent observations of the response variable y given the parameters, the explanatory variables, and the values of the random effects. Moreover, the GAMLSS models provide a framework for regression-type models, combining models often considered as different in the statistical literature. Besides, the GAMLSS framework is

assumed that independent observations y_i, for $i = 1, \ldots n$, have a probability distribution function of $f_y(y_i | \theta_i)$ with $\theta^i = (\theta_1^i, \ldots, \theta_p^i)$ as a vector of p $(p \leq 4)$ parameters accounting for location, scale and shape of the distribution of random variable y. Due to the GAMLSS methodology involves several models, Debele et al. [32] recommends the use of the fully parametric formulation exposed in equation (3), where θ_k are vectors of length n, X_k is a matrix of explanatory variables of order $n \, x \, m$, β_k is a parameter vector of length m.

$$g_k(\theta_k) = X_k \beta_k \tag{3}$$

Due to the challenges of the uncertainties related to the hydro-meteorological conditions, new approaches to reconstruct flood time series for non-stationary frequency estimation were developed [36]. Besides the hydrological modelling, there are methodologies based on rainfall-runoff correlation analysis, where it is established the rainfall-runoff function applying the land-use change, while the flood time series of the unchanged land-use (historical observed rainfall) are recalculated based on the function [31], [37].

Recently, many probabilistic approaches have been developed for extreme flood estimation, mostly for structural design. Paquet [38] introduced the SCHADEX probabilistic method (semi-continuous stochastic simulation) based on rainfall-runoff simulation. Thus, the methodology achieves complete distributions of areal rainfall, flood volumes and flood peaks, up to extreme quantiles, hourly hydrographs for hydraulic modelling. The SCHADEX method was applied in several case studies. Paquet [38] presented an example of the River Tarn at Millau (2170 km², South of France), being available to estimate the distribution of flood daily discharges and flood peaks. Other authors as Valent et al. [39] tested in the Slovak conditions on a mountainous catchment of the River Hron at Banská Bystrica (1768 km²) in Slovakia, where two datasets with daily (from 1981 to 2010) and hourly (from 1988 to 2002) time steps were used in combination to estimate mean daily and hourly floods with several return periods; and Brigode [40] applied the complete modelling chain, from weather pattern definition to stochastic simulation of river discharge to an Austrian catchment, the Kamp river at Zwettl (600 km², North of Austria).

On the other hand, some methodologies are easier to apply. As an example, Holemba [41] presented a study regarding the frequency of bridge failures and collapses caused by flooding

rivers in Papúa Nueva Guinea, where it was assessed twenty-one flood affected bridges based on field investigations. In that case, the quantile magnitude of the hazard was used to estimate the Regional Flood Frequency Method (RFFM) [42], thus the following equations were used:

$$Q_2 = 0.028 * AREA^{0.70} * P_2^{1.12} * KS \qquad (4)$$

$$Q_{20} = Q_2 + 0.62(Q_{100} - Q_2) \qquad (5)$$

$$Q_{100} = 0.059 * AREA^{0.65} * P_2^{1.12} * SLOPE^{0.11} * KS \qquad (6)$$

Where Q_2 is the two-year return period or the base flood, Q_{20} is the twenty-year return period and Q_{100} is the one-hundred-year return period which is known as Average Recurrence Intervals (ARI) or return periods. The $AREA$ represents the area of the catchment size in km², P_2 is the two-year daily rainfall data taken from flood estimation manual, the $SLOPE$ is the mean slope of the river channel and KS is the swamp adjustment factor of the main catchment and 0.62 is the regression factor for Q_{20} return period [43].

In mainland Portugal, exist several empirical methodologies used in the standard guidelines for peak discharge estimation, which consider the information of the watershed and rainfall data. According to Velhas [44], the Giandotti method [45] is part of the standard guidelines for dam design. This method considers flooding originating from precipitation P with a total duration t associated with a return period T_r. Therefore, Equation (7) defines the peak discharge during flooding.

$$Q = \frac{277 \, a \, b \, P \, A}{c \, T_c} \qquad (7)$$

The variable Q is the peak discharge in m³/s, P is the precipitation in m, A is the area of the watershed in km², T_c is the concentration-time in hours, a and b are runoff coefficient parameters associated with the area, and c is the flood duration coefficient. The runoff coefficient parameters can be found in the literature. Quintela [46] recommends for watersheds with an area lower than 500 km² the following values: $a = 6.5$, $b = 0.5$, and $c = 4$. To determinate the concentration time of the watershed, DeLencastre [45] proposed

Equation (8), where L is the main river's total length, and H is the average altitude of the watershed in meters.

$$T_c = \frac{4\sqrt{A} + 1.5L}{0.8\sqrt{H}} \qquad (8)$$

Another empirical methodology herein used is the rational method [47], one of the most applied formulas to determine peak discharge in Portugal for small and medium watersheds of areas between 10 and 600 km². The empirical formula depends on the rainfall intensity calculated considering the IDF curves and the runoff coefficient for a specific return period.

2.2.2 SURROGATE MODEL ALGORITHMS

It is well established that in many areas of engineering, surrogate models (also known as response surfaces or metamodels) are used to replace the traditional way of collecting data and verifying the performance of engineering results. However, the investment in computational time when using analytical models might be less practical in some cases (a simulation can take minutes, hours, or even days). To address this issue, surrogate models can replace analytical models by establishing a relationship between the analyzed variables (inputs - outputs) [48], using a relatively small number of evaluations of the (presumably expensive) response function of interest to construct an approximation to that function that is cheaper to evaluate.

The first proposal of a metamodel was presented by Box and Wilson [49], who used a second-order polynomial approximation. Since then, polynomial models have remained popular due to their ease of construction and evaluation. Therefore, these models are rigid and may yield inaccurate models when the function of interest is not a polynomial [50].

The most recognized surrogate models are polynomial, response surfaces methodology (RSM), kriging or Gaussian process regression, gradient-enhanced kriging (GEK), radial basis function (RBF), support vector machines, space mapping, artificial neural networks (ANN), and Bayesian networks.

In civil engineering, the evaluation of complex structures such as bridges requires the incorporation of metamodels to reduce computational time. Ghosh [51] presented a study using a large number of nonlinear dynamic analyses of finite element models (FE) to obtain a seismic response; therefore, the approximation is generated and compared from different types of surrogate models, such as polynomial surface models with stepwise regression (PRSM), multivariate adaptive regression splines (MARS), Radial Basis Function Networks (RBFN), and Support Vector Machines for Regression (SVMR).

ANN is a specific surrogate model used by many researchers in structural problems such as identifying the damage location and severity. Bakhary [52] presented an overview of applications of ANN such as: i) damage detection in a three-story frame, ii) a detailed treatment of network architecture for damage detection in a beam bridge truss, iii) the use of a neural counter propagation network in damage analysis in a continuous beam, iv) a method for damage assessment of steel structures. Most of the studies developed with an artificial neural network provide correct damage identification, moreover, the probability of error at different stages of the health monitoring is given by modelling errors in the FE model due to the uncertainties of the parameters and the possible errors in the measured data.

Lee et al. [53] presented a study in which the back-propagation neural network (BPN) was used to estimate the scour depth of bridges, and the performance of the network was validated using measured data of the bridge. Choi et al. [54] used the same training and optimization method to build the surrogate model and estimated the local scour around the bridge piers of a case study, validating the network through laboratory tests.

The chosen algorithm to develop the objectives of this research is Artificial Neural Networks (ANNs) due to its capacity for solving highly complex non-linear problems. Based on the biological functionality of the human brain, the nervous system is recreated in a mathematical model interconnecting processing unit called a node or neuron. Thus, neurons are classified depending on the layer (i.e., input layer, hidden layer, output layer), and the connections are through a "synaptic weight". Figure 10 attempts to exemplify the primary element component (neuron) and the most basic architecture of the network, followed by the mathematical description of each part [55]. Then, the following procedure is the network training process.

In this sense, the weights of each neuron must be updated following an optimization algorithm until the model reaches its maximum error allowed (e.g., backpropagation algorithm).
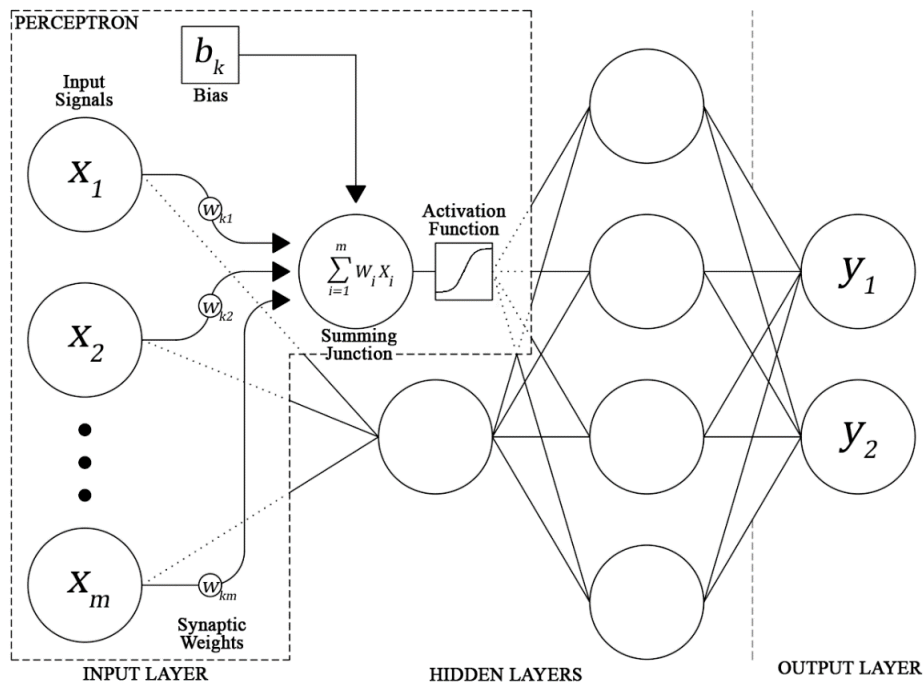
Figure 10. A generic ANN architecture composed of input neurons, hidden neurons, and output neurons connected by synaptic weights.

2.3 LEÇA RIVER WATERSHED

2.3.1 HYDROGRAPHIC REGION CHARACTERIZATION

The proposed study zone is located in a watershed with the Leça river as its main tributary. Moreover, it contains a specific railway bridge located in the urban area of Ermesinde which fulfil the conditions for the full application of the proposed framework (see Figure 11). Consequently, this bridge was assessed in subsequent sections.

The considered watershed has an area of 189.0 km² and a total length of 30.4 km passing through several urban areas (e.g., Ermesinde, Matosinhos, among others) and flowing into the Atlantic Ocean. Along the waterway there are structures that can be considered as obstacles, such as buildings/houses near the riverbed, bridges (some dating back to the middle age), weirs, and retaining walls. These obstructions disrupt flow conditions and create ineffective areas that affect the height and velocity of the water and the extent of flooding.
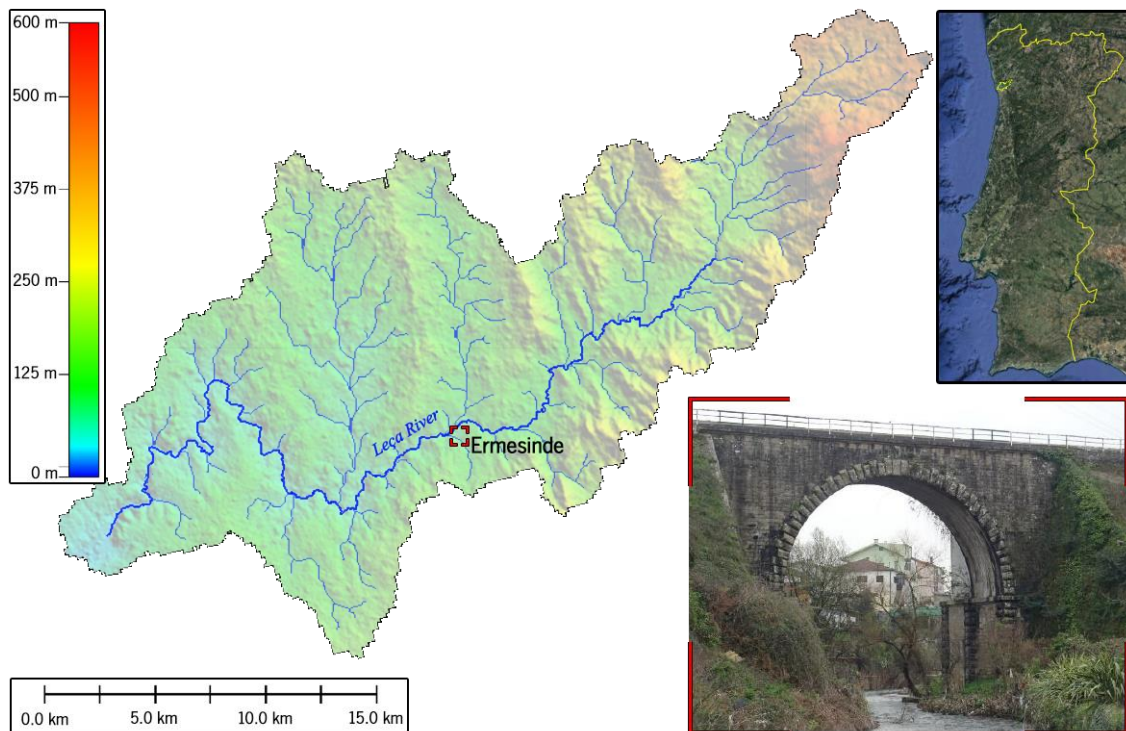
Figure 11. Case study location in the Leça river watershed.

According to Gonçalves et al. [56], who collected information from national and local newspapers, several areas of the watershed are frequently flooded, with important flood events causing significant damage in 1926, 1929, 1935, 1961, 1979, 2001, and 2013 (see Figure 12). However, the research presented by Velhas [44] concluded that there are three zones of high flood risk in the watershed, which do not include the case study zone (Ermesinde). This is because the natural gradient in the river channel is considerably high, and the entire urban area of the zone is above it. However, even if the risk of flooding in urban areas is low, it does not mean that the structures along the watercourse cannot be affected.

Figure 12. General view of several sectors in the Leça watershed and measurements of the 2001 flood. Adapted from **[56].**

To characterize the geological and geomorphological nature of the watershed, the geological cartography from IGeoE, published by Soares et al. [57] was consulted, which includes a

graphical representation of the morphology, hydrography, lithography, and tectonics (see Figure 13). A series of materials can be identified in the watershed, divided into four groups: i) superficial formations; ii) metasedimentary formations; iii) granitoid rocks; and iv) metasediments. These materials are important because of their influence on topographic features, control of surface runoff rates, and water movement due to their permeability and porosity [44].
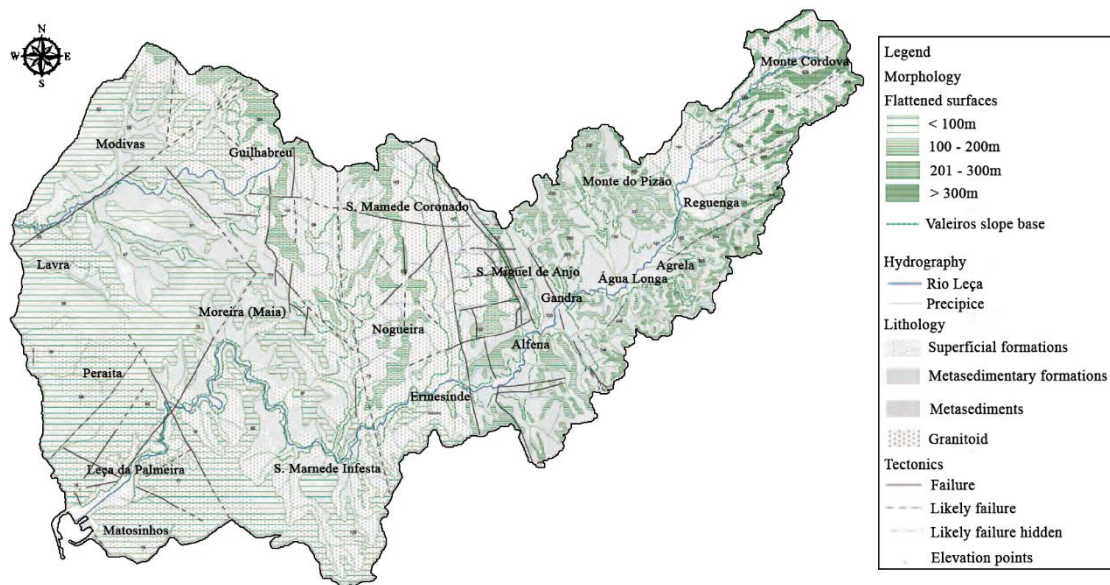
Figure 13. Morphology, hydrography, lithography, and tectonics of the watershed. Adapted from **[57]***.*

The last information to consider is the land cover of the study area due to its influence on the velocity of water runoff throughout the watershed. The data were provided by the Portuguese institute "Direção-Geral do Território". According to the data, land use in the Ermesinde sector is closely related to the slope of the land. Thus, in areas with slopes between 16º and 25º, the biogeographical factors in the watershed favor good to moderate water retention, since in these areas an extensive forest cover was found, especially pines, although in some sectors it has been fragmented by fires. Areas with slopes greater than 25º have a much lower forest cover, often with a low density, and in some sectors the presence of undergrowth with low density and even bare ground, which increases the values of surface runoff. In the areas adjacent to watercourses, where the soil thickness is greater and slopes are much weaker, and in most areas with slopes of less than 8º, the land use is essentially agricultural. Figure 14 shows the details of land use and land cover throughout the watershed and the percentage of each category.
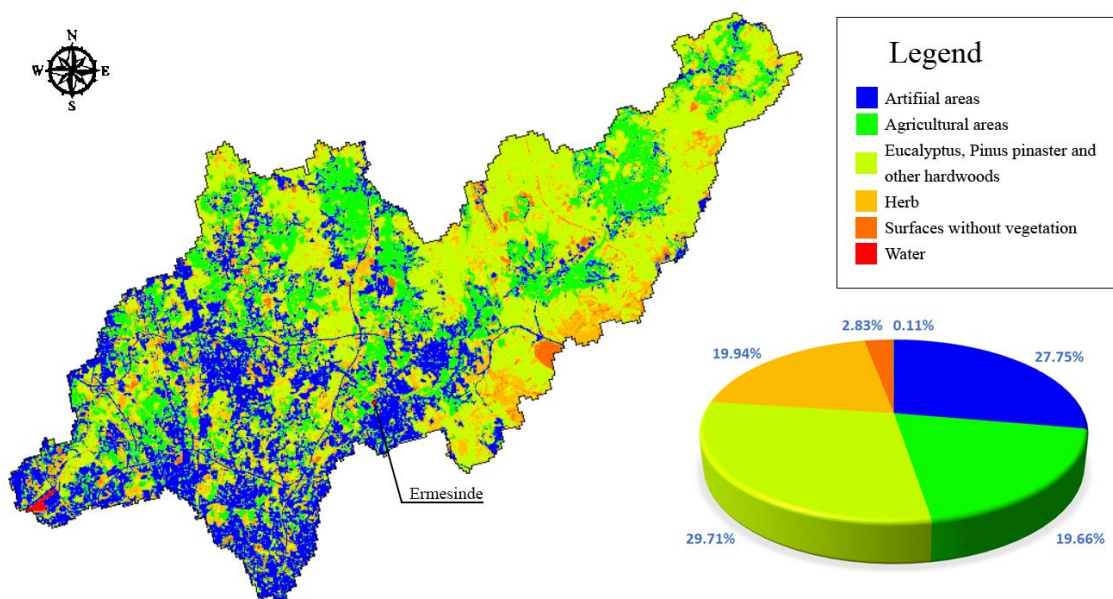
Figure 14. Details of land use and land cover details in the Leça river watershed.

The Leça watershed contains several hydrometrical and meteorological stations administrated by the "Sistema Nacional de Informação de Recursos Hídricos" (SNIRH). Table 1 shows the details and quantity of the accessible database, followed by their location in Figure 15. However, considering the available data, only the information on the Ermesinde station can be used due to its location (closeness to the designed study area of the watershed) and consistency. Therefore, the records were organized in 41 hydrological years as monthly data of maximum rainfall in 24 hours (see Figure 16).

Table 1. Weather stations of the Leça River watershed [58]*.*

Name	Altitude (m)	Latitude (°N)	Longitude (°W)	Start date	End date	Station type
Ermesinde	73	41.221	-8.559	01/10/1979		Udometric
Leça da Palmeira	17	41.198	-8.69	01/10/1979		Udometric
Fervença	305	41.307	-8.444	01/10/1980	30/09/1990	Limnimetric
Pereiras	331	41.31	-8.442	03/01/1980	30/09/1990	Limnigraphic
Ponte moreira	31	41.236	-8.646	23/06/2003		Level sensor
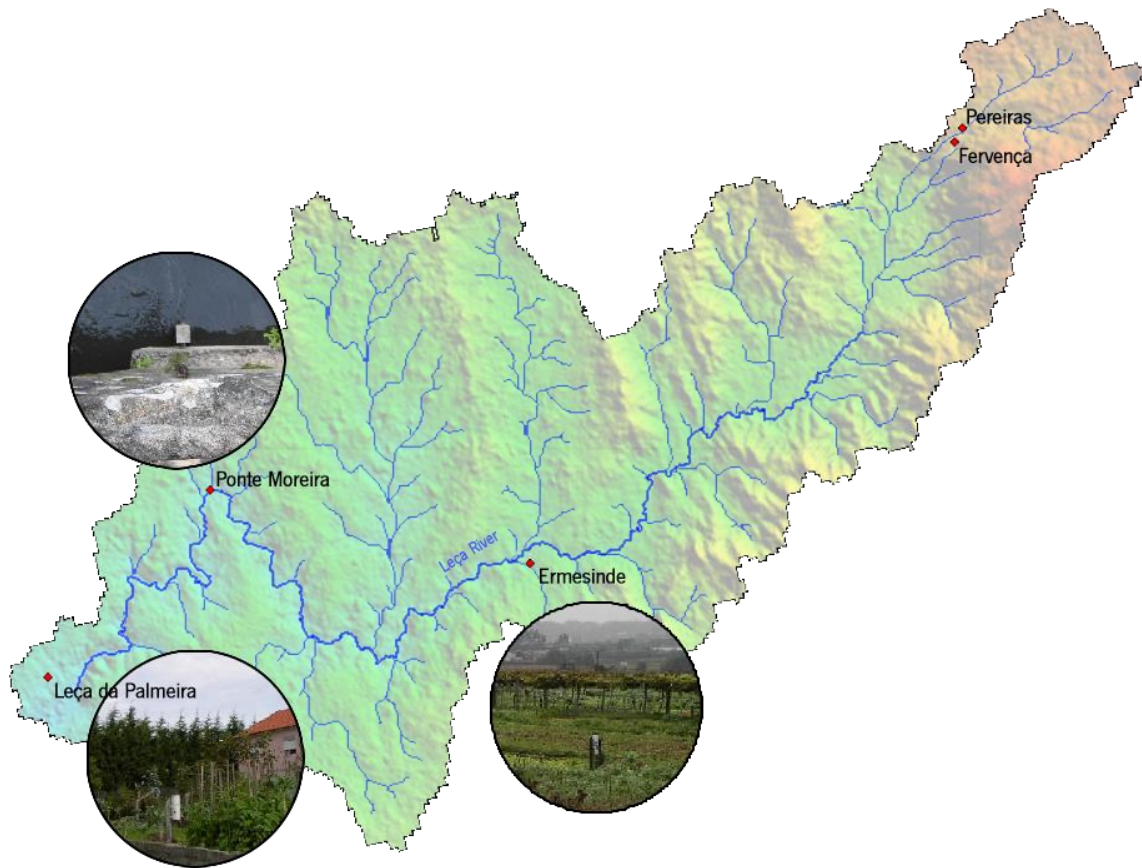
Figure 15. Location of the meteorological and hydrological stations.
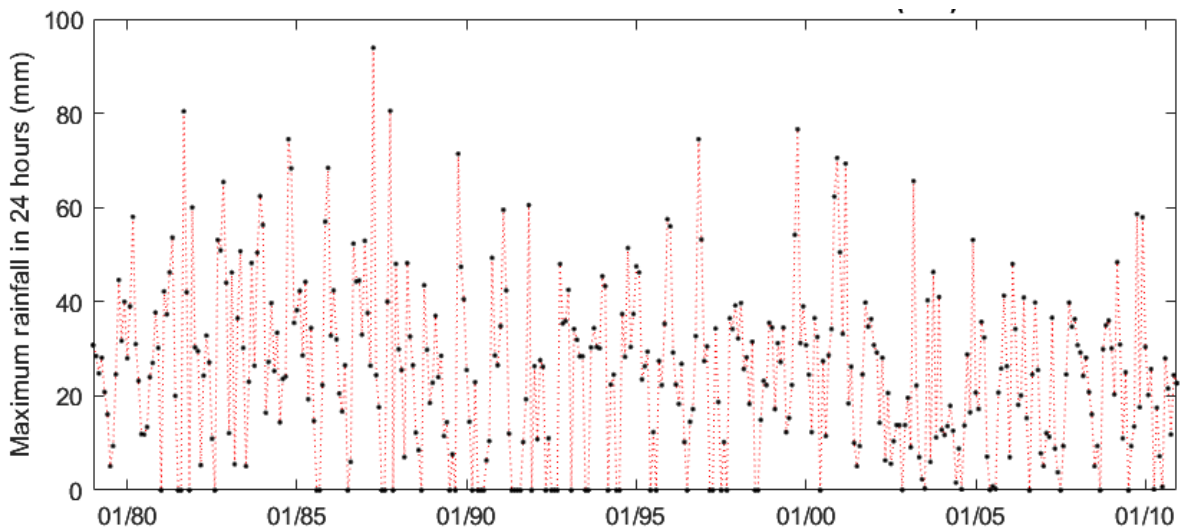
Figure 16. Monthly data of maximum rainfall in 24 hours from Ermesinde station.

According to the Climate Change Knowledge Portal (CCKP) of the World Bank Group [59], the main factors affecting the climate of mainland Portugal are latitude, orography, and proximity to the Atlantic Ocean. Regarding the precipitation in the Porto region (including the Leça watershed), the historical data presented in Figure 17a show a constant tendency during the

20th century. On this watershed, the upper reaches contain part of the mountainous regions of Minho, which have the highest precipitation values compared to the other areas of Portugal. Nevertheless, the amount of precipitation varies during the seasons (see Figure 17b). On average, about 40% falls in winter (December-February), while only 7% in summer (June-August). On the other hand, the transitional seasons (spring and autumn) show a variable inter-annual distribution with roughly 24% and 28%, respectively.
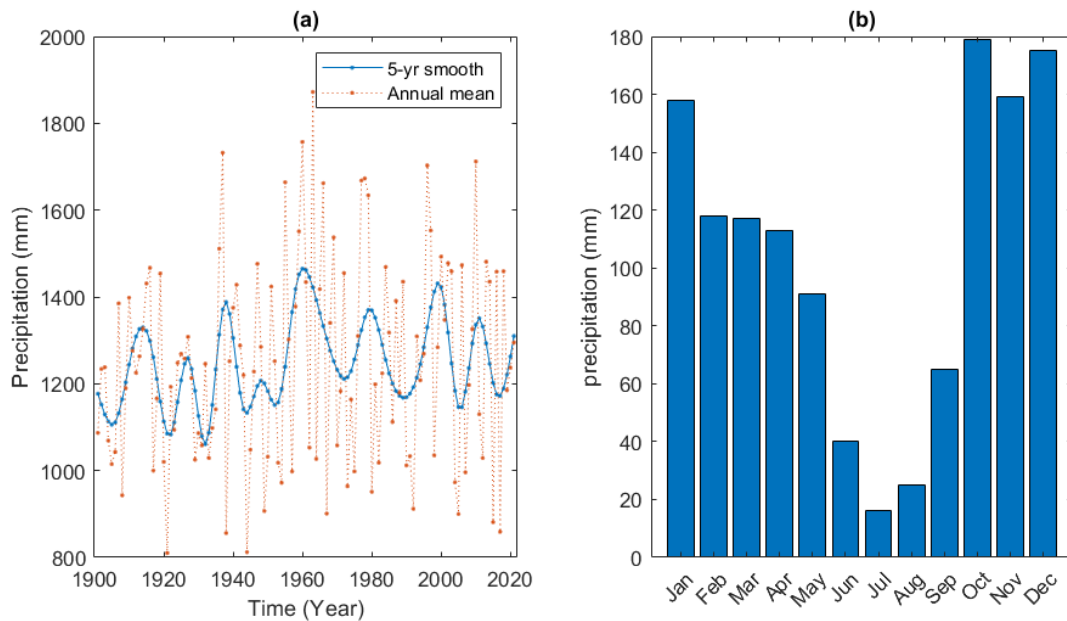
Figure 17. Precipitation in the Porto region for 1901 – 2021: (a) observed average annual precipitation; and (b) monthly average precipitation. Adapted from [59]*.*

The basis for the climate projections in this research is a set of global climate models studied by the Coupled Model Intercomparison Project, Phase 6 (CMIP6) and the analysis of climate impacts by applying multi-model ensembles developed by CCKP. Thus, the scenarios used follow different trends in greenhouse gas (GHG) emissions, air pollutant emissions, and land use described in the IPCC Sixth Assessment Report [60]. Five different pathways or Shared Socioeconomic Pathways (SSPs) were defined for the 21st century: i) SSP1.9/SSP2.6 - low GHG emissions; iii) SSP4.5 - intermediate GHG emissions scenarios; iv) SSP7.0/SSP8.5 - very high GHG emissions. Based on the SSPs, the expected rainfall for the Porto region was projected until 2100, as shown in Figure 18. It can be seen that higher GHG emissions reduce the expected accumulated precipitation, following the trend of each SSP. In addition, the data are presented in percentile ranges across years. Therefore, the expected maximum values

predominant for the low GHG emission scenarios and the minimum values predominate for the very high GHG emission scenarios.
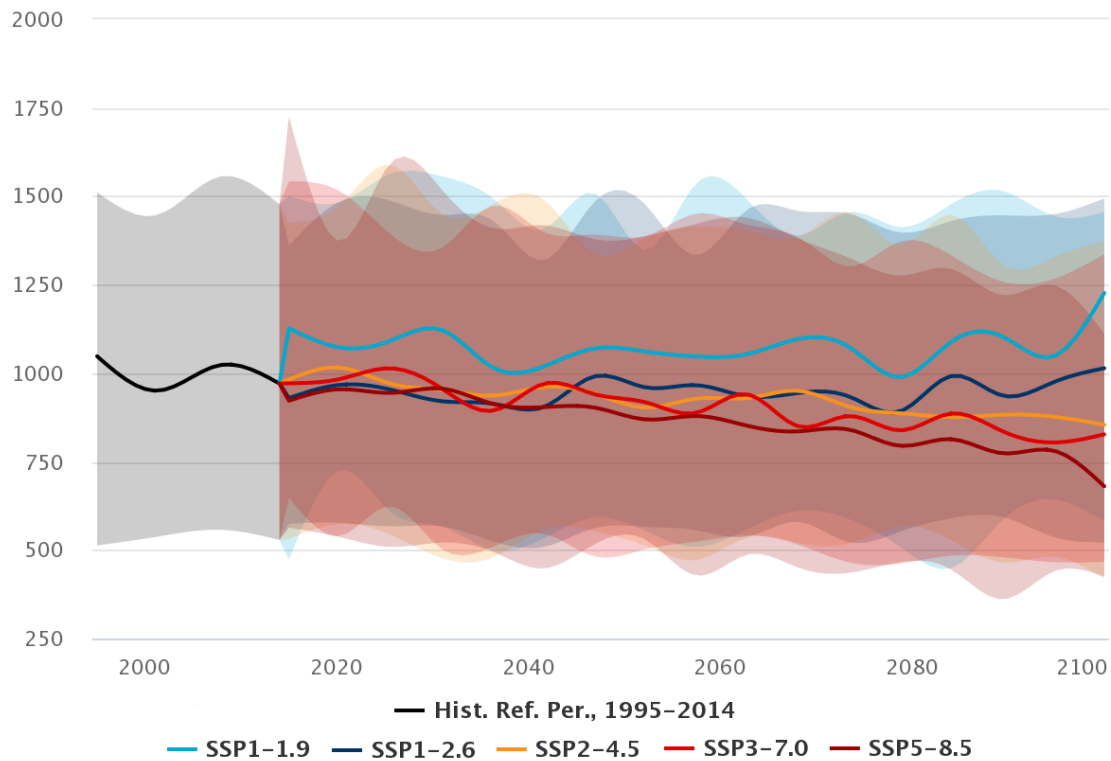
Figure 18. Projected precipitation for the Porto region (reference period 1995-2014). Adapted from **[59]**.

2.3.2 RESULTS AND DISCUSSION

2.3.2.1 Hydrological modeling application

The precipitation data considered was the highest amount of precipitation within a 1-day period in each month of the data period. Since the collected projection data were presented considering different variables (SSP scenarios, percentiles for each future year of the 21st century, and return period), the metamodel-based methodology was applied to fit the data to a probability surface considering all variables involved. In this sense, the data of each SSP scenario were ordered from the highest to the lowest value and the percentile data of each data year were fitted to a statistical distribution function (Gumbel). Figure 19 shows in a 3D representation the organization of the dataset for the SSP 1.9.
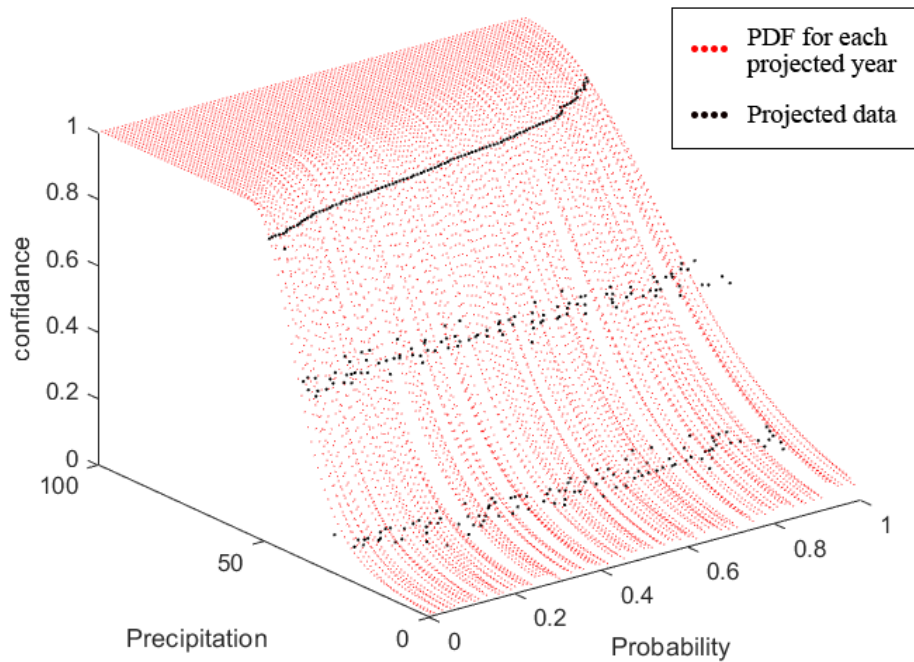
Figure 19. Summary of the example of adjustment of PDFs for each projected year.

In this research, the following steps were defined to achieve an accurate multi-layer perception ANN: i) the definition of the parameters to be estimated by ANN; in this case, the output is the precipitation data (P). ii) The definition of the input parameters is divided into two groups: probabilistic factors (percentile range, return period) and the SSP scenarios. iii) The size of the data set to obtain the correct behavior of the data variation, in this case the input was a 145413x3 matrix and the output was a 145413x1 vector. iv) The choice of the architecture of the ANN (see Figure 20). For the perceptron, the activation function (sigmoid function) is used due to its form and range, and it fits the final desired output. For the hidden layers, only one layer was chosen because the network with two or more layers requires more computational effort and the results do not improve. Moreover, it was tested with different number of hidden neurons. It was found that ten is an optimal number for this problem, which gives a balance between training time and data fitting. Backpropagation was used for the training algorithm and Mean Squared Error (MSE) was used as the loss function. Finally, v) train the network with 60% of the data and use the rest of the dataset to validate and test the network (data that the algorithm never used for its training improving the ability to predict). This step especially helps to avoid overfitting the surrogate model.
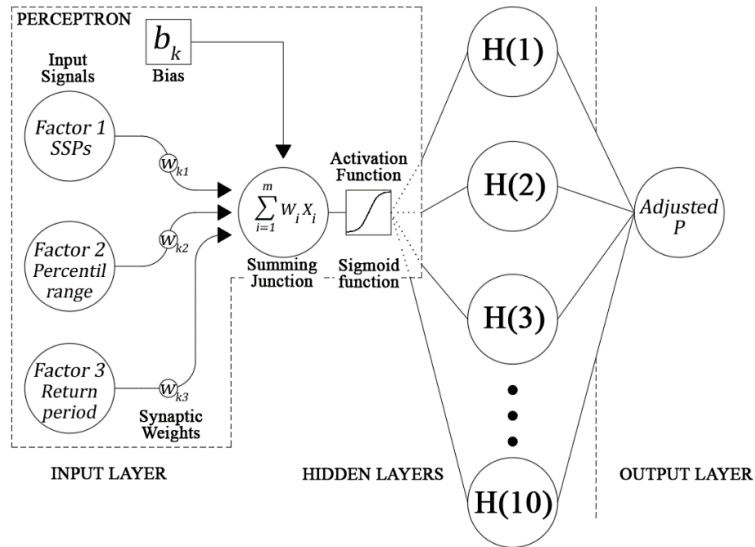
Figure 20. Network architecture used for the multi-layer perceptron ANN.

Once the training process of ANN was established, the probability surface plot can be drawn (see Figure 21). This graph shows the adjusted precipitation considering the probability of occurrence and the percentile range. Nevertheless, some problems were found in the results when the probability approaches one, since the result tends to infinity for a probability distribution function. With this in mind, it is recommended to work only up to a probability of 0.9 (T_r =100 years). After that, the result may not be accurate.
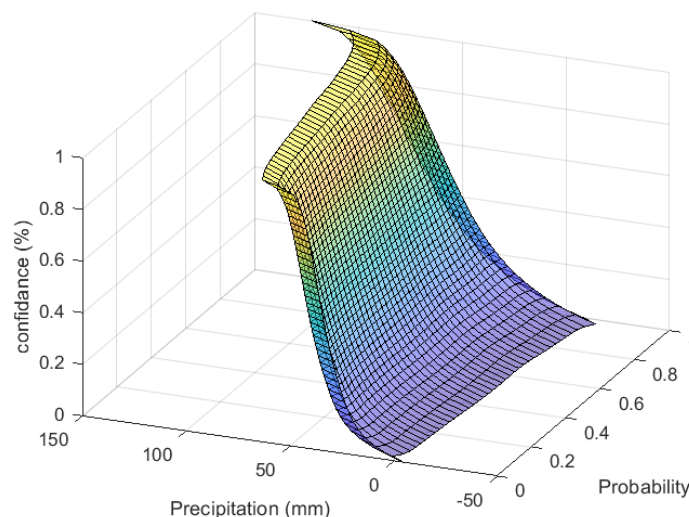
Figure 21. Fitted maximum daily precipitation using the ANN model.

The Giandotti method, specified in subsection 2.2.1, was used on the fitted values from the surrogate model to determine the peak discharge values associated with a probability of

occurrence. Figure 22 shows the results for the predicted discharge considering different confidence levels for a range of 1 to 100 return periods.
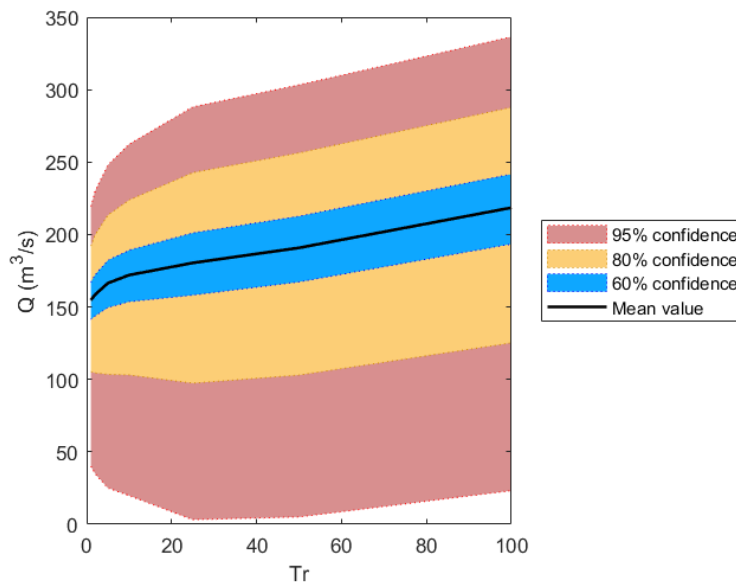
Figure 22. Confidence intervals of projected discharge versus return period.

Other traditional methodologies were performed to validate the quality and accuracy of the results: i) the rational method, ii) $Q = aA^b$ fitting, and iii) rainfall frequency analysis applying historical data. Therefore, for the rational method, the rainfall intensity was obtained considering the IDF curves published in the "Ministério das Obras Públicas" [28] and on the runoff coefficient obtained through the "Sistema Nacional de Informação de Ambiente" (SNIAmb) for a return period of 100 years.

For the $Q = aA^b$ fitting method, the calculations were based on the research executed by Velhas [21], which evaluated the data of maximum peak discharges from hydrological stations in the watershed.

The rainfall frequency analysis was performed using the historical information of the Ermesinde station. Therefore, the data were fitted to a probability distribution function (PDF). Consequently, it was necessary to compute some probabilistic variables which depend on the mean ($\bar{x}$) and the standard deviation (s_x) such as the parameters of location (μ), scale (σ), and shape (κ) (See Table 2 and Table 3) [61]–[63]. Finally, The MATLAB© software was used to develop a successful data adjustment to the proposed probability and cumulative distributions (see Figure 23).

Table 2. Summary of (two/three-parameter) distributions for frequency analysis.

Name	Probability density function
Weibull	$f_Y(y\|\sigma,k) = \dfrac{k}{\sigma}\left(\dfrac{y}{\sigma}\right)^{k-1} exp\left[-\left(\dfrac{y}{\sigma}\right)^k\right]$ $\sigma > 0; k > 0$
Gumbel	$f_Y(y\|\mu,\sigma) = \dfrac{1}{\sigma} exp\left(\dfrac{y-\mu}{\sigma}\right) exp\left(-exp\left(\dfrac{y-\mu}{\sigma}\right)\right)$ $-\infty < y < \infty; \ -\infty < \mu < \infty; \ \sigma > 0$
Gamma	$f_Y(y\|\mu,\sigma) = \dfrac{1}{\sigma^k \Gamma(k)} x^{k-1} e^{\frac{-x}{\sigma}}$
Log-normal	$f_Y(y\|\mu,\sigma) = \dfrac{1}{\sqrt{2\pi\sigma^2}} \dfrac{1}{y} exp\left\{-\dfrac{[\log(y)-\mu]^2}{2\sigma^2}\right\}$ $y > 0; \ \mu > 0; \ \sigma > 0$
Pearson type iii	$f_Y(y\|\mu,\sigma,k) = \dfrac{1}{\Gamma(k)\sigma}\left(\dfrac{y-\mu}{\sigma}\right)^{k-1} exp\left[-\left(\dfrac{y-\mu}{\sigma}\right)\right]$ $\mu > y > \infty$
GEV	$f_Y(y\|\mu,\sigma,k) = \dfrac{1}{\sigma}\left[1 + k\left(\dfrac{y-\mu}{\sigma}\right)\right]^{\left(-\frac{1}{k}-1\right)} exp\left\{-\left[1 + k\left(\dfrac{y-\mu}{\sigma}\right)\right]^{-\frac{1}{k}}\right\}$ $\mu + \dfrac{\sigma}{k} < y < \infty$
Log-normal type iii	$f_Y(y\|\mu,\sigma,k) = \dfrac{1}{(y-\mu)k\sqrt{2\pi}} exp\left\{-\dfrac{[\log(y-\mu)-\sigma]^2}{2k^2}\right\}$ $\mu < y < \infty$
location μ, scale σ and shape k	

Table 3. Computation of probabilistic values.

PDF	$\bar{x}$	s_x	μ	σ	k
Weibull				62.13	3.66
Gumbel			64.61	17.59	
Gamma				12.32	4.55
Log-normal	56.08	16.45	3.99	0.29	
Pearson type iii			15.52	7.08	5.73
GEV			-0.05	13.47	48.79
Log-normal type iii			53.77	16.04	-0.28
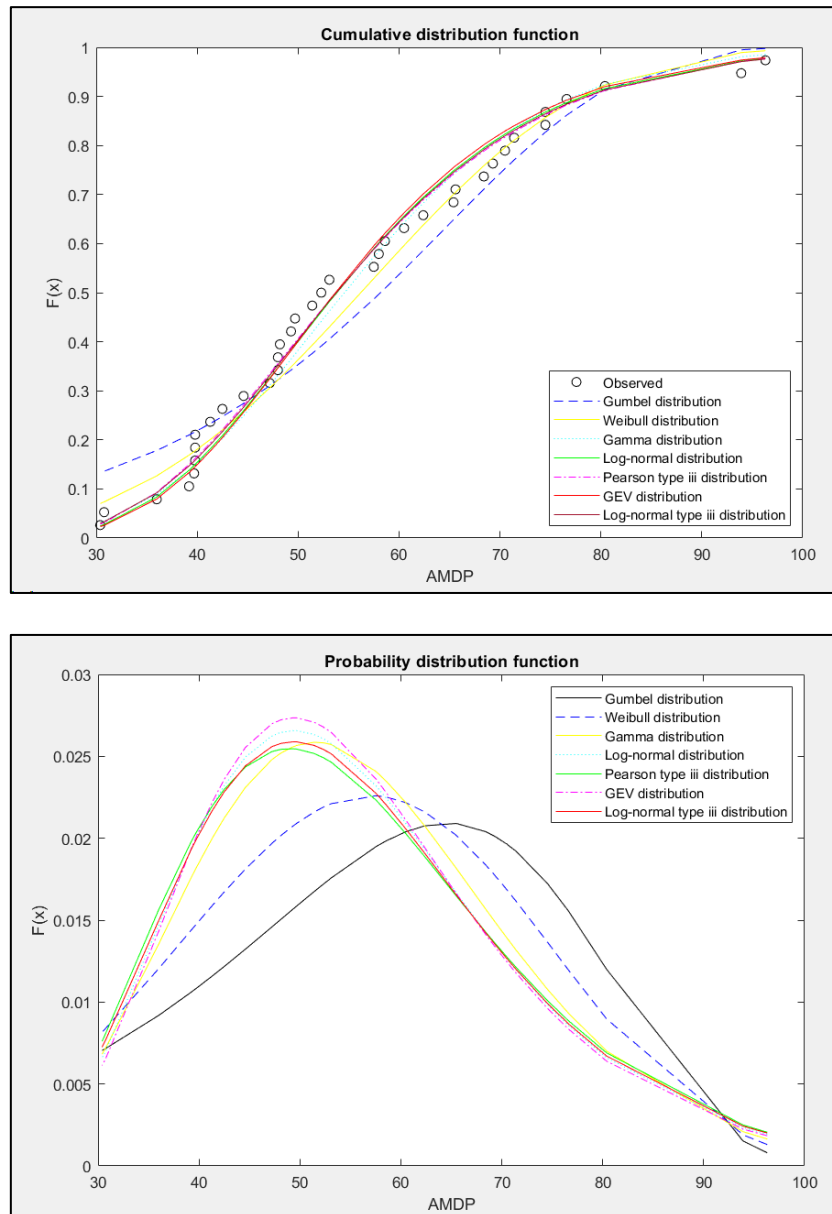
Figure 23. Summary of CDFs and PDFs adjustment to the annual maximum daily precipitation (Ermesinde station).

When assessing the accuracy of the result, it is essential to examine each distribution's fit and discard values that are far from reality. Therefore, a goodness of fit test approach is proposed to assist in rejecting possible distributions instead of choosing the best distribution (this research used Anderson-Darling (AD), Kolmogorov-Smirnov (KS), and Chi-Squared χ^2) as defined in Solaiman [64]). These algorithms calculate how well the given distribution is adjusted to the data and describe the differences between the experimental and the calculated values from the tested distribution considering a significance level of 99% ($\alpha = 0.01$).

Considering the results in Table 4, none of the distributions have reasons to be rejected. Instead, there are classified by ranking considering the p-value (for KS and χ^2 tests) and the statistic result (for the AD test). Nevertheless, to reduce the model uncertainty, Bento et al. [65] proposed a modified model average ($modified\ MM$) as an improvement of the original MM method [66]. Thus, the $modified\ MM$ method considered the arithmetic mean of the maximum daily precipitation from the mentioned probabilistic distributions. Moreover, the peak discharges were calculated applying The Giandotti method and the results are given in Table 5.

Table 4. The goodness of Fit tests – summary results.

		Weibull	Gumbel	Gamma	Log-normal	Pearson type iii	GEV	Log-normal type iii
KS	Statistic	0.09657	0.08657	0.07906	0.07572	0.0737	0.07015	0.07887
	P-Value	0.84781	0.92189	0.96073	0.973	0.97906	0.98731	0.96148
	Critical value	0.2618						
	Reject?	No	No	No	No	No	No	No
	Rank	7	6	5	3	2	1	4
AD	Statistic	0.65405	0.33431	0.27366	0.27268	0.25505	0.24229	0.26695
	Critical value	3.9074						
	Reject?	No	No	No	No	No	No	No
	Rank	7	6	5	4	2	1	3
χ^2	Statistic	2.1843	2.9682	0.86318	1.7159	1.6634	1.0137	1.1674
	P-Value	0.70191	0.39655	0.92978	0.6334	0.6451	0.79794	0.76082
	Critical value	11.345						
	Reject?	No	No	No	No	No	No	No
	Rank	6	7	1	5	4	2	3

Table 5. Calculation of Probable Maximum Daily Precipitation for different return periods.

Return Period	Probability of occurrence	*Modified MM* method - Probable maximum daily precipitation (mm)	Q (m³/s)
2	0.50	54.85	183.87
5	0.80	69.70	233.65
10	0.90	78.22	262.20
25	0.96	88.00	295.00
50	0.98	94.75	317.62
100	0.99	101.13	339.00

After performing the different empirical methodologies, the results were plotted with the confidence interval projections of the discharge to be compared (see Figure 24).
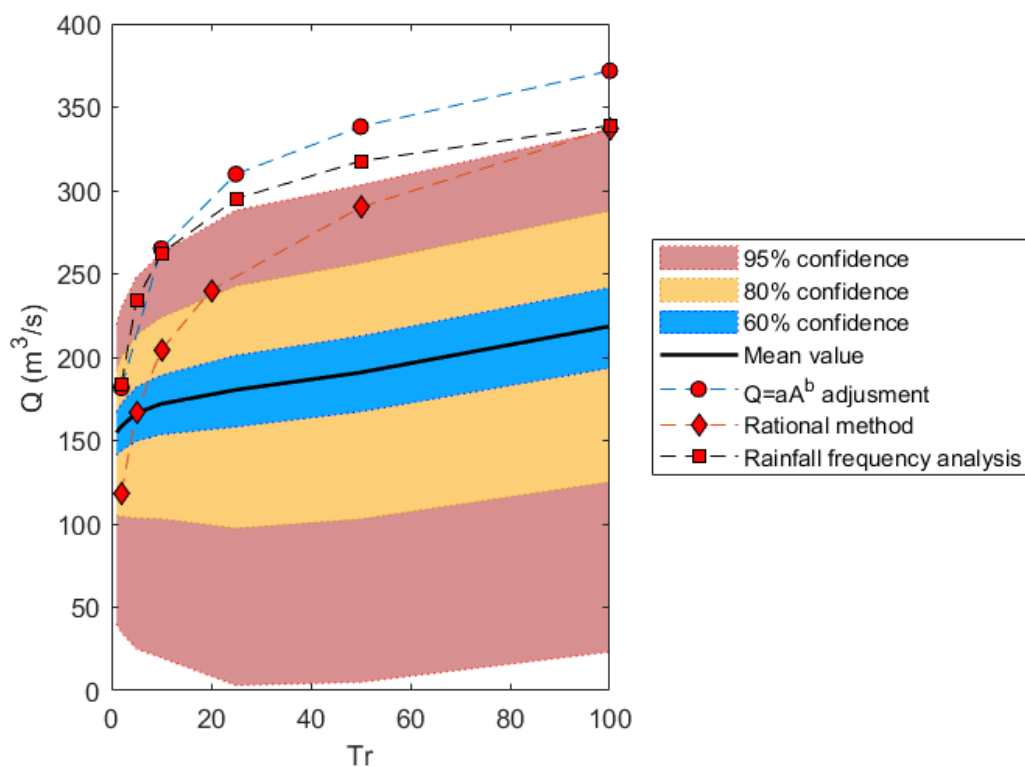
Figure 24. Comparison of estimated Q values from different empirical methods.

Two important points can be highlighted from this comparison. The first relates to the decrease in projected precipitation compared to historical data in the region. In this sense, the increase in temperatures in the most critical SSP scenarios is translated into drier seasons.

On the other hand, the presented comparison of the projected discharge and the Q calculated by the empirical method shows that the results for the 90th percentile are more similar in the less extreme return periods and can assume a conservative scenario. In addition, there is a likelihood that precipitation in the Porto region will decrease over the next few decades if the global trend in greenhouse gas emissions increases. For these reasons, the most conservative values were used to feed the hydraulic models and analyze the behavior of the extreme conditions in the study zone. The second issue relates to the accuracy of the surrogate model. Even though enough data were available to train the network and better results were obtained in the limiting ranges of the function (0 and 1), they do not represent reality because they do not reach the tendency to infinity, as a probability function would for these limiting ranges.

2.3.2.2 Hydraulic modeling

ArcMap software was used to create a Triangular Irregular Network (TIN) surface. Then, information such as altimetry, hydrography, road/railway network, buildings and bridges are collected from different sources using available databases:

i) raster data acquired from "Centro de Informação Geoespacial do Exército (IGeoE)" as part of the cartographic series of the continental territory at scale 1:25000 acquired. ii) altimetry and hydrography data at a scale of 1:10000 from the open data cartography of the Valongo city hall. iii) Digital Elevation Model (DEM) from the Shuttle Radar Topography Mission (SRTM), which provides digital elevation data with a resolution of 1 arc-second (≈ 30 m); and iv) orthophotography of the area from "Sistema Nacional de Informação Geográfica (SNIG)".

Finally, the geometric elements of the hydraulic model are drawn, such as the geometric centerline of the channel, the riverbanks, the flow path of the river, the cross-sections (152 in total) with an average spacing of 15 m, each associated with a Manning n value estimated based on the guidelines of Brunner [67], the flow obstacles (buildings, retaining walls), and the bridges along the watercourse. Figure 25 shown the generated TIN surface and the geometric elements drawn.
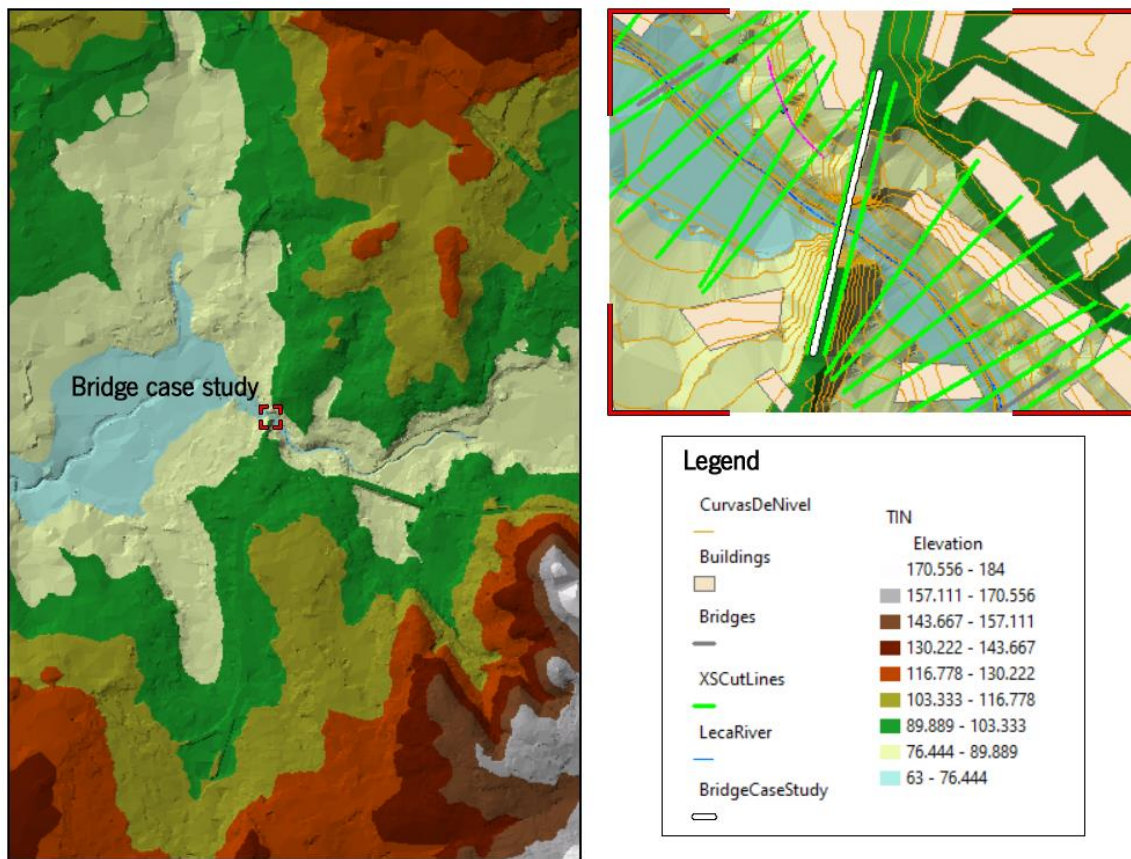
Figure 25. GIS model developed by ArcMAP software.

Then, the software HEC-RAS (version 6.0) imported the model for hydraulic calculations (see Figure 26). To define the values of peak flood discharges to be included in the model, the values estimated values in this subsection were adjusted as a function of the drainage area of the sub-catchments up to the point of the study area (see Table 6).
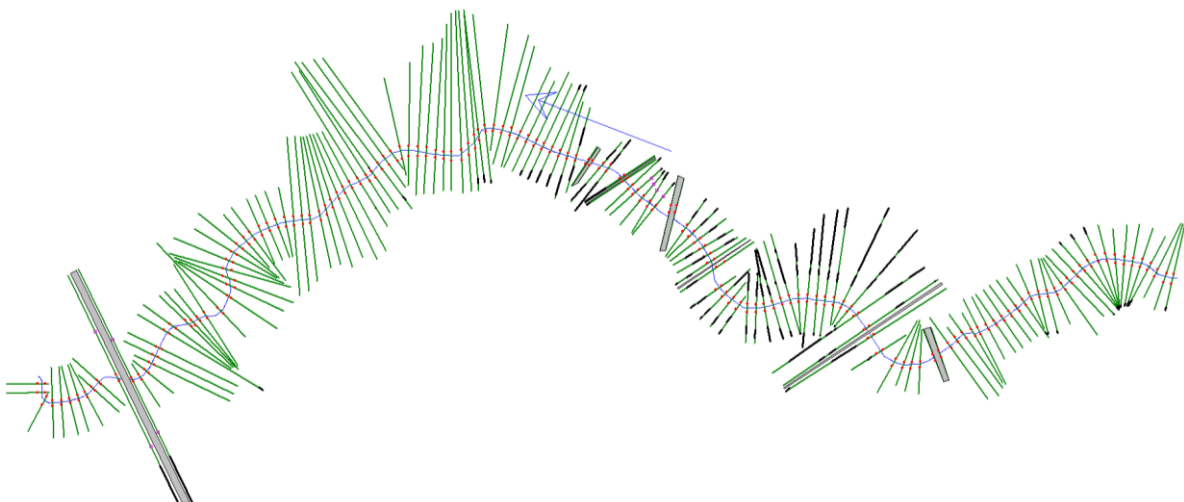
Figure 26. Imported geometry to HEC-RAS.

Table 6. Discharge values incorporated into the HEC-RAS model.

Return period (years)	Q- mean (m³/s)	Q- 90th percentile (m³/s)
2	41.45	60.11
5	43.52	64.84
10	44.97	68.59
25	47.17	75.32
50	49.89	79.3
100	57.13	87.97

In addition, the model considered a mixed flow regime calculation due to slope conditions and infrastructure along the watercourse that retards runoff. Then, the boundary conditions at all ends (downstream and upstream) were input as critical depth. After the model was fitted on the software HEC-RAS, the flood-prone areas were estimated.

Figure 27 shows the general profile of the hydraulic model containing the water surface level of the studied zone and Figure 28 shows the results of velocity and water surface level of a representative railway bridge to support further analysis in this document.
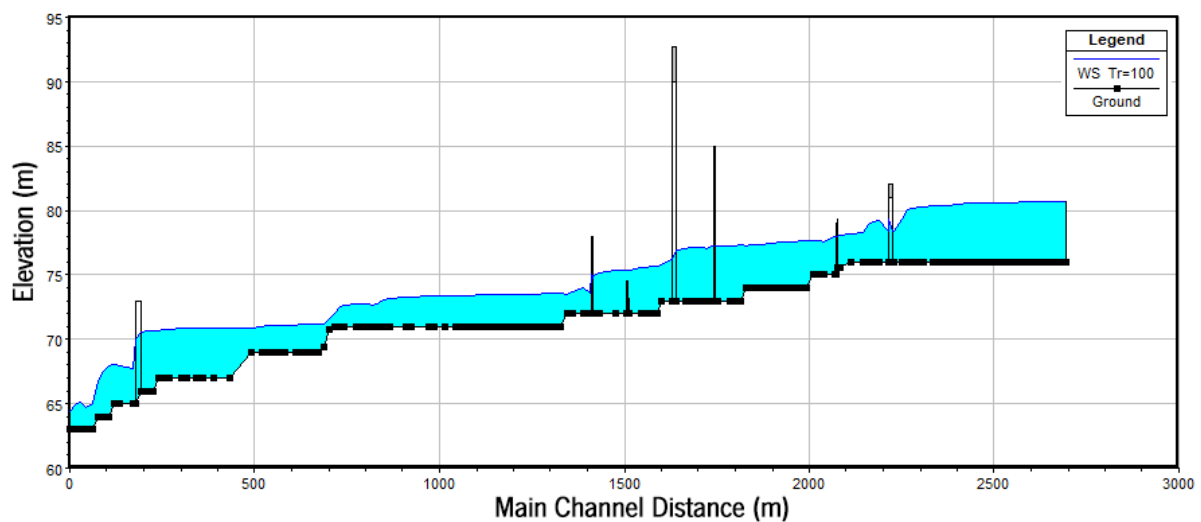
Figure 27. Hydraulic profile plot of the Leça river watershed.
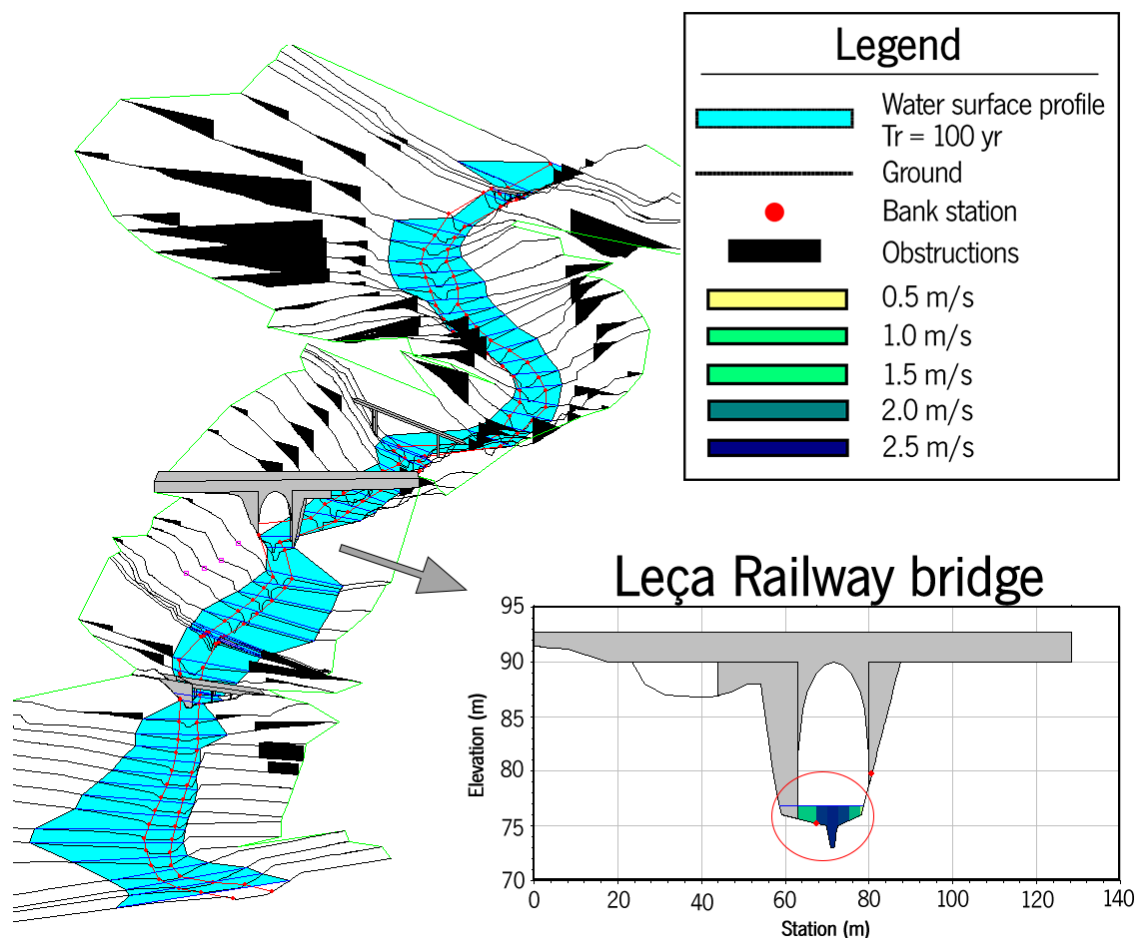
Figure 28. Hydraulic model results built within HEC-RAS software

Based on the findings from the hydraulic model, the following observations can be derived: i) Generally, the velocity along the Leça river for a return period of 100 years is between 1 and 2 m/s, which is considered a normal value for exceptional extreme events. However, the bridges in the area can cause a significant increase in velocity when the channel width is less than the bridge span. In this sense, the average maximum velocity for these zones is 5 to 6 m/s. ii) Considering a return period of 100 years, the average height of the water column along the entire channel does not exceed the limits, so there is no risk of flooding in the urban area of the studied zone.

Furthermore, the delineation of the flooded areas was enabled in a raster map using the tool RAS Mapper. Figure 29 presents the results of the mentioned variables in different raster maps to improve the visualization of the most critical scenario (Q = 87.97 m³/s with a return period of 100 years).
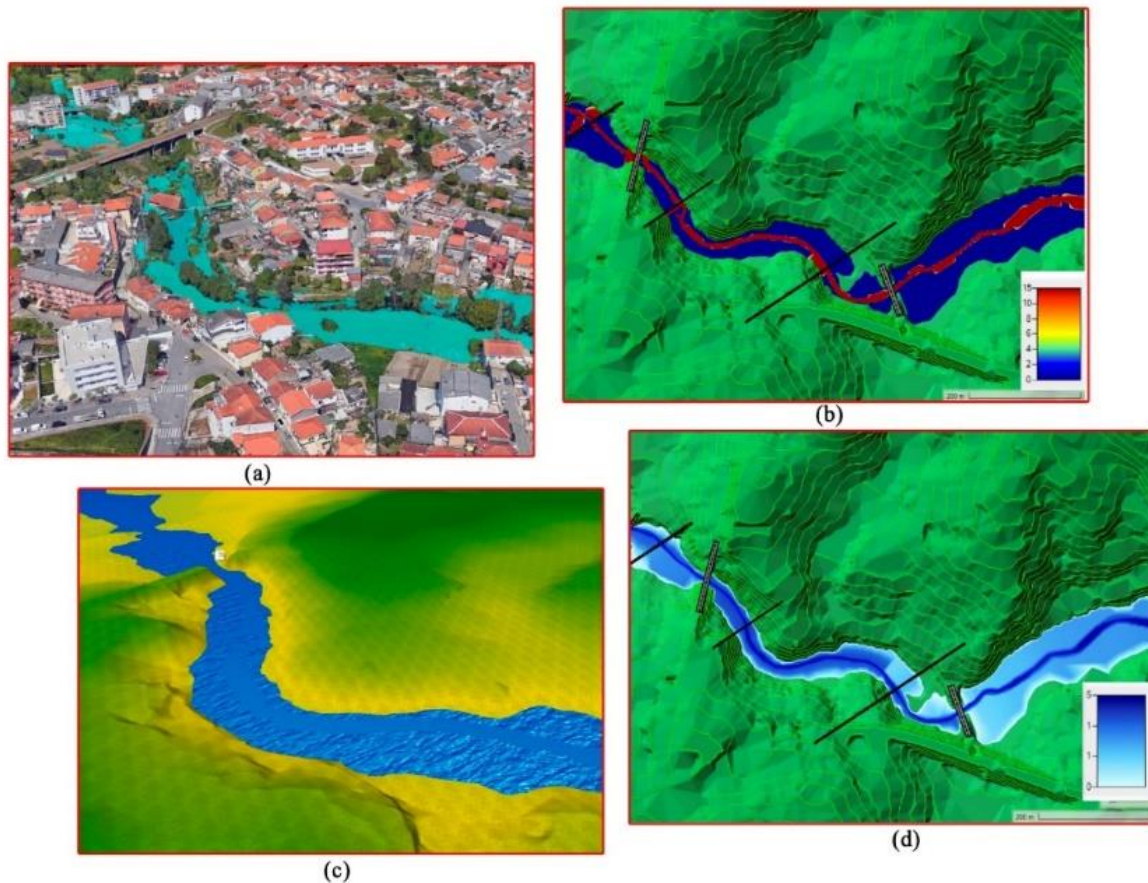
Figure 29. Illustration of the hydraulic modeling results. (a) Flood-prone areas are presented in KML format using the Google Earth view. (b) The flow velocity of the river in the original DEM. (c) 3D view of the flood-prone areas modeled in RAS Mapper. (d) Height of column water presented in the original DEM.

2.4 CONCLUSIONS

This chapter presented an ANN-based climate change framework through a watershed analysis for flood assessment. The results of the discharge estimation have shown uncertainty about the future climate. Historical rainfall records are no longer accurate and might be used as conservative estimations. Nevertheless, to obtain more optimal predictions, it is necessary to involve climate change variables that were not considered in the past. Consequently, the primary outcome of the proposed methodology is the resulting graph in Figure 22, which relates the flow peak discharge with return periods considering confidential intervals that researchers can use to include climate change in hydraulic modeling for this specific watershed. Furthermore, comparing the ANN output and the empirical hydrology method validates the results. The analysis indicates a significant difference considering all SSP scenarios, the prognostic of higher temperatures, and the increase in dryer seasons directly

affecting the watershed's flow discharge. However, it may be higher in terms of extreme event frequency.

An explicit limitation of the surrogate model was the difficulty of predicting the output close to the range values. However, as was stated, the typical probabilistic functions tend to the infinity on those ranges, and the results may improve even if the network intends to be trained using more data. Still, the ANN function cannot behave the same when probabilities approach 1.

From the flood inundation model, this specific watershed zone does not present a real urban flooding risk. The topography and the multiple structures that line the watercourse have made the site suitable for the most critical scenarios without affecting the population. However, that does not imply the existence of a risk to the zone infrastructure (i.e., bridges). High flow velocity variations have been caused by the channel contractions where the bridge infrastructure is located. In this sense, the reliability of the bridges due to the effects of floods (e.g., scour, debris, hydraulic loads) has to be assessed.
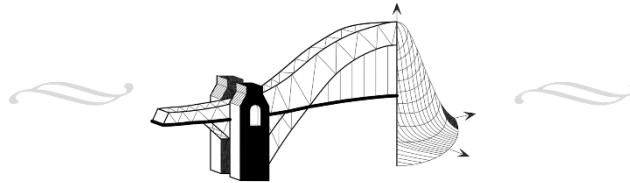
FLOOD-BRIDGE INTERACTION ANALYSIS

3.1 STRUCTURAL FAILURE REVIEW

This section is intended to review the causes and mechanisms of bridge's failure due to flooding. Therefore, the common factors induced by floods are first reviewed (e.g., scour, debris, hydraulic loads). Figure 30 summarizes the analysis of this section classifying the impacts of the hazard by levels and specifying the collapse mode [41].
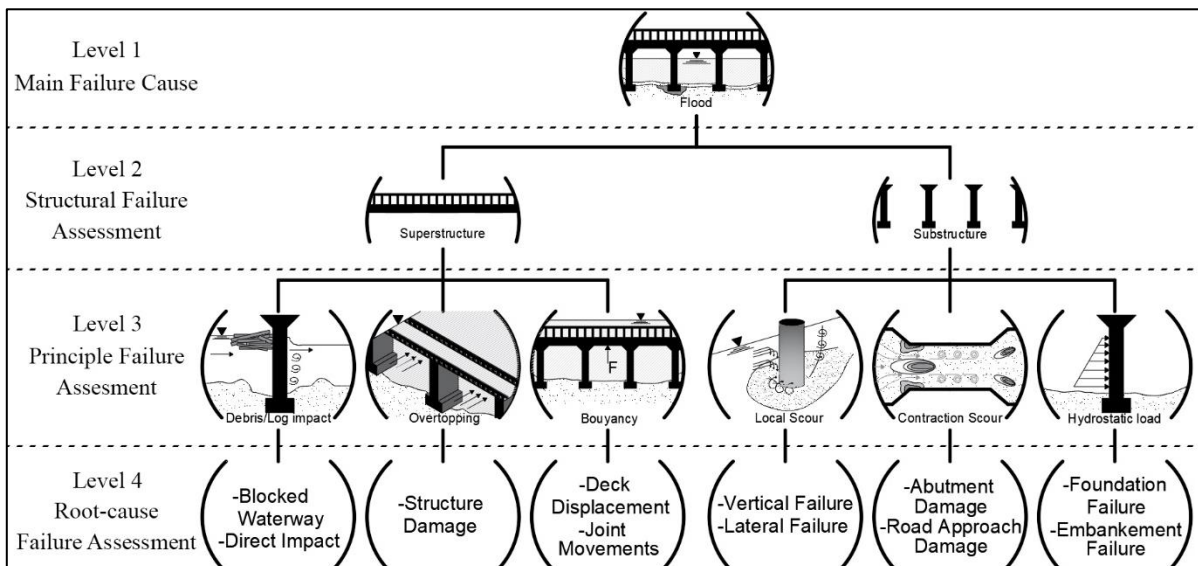
Figure 30 – Bridge failure analysis.

For this research, masonry arch bridges (MAB) are the one that requires more attention in terms of flooding events. Moreover, it is the most common type of bridge, as mentioned in

chapter 1. According to the literature [68], [69], MAB is more susceptible to flood events than other bridge typologies composed of different materials such as reinforced concrete or steel, and the foundation system of the structure can define the difference. In this sense, Hajdin et al. [68] attributed the threat increase to the MAB construction process used in the past.

Deng et al. [17] presented a systematic review of bridge collapse (causes and mechanisms), with two highlighted sections. First, the collapse mechanisms due to flood and scour, which the author categorized into four types: i) Vertical failure caused by lack of soil support and instabilities of the structural components of the foundation. ii) Lateral failure due to excess in the lateral stresses and displacements on piers and foundation. iii) Torsional failure caused by skewed flows. iv) Bridge deck failure due to buoyancy effect. Second, it defined three failure mechanisms of MAB due to statical loadings, such as the four-hinge collapse mechanism based on the contributions of Heyman [70] and Drosopoulos et al. [71], the sliding failure mode addressed by several authors [72]–[74], and a combination of the previous failure modes proposed by LimitState RING software [75]. Figure 31 shown the exposed failure mechanism.

(a) single span: 4 hinges   (b) single span: sliding only   (c) single span: hinges & sliding
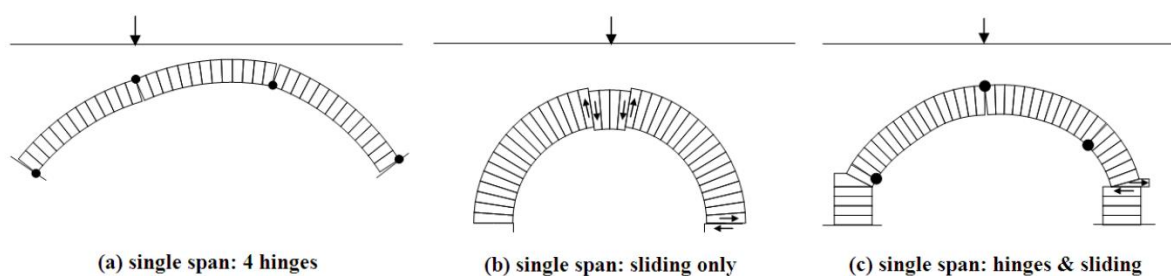
Figure 31 – Potential failure modes of single span MAB identified by LimitState:RING [75]

Once the possible mechanisms of MAB failure have been analyzed, it is necessary to know how to identify signs of these structural problems. For example, "Infraestruturas de Portugal" developed a guide to inspect bridges over rivers and identify settlement damage caused by soil scour following crack patterns. Figure 32 graphically describes noticeable cracks in MAB induced by scour, where pattern I is a diagonal crack located in the abutments and the arch; pattern II can be found on the middle span affecting the piers, the spandrel walls, the infill and the arch, and rotations cause both types of cracking due to a settlement effect.
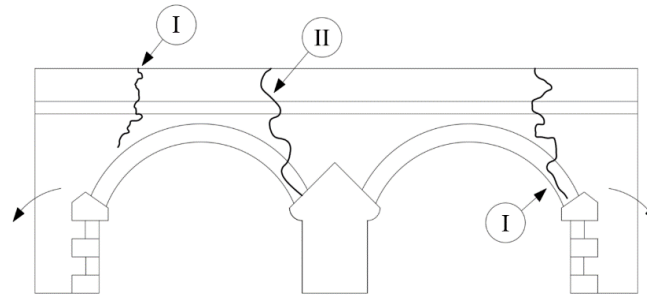
Figure 32 – Crack pattern guidelines to detect damages caused by scour effects.

Past flood events have exposed several modes of collapse that can be learned and assessed. In the literature, several examples can be found where the structural failures of MAB are analyzed, where the main weakness of MAB is its lack of resistance to tension. The Federal Highway Administration (FHWA) [76] shown an example of the fragmentation of one of the intermediate columns (see Figure 33a). Zampieri et al. [77] analyzed two examples, one where the failure mode was symmetric in the plane, causing the collapse of the arches in two spans (see Figure 33b), and the other with the exact mechanism but without symmetry (see Figure 33c).
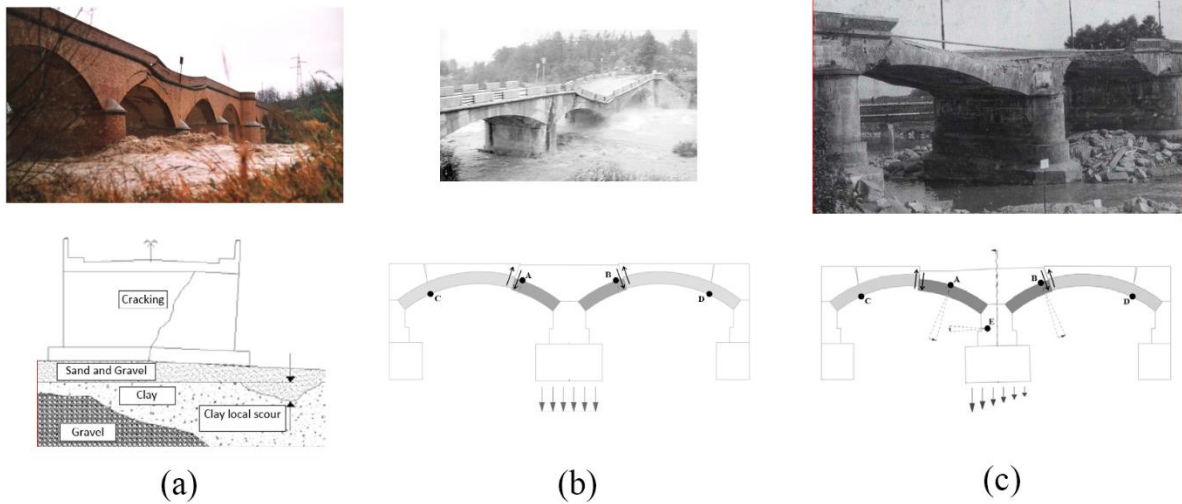
Figure 33 – Historical MAB collapses and failure modes, adapted from [78]

3.2 FLOOD EFFECTS INTERACTION METHODOLOGIES

3.2.1 SCOUR

As reviewed in section 2.1, the hydraulic action of the flowing stream during the flood may cause scour at bridge piers, leaving this phenomenon as the primary cause of bridge failures

worldwide. Scour is a phenomenon where the riverbed is reduced by underwater erosion [79]. Nevertheless, the susceptibility to local scour is presented by the normal flow around piers and abutments. Moreover, bridges spanning over rivers represent an obstacle inducing a decrease in the cross-section of the river. This reduction implies variations in the water flow, thus known by the name of contraction scour [17], [41].

Scour depth estimation on a bridge foundation has been challenging for engineers and an important research field. The current approaches for maximum scour depth calculation are based on: i) the variables characterizing the flow (e.g., velocity, slope); ii) the bed material; and iii) the geometry of the bridge [80].

The knowest expressions for the scour depth estimation are proposed by: Melville [81], [82], Richardson and Davis [83], Sheppard and Miller [84], and Sheppard-Melville [85]. Each method is based mainly on scour for cylindrical piles, where applying more minor variations allows for more complex cross-sections.

The methodology proposed by Richardson and Davis [83] shown in equation (9) has been used by the US HEC-18 manual in the past decades for scouring calculation, and it is an adaptation of the Colorado State University (CSU) equation published in 1975 [86].

$$\frac{y_s}{a} = 2.0k_1k_2k_3 \left(\frac{y}{a}\right)^{0.35} F_r^{0.43} \qquad (9)$$

Where y_s is the scour depth, y is the flow depth, a is the pier width, F_r is the Froude number; k_1, k_2 and k_3 are a factor for pier shape, flow angle of attack of flow and movement state of bed material, respectively.

The methodology proposed by Melville [82] in equation (10) is used in several countries and provides extensive coverage of parameters that influence scour. It is being combined with the method developed by Sheppard and Miller [84].

$$\frac{y_s}{a^*} = 2.5f_1f_2f_3 \qquad (10)$$

Where f_1 depends on $\frac{y}{a^*}$; f_2 of $\frac{v}{v_c}$ and f_3 of $\frac{a^*}{D_{50}}$. Where a^* is an effective diameter of a circular pile, V is the flow velocity, V_c is the critical flow velocity and D_{50} is the median grain size of the riverbed material.

Regarding the contraction scour estimation, the methodologies are based on the conservation of sediment transport, and it is necessary to determine the scour type (live-bed scour or clear-water scour). In the case of live-bed scour, the equilibrium of the developed bridge scour is reached when sediment transported into the contracted section equals sediment transported out. As scour develops, the shear stress decreases (in the contracted section) due to a decreasing velocity and the flow area increase. Moreover, maximum scours occur when shear stress reduces to the minimum while maintaining the equilibrium conditions. For clear-water scour, there is no sediment transport into the contracted section. Moreover, maximum scour occurs when shear stress reaches the critical shear stress of the bed material in the section. Typically, for both types of contraction scour, the width of the contracted section is constrained, and depth increases until the limiting conditions are reached [86]. To determine if the upstream flow is transporting bed materials, the critical velocity for the beginning of motion V_c of the particle D_{50} must be calculated and compared with the main velocity of the flow in the main channel or the overbank area upstream of the bridge opening. Figure 34 presents a flowchart describing that condition.
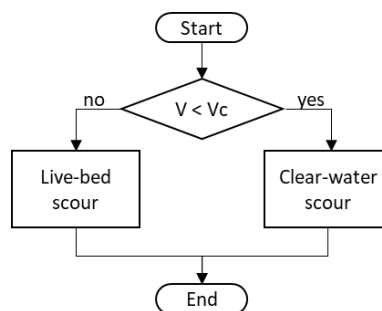
Figure 34 – Flowchart of the conditional to determine the type of contraction scour.

The main velocity is determined following the equation (11) (Manning equation), and to calculate the critical velocity is used equation (12):

$$V = \frac{1}{n}R^{2/3}S^{1/2} \tag{11}$$

$$V_c = 6.19h^{1/6}D_{50}^{1/3} \qquad\qquad (12)$$

Where R is the hydraulic radius, S is the slope of the channel at the point of measurement, n is the surface roughness (based upon channel material and condition), h is the flow depth, D_{50} is the median grain size of the river bed material, V is the flow velocity and V_c is the critical velocity above which bed material of size D_{50} and more minors will be transported. A classical methodology summarized in Table 7 is being used based on the modified version of the Laursen equation [87], adopted by the US HEC-18 [86] for both types of contraction scour (live-bed scour or clear-water scour).

Table 7. A modified version of the Laursen equation for contraction scour.

Type	Equation	Description	
Live bed	$\dfrac{Y_2}{Y_1} = \left(\dfrac{Q_2}{Q_1}\right)^{\frac{6}{7}}\left(\dfrac{W_1}{W_2}\right)^{k_1}$ $Y_s = Y_2 - Y_0$	y_1	The average depth in the main upstream channel
		Y_2	The average depth in the contracted section
		Y_0	Existing depth in the contracted section before scour
		Q_1	Flow in the upstream channel transporting sediment
		Q_2	Flow in the contracted channel
		W_1	The bottom width of the main upstream channel that is transporting bed material
		W_2	The bottom width of the main channel in the contracted section less pier width
		k_1	Exponent determined in Table 8
		Y_s	Average contraction scour depth
Clearwater	$Y_s = \left(\dfrac{0{,}025Q^2}{1{,}25D_{50}{}^{2/3}W^2}\right)^{\frac{3}{7}}$	Q	Discharge through the bridge or on the overbank set-back area at the bridge associated with the width W
		D_{50}	The median diameter of bed material
		W	The bottom width of the contracted section less pier width

In order to compute the coefficient of k_1 to estimate the clear water scour is used equation (13). Where V^* is the shear velocity in the upstream section, T is the fall velocity of bed material based on the D_{50}, g is the acceleration of gravity, S_1 is the slope of energy grade line of the main channel, ϑ_o is the shear stress on the bed and Δ is the density of water.

$$V^* = \left(\frac{\vartheta_o}{\Delta}\right)^{1/2} = (gy_1S_1)^{1/2} \tag{13}$$

Regarding the calculation of the local scour on the abutments, some methods exist for its determination: Liu et al. [88], Laursen [89], Froehlich [90], Highways in River Environment (HIRE) provided by the United States Army Corps of Engineers, and Melville [91]. However, the uncertainty for calculating the local scour in abutments is higher than in piers due to the results exceeding the phenomenon's reality. Equations for the calculation of abutment scour are based on laboratory data, and very little field data exists for verification. Almost all the equations result in conservative values of scour because the main channel riverbed is considered an alluvial and assumes that the obstructed water flow is proportional to the length of the abutment, which is unlikely to occur in reality.

Table 8. Coefficient values of k_1.

V^*/T	k_1	Mode of Bed Material Transport
$< 0{,}50$	0,59	Mostly contact bed material discharge
$0{,}50\ to\ 2{,}0$	0,64	Some suspended bed material discharge
$> 2{,}0$	0,69	Mostly suspended bed material discharge

The methodology proposed by Froehlich [90] and represented by equation (14) is based on dimensional and regression analysis of laboratory data. HEC-RAS recommends its use for both live-bed and clear water scour, for abutments into the main channel or not, and for concentrated flow in the main channel or combined with flow over flooding zones. Table 9 shows each of the used variables in the Froehlich methodology and their description.

$$Y_s = 2{,}27K_1K_\theta\ L^{0{,}43}\ F_{re}^{\ 0{,}61}\ Y_a^{0{,}57} + Y_a \tag{14}$$

$$K_\theta = \left(\theta/90\right)^{0,13} \tag{15}$$

As this methodology is considered conservative, adding Y_a is recommended only for design purposes. In this sense, for assessment or prediction of the scour events, the addition can be dismissed.

Table 9. Variables for abutment scour calculation.

Variable	Description
L	Length of abutment
$\mathbf{Y_s}$	Scour depth
$\mathbf{K_\theta}$	Angle of attack of flow with abutment factor
θ	Angle of attack of flow
$\mathbf{F_{re}}$	Froude number
$\mathbf{Y_a}$	Average depth of flow
$\mathbf{A_e}$	Flow area obstructed by the abutment and embankment
$\mathbf{K_1}$	Abutment shape factor

3.2.2 HYDROSTATIC LOADS

There are two effects produced by the resistance to flow: i) shear resistance, and ii) resistance resulting from the difference in pressure between the upstream side to the downstream side of an object, which creates a drag force. Thus, structures are obstacles to the normal flow of the river, generating resistance and causing a deflection of the streamlines and a local acceleration of the fluid. Moreover, this effect depends on the shape of the boundary of the object (i.e., a bridge pier). Consequently, another effect (normal stress) occurs due to the change in pressure from the upstream to the downstream side of the object boundary. The summation of the forces over the surface of the object thus results in a drag force and a pressure resistance [41].

The hydraulic design of safe bridges of the US Department of Transportation (Federal Highway Administration) [92] specified the methodology to estimate the hydrodynamic flow pressures

such as drag force and lift force for bridge piers (see equations (16) and (17)). Figure 35 describes the forces diagram when the structure's body is submerged during a flood (or normal flow condition).

$$V^* = \left(\frac{\vartheta_o}{\Delta}\right)^{1/2} = (gy_1S_1)^{1/2} \qquad (16)$$

$$V^* = \left(\frac{\vartheta_o}{\Delta}\right)^{1/2} = (gy_1S_1)^{1/2} \qquad (17)$$

Where F_d is the Drag Force, C_d and C_L is the drag and lift force coefficient depending on the pier shape, V_u is the upstream flow velocity, A_d and A_L are projected areas of the pier respecting the flow angle.
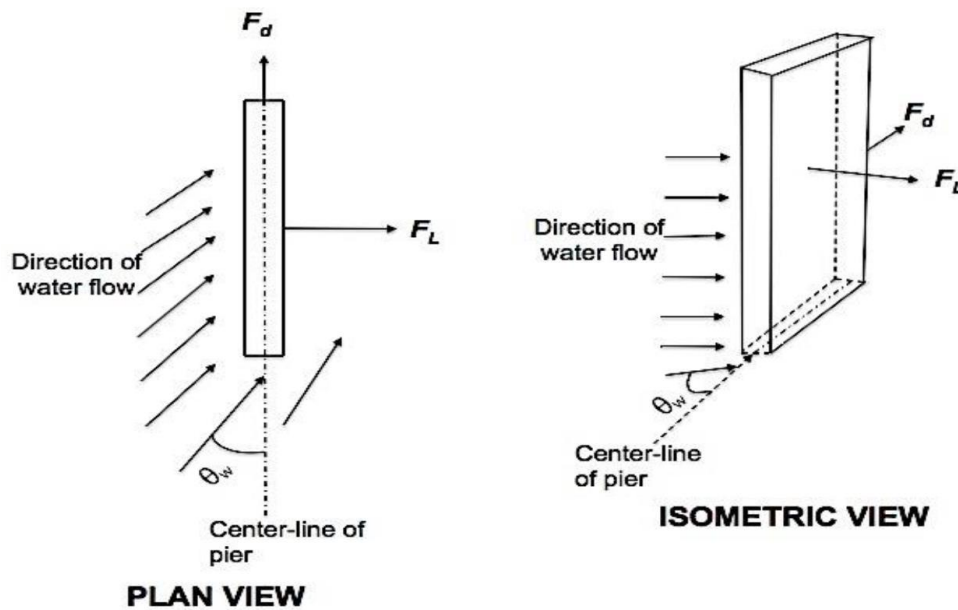
Figure 35 – Drag Force (F_d) and Lift Force (F_L) on submerged bridge piers and abutments obtained from [93].

Besides the resistance effect to the flow of the substructure, the hydrostatic force must be considered if any imbalance in the water surface elevation exists. Otherwise, the hydrostatic forces are evaluated depending on the elevation upstream and downstream of the bridge. The pressure of the water weight on the structural element surface is calculated following the equation (18). Thus, the pressure is most significant at the lowest point of a submerged element, and it is zero at the water surface elevation.

$$P_h = \gamma_w H \qquad\qquad (18)$$

Where P_h is the hydrostatic water pressure, γ_w is the specific weight of water (9.81 kN/m^3), and H is the flow depth.

3.2.3 OVERTOPPING FLOW

The hydraulic design of safe bridges of the US Department of Transportation (Federal Highway Administration) [92] defined overtopping flow as the condition in which flow crosses over the roadway approaches or the bridge deck itself. Overtopping flow conditions can be assumed as a broad-crested weir since the deck is elevated above the floodplain grade, the dimension of the crest in the direction of flow (e.g., across the road) is broad, and the overtopping depth is comparatively shallow.

The overtopping flow induced by the rising water level causes an erosion effect, which results in the downstream side collapse through the washout of the bridge supports. Moreover, the flow velocity increases, deteriorating the infrastructure's lateral sides of the infrastructure itself [94]. Nevertheless, this phenomenon is analogous to the overtopping erosion of dams or embankments [95].

It is possible to apply the methodology proposed by several authors [96], [97] to estimate the critical time of erosion capable of leading to instabilities. It is conceived first for dam assessment and then extended to the crossing road case. The mechanics of dam erosion assumes that the water accumulated upstream of the occluded crossing road acquires potential energy that can be transformed into mechanical energy. In this sense, the erosion model of a bridge can be represented by a trapezoidal shape (assuming a single span) defined by a hydraulic ratio. Thus, to evaluate the flow and the mechanical condition of the water, it is necessary to fix some boundary conditions due to the cross-section increasing its transverse area and slope caused during the erosion.

Figure 36 shows the different modes of the riverbed erosion that may take place; (a) the erosion causes the steepening of the lateral side, increasing the possibility of a lateral collapse; (b) it is characterized by a direct erosion of the lateral side; (c) involves a homothetic erosion of the whole section.

The erosion of the section also depends on the material properties. Empirical equations proposed by Chang et al. [97], Zhang and Chang [96] for dams are the following:

$$K_d = 20075e^{4.77}C_u{}^{-0.76} \qquad (19)$$

$$\tau_c = 6.80(PI)^{1.68}P^{-1.73}e^{-0.97} \qquad (20)$$

Where K_d is the coefficient of erodibility, τ_c is the critical shear stress initiation of the soil erosion, e is the void ratio, C_u is the coefficient of uniformity, PI is the plasticity index, P is the fines content.
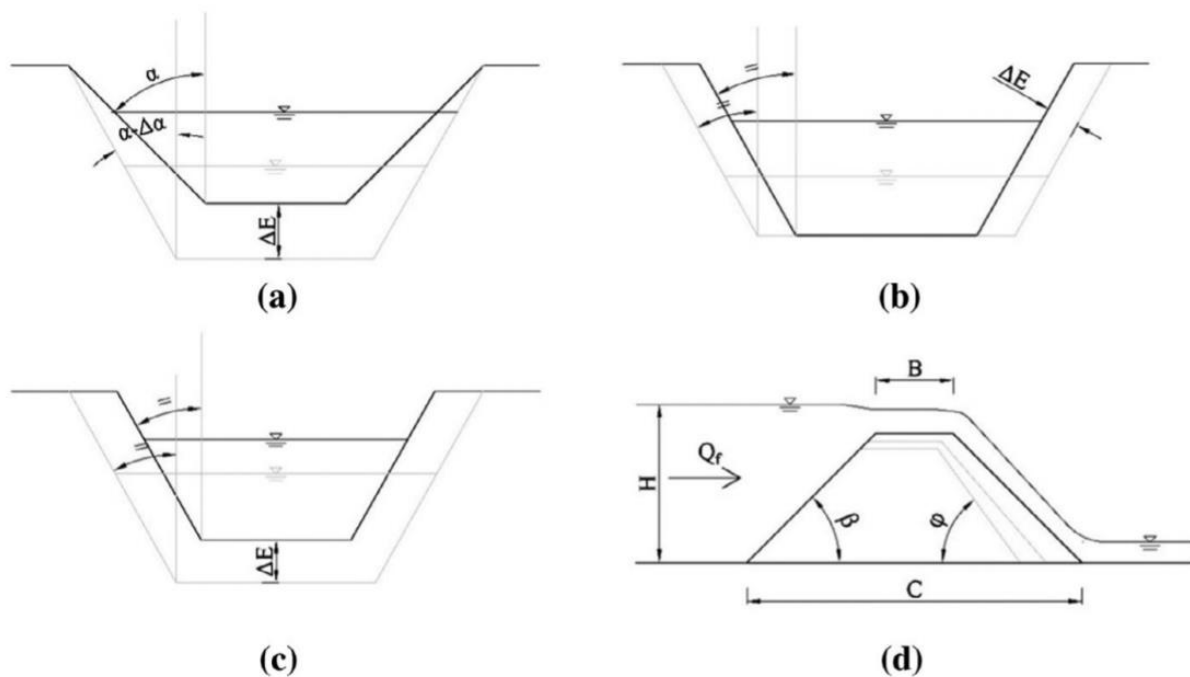
Figure 36 – Erosion of the transverse section: (a) bed of the river; (b) whole cross section; (c) lateral embankment; and (d) longitudinal Section. Obtained from [94].

This formulation is recommended for soils characterized by a content of fine parts higher than 10%. For granular subsoil, the erosion mechanism relates to aggregates' dimension; a possible formulation is Annandale's equation [98].

$$\tau_c = \frac{2}{3}gD_{50}(\rho_s - \rho_w)\tan\varphi \qquad (21)$$

Where g is the gravitational acceleration, ρ_s is the soil mass density, ρ_w is the water mass density, D_{50} is the mean gravel size, φ is the friction angle.

3.2.4 BUOYANCY FORCE

Buoyancy is an uplift force equivalent to the weight of water displaced by the submerged element. This force must be considered if the superstructure and substructure design elements incorporate empty voids as with a box-girder or if air pockets develop between girders beneath the deck. Thus, to evaluate the buoyancy force, designers must estimate the water surface elevation upstream and downstream of the bridge [92]. Recent studies provide guidelines to evaluate the stream pressure and forces on submerged bridge superstructures. For example, the report "Hydrodynamic Forces on Bridge Decks" FHWA [99] proposed a physical model combined with a three-dimensional computational fluid dynamics (CFD) modeling in order to understand the behavior of hydrodynamic forces on inundated bridge decks. Three specific forces are acting in the superstructure (see Figure 37): i) The drag force applying parallel to the flow direction and tending to push the superstructure off of the piers and the abutments. ii) The lift force applying vertically and tending to lift the superstructure. iii) The overturning moment resulting from unevenly distributed forces and tending to rotate the superstructure about its center of gravity.
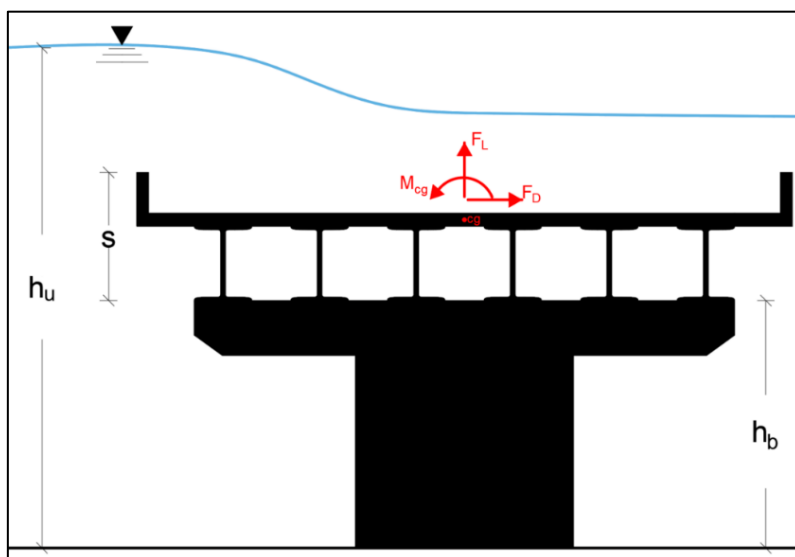
Figure 37 – Sketch for drag, lift, and turning moment variables.

FHWA [99] provided the equations for computing drag, lift, and moment per unit length of the bridge, which are summarized in Table 10.

Table 10. Equations for computing hydrodynamic forces on inundated bridge decks.

Type	Equation	Description	
Drag Force	$$F_D = \frac{\rho C_D V^2 s}{2}; \; h^* > 1$$ $$F_D = \frac{\rho C_D V^2 s h^*}{2}; \; h^* < 1$$ $$h^* = \frac{h_u - h_b}{s}$$	ρ	density of water
		C_D	Drag coefficient
		V	Flow velocity
		s	See Figure 37
		h_u	See Figure 37
		h_b	See Figure 37
Lift Force	$$F_L = \frac{\rho C_L V^2 W}{2}$$	C_L	Lift coefficient
		W	Deck length
Overturning Moment	$$M_{cg} = \frac{\rho C_M V^2 W^2}{2}$$	C_M	Moment coefficient

3.2.5 DEBRIS

The accumulation of flood debris is one of the most unpredictable problems. The hydraulic design of safe bridges of the US Department of Transportation (Federal Highway Administration) [92] defined debris as the floating or submerged material, such as logs, vegetation, or trash, transported by a stream, damaging bridges by individual pieces of debris or debris mats colliding with structural components. Usually, debris forces cause superficial damage such as spalling concrete from girders, the decks, or piers. Moreover, the water forces on the bridge due to the river/stream flow and debris accumulation (hydrodynamic and hydrostatic forces, see Figure 38) may result in failures.

The hydrodynamic and hydrostatic debris forces can be enough to i) overturn bridges; ii) shear bridge roadway decks off their supports; iii) cause the buckling failure of the substructure. Even more, debris collection increases the upstream flooding due to the reduction of the waterway opening, causing an increase in all scour types (e.g., contraction scour is increased when debris blocks a portion of the bridge opening, and pressure scour is increased when debris collects on the bridge deck and girders) [100]. Regarding computational debris models,

several authors suggest where the pier is modeled to increase the width of the pier by the area of the blockage. Nevertheless, it might be necessary to define some flow areas as ineffective depending on the obstruction size (see Figure 39)[92].
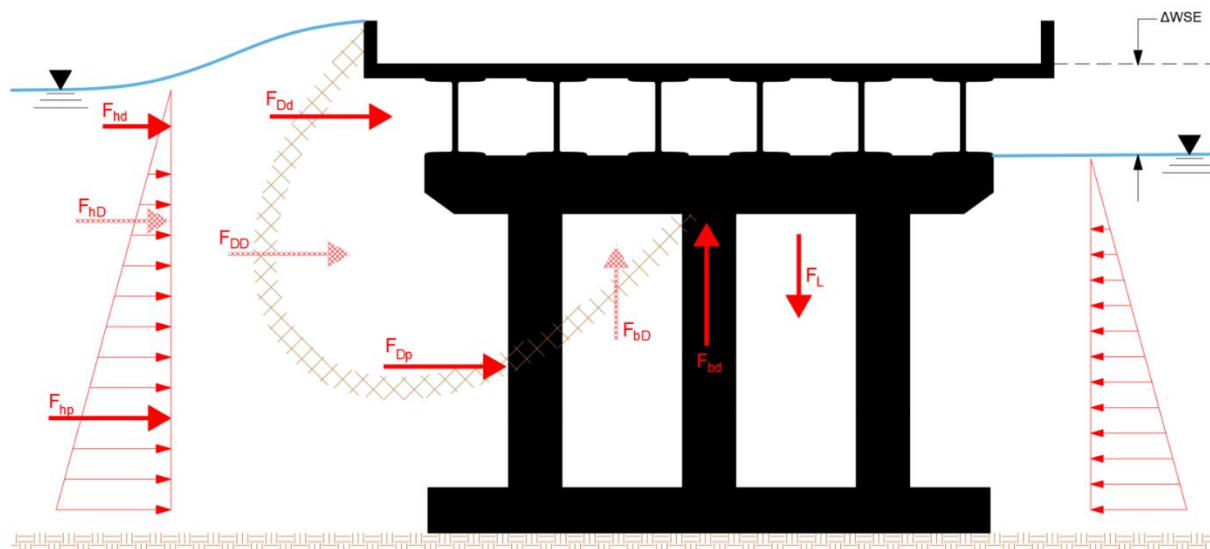
Drag Forces
F_{Dd}-Deck
F_{DD}-Debris
F_{Dp}-Pier

Hydrostatic Forces
F_{hd}-Deck
F_{hD}-Debris
F_{hp}-Pier

Lift Forces

F_L-Deck

Buoyant Forces
F_{bd}-Deck

F_{bD}-Debris

Figure 38 - Hydraulic forces on bridge system with debris.
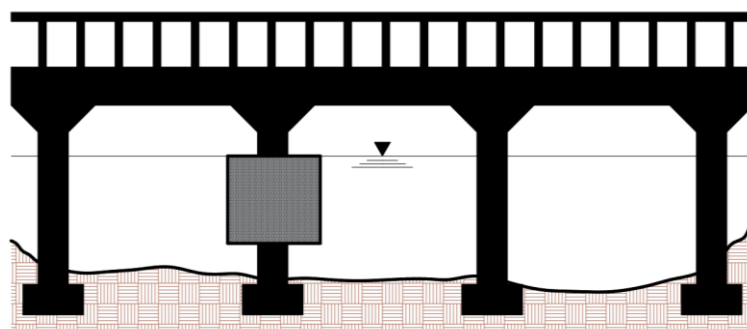
Figure 39 – An example of an upstream bridge cross-section with debris accumulation on a single pier [92].

3.3 SCOUR MODELING IN HEC-RAS - CASE STUDY: LEÇA RIVER RAILWAY BRIDGE

As a continuation of the hydraulic analysis executed in section 2 of this document, it was proceeded to analyze one of the bridges in the watershed (See Figure 40) according to the guidelines introduced in this section.
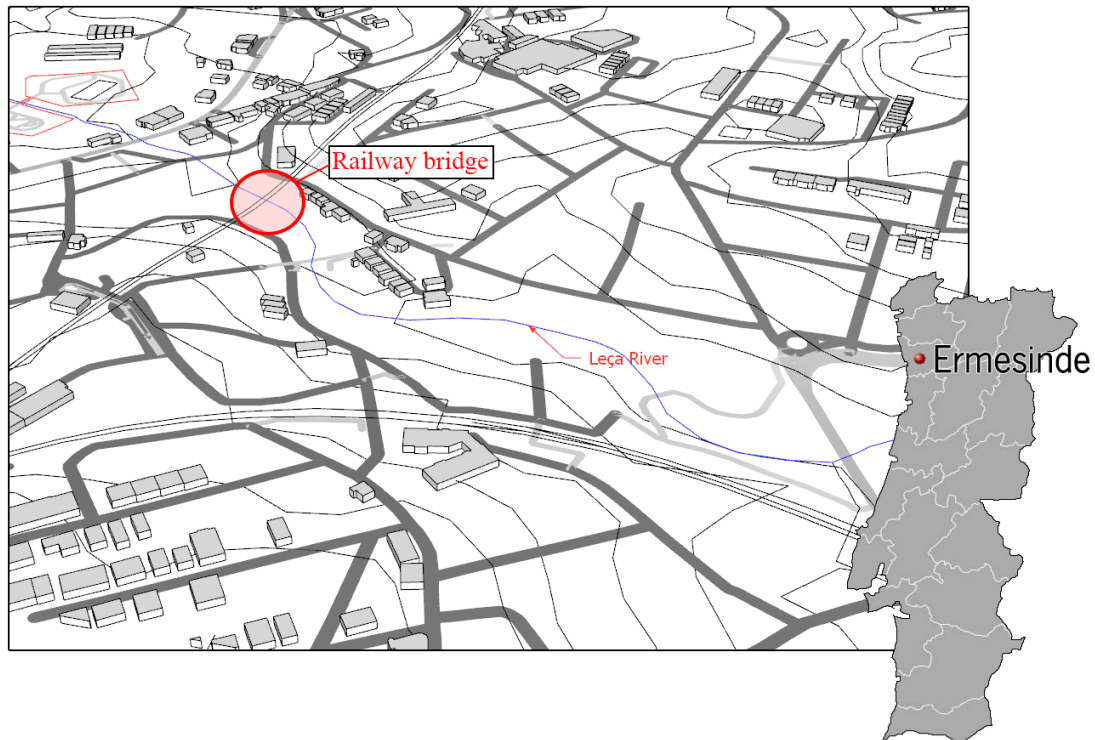
Figure 40 – Leça railway bridge location.

The scour model was generated using the HEC-Ras software based on the hydraulic model and hydrological information collected in section 2. In addition, it is necessary to gather new details such as the geometry of the structure and the bed soil conditions and thus be able to estimate the scour depth using maximum flow discharge related to a return period. In this sense, the required information is obtained through the geotechnical studies of the bridge design and the literature.

The geometry editor of HEC-RAS was used to enter the geometry data of the bridge, where all the topography constrains were drawn. First, the position of the bridge position was defined according to the GIS mapped location. Then, the bridge cross-section was added between the defined river cross-sections, including the upstream and downstream dimensions of the substructure and superstructure. Figure 41 shows the modelled bridge in the HEC-RAS geometry editor.
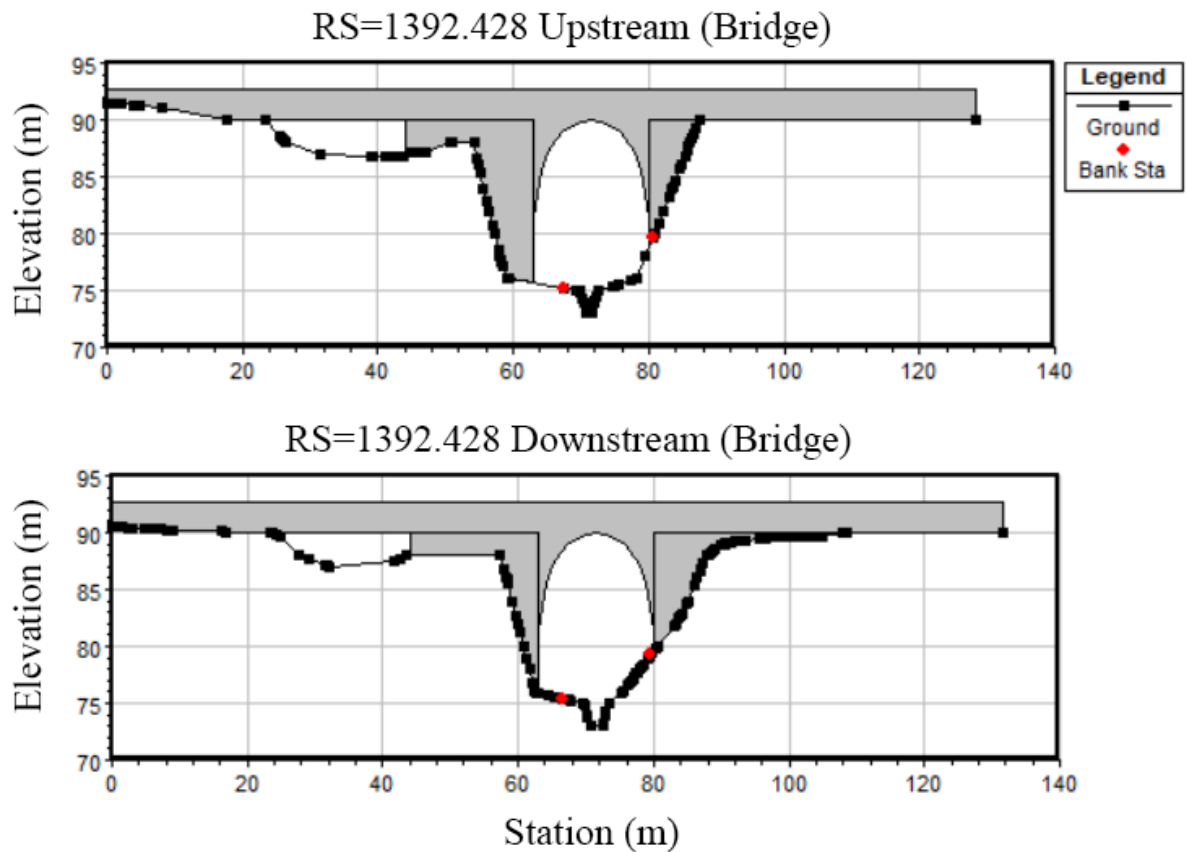
Figure 41. Input geometry of the railway bridge in the HEC-RAS geometry editor.

The hydraulic design function of HEC-RAS has performed the analysis of the scour bridge. However, it is necessary to characterize the riverbed's material, which is represented by the size of the particles. According to the geotechnical information provided by Soares et al. [57], the soil in this area is mainly composed of Porto granite, classified in a degree of alteration of W_{III} according to the classification proposed by the International Society of Rock Mechanics (ISRM) [101] and the International Association of Engineering Geology (IAEG) [102].

Table 11 describes each degree of alteration based on qualitative criteria such as intensity of discoloration and preservation of structure. Although there are many new methods for classifying granitic rocks in the literature and most of them consider quantitative variables as geomechanically parameters [103]; this assessment exceeds the scope of this research.

Table 11. Classification of alteration degrees in granitic rocks [104].

Grade	State	Description
W_I	Fresh	There are no visible signs of weathered, only a slight discoloration.
W_{II}	Slightly weathered	The bedrock discoloration indicates a weathered.
W_{III}	Moderately weathered	Less than 35% of the rock is weathered. Fresh material remains in the bedrock.
W_{IV}	Highly weathered	More of the 35% of the rock is weathered.
W_V	Completely weathered	All the rock material is weathered for soil. However, the original rock structure is still preserved.
W_{VI}	Residual soil	All material was converted to the soil. The bedrock structure is destroyed.

Among the documents collected by the IP, there is a geotechnical report that evaluates the condition of the soil. In addition, several standard penetration tests (SPT) and dynamic penetration tests (DPT) were performed at the locations shown in Figure 42.
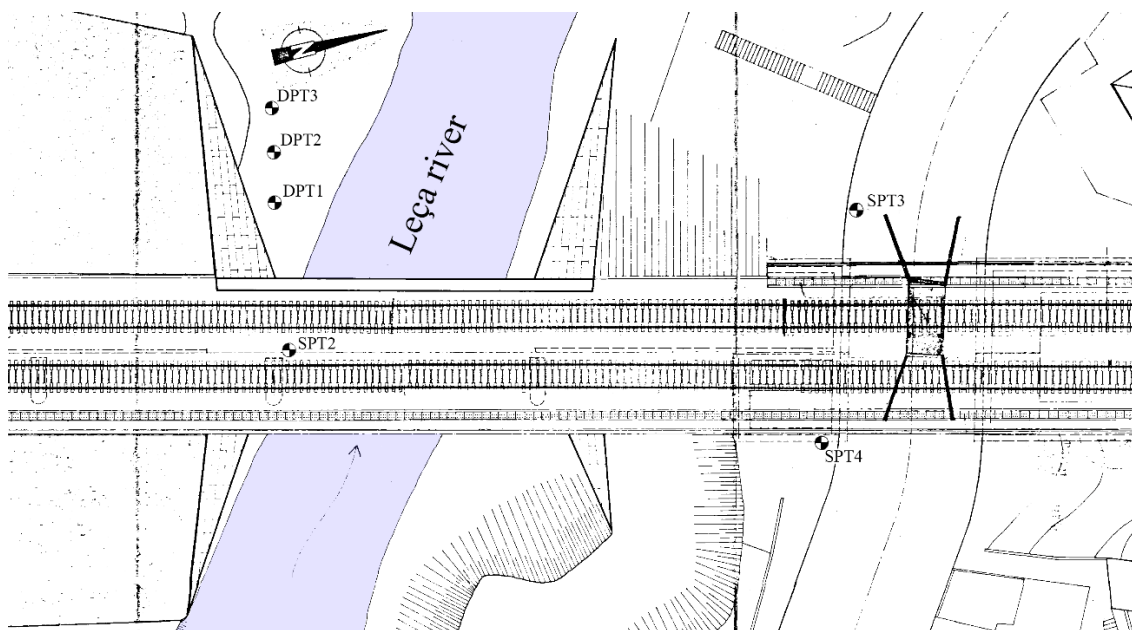
Figure 42. Location of the performed standard and dynamic penetration tests.

As a result, the soil profile was drawn, and the mechanical properties were defined. According to this, under the organic profile there is an alluvial area, which is specifically composed of sandy gravel, which is a residual soil of the bedrock (see Figure 43).
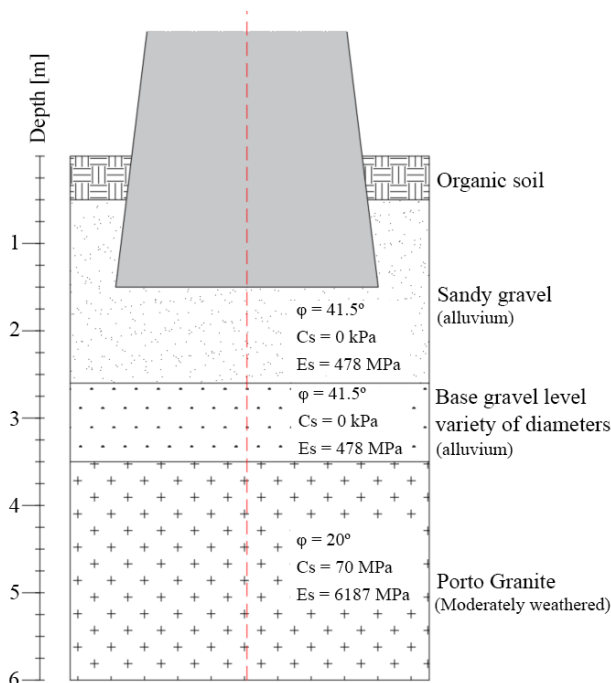
Figure 43. Soil profile of the bridge abutment at Leça river.

For the calculation of contraction scour, it is necessary to define the factor D_{50}, which is related to the grain size of the riverbed. In this sense, the value of D_{50} for the Leça river was determined using a granulometry distribution of the residual Porto granite soil presented by Viana da Fonseca et al. [105]. Consequently, the distribution shown in Figure 44, which contains ~100 samples, corresponds approximately to the D_{50} of 0.35 mm.

The D_{50} of soil information is entered to calculate the contraction scour depth and the local scour depth at the abutments. Therefore, in HEC-RAS, the total scour depth is estimated as the sum of the local and contraction scour depths. First, the contraction scour was calculated using the equation for live bed contraction scour (see Table 7). Moreover, abutment local scour depth was calculated using the Froehlich equation [90]. Then, the analysis of the hydraulic design function was performed in HEC-RAS considering the discharge scenarios given in Table 6. Consequently, the graphical representation of the calculated scour depth is developed by the software and displayed in Figure 45. At the same time, all the results are displayed in Table 12.
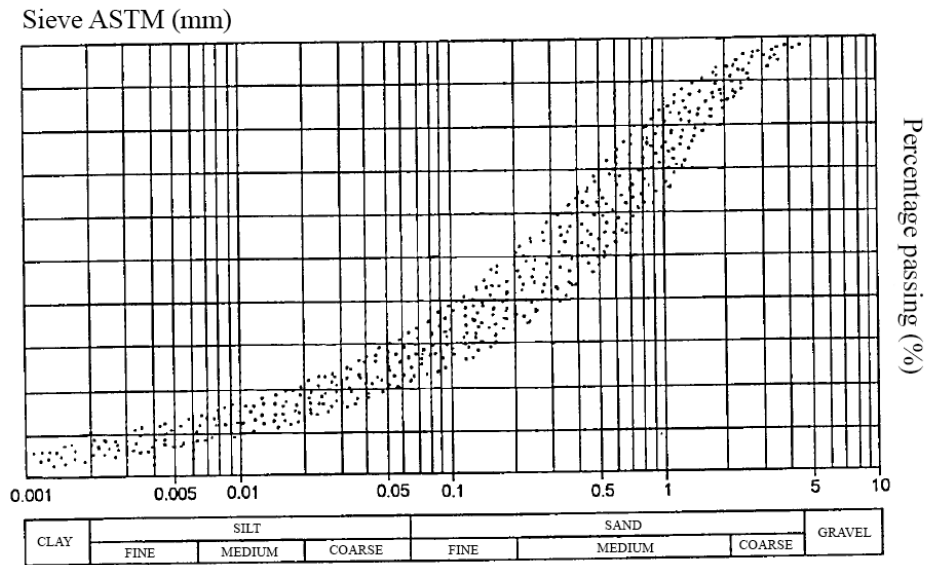
Figure 44. Granulometric distribution of Porto granite residual soil samples. Adapted from [105].
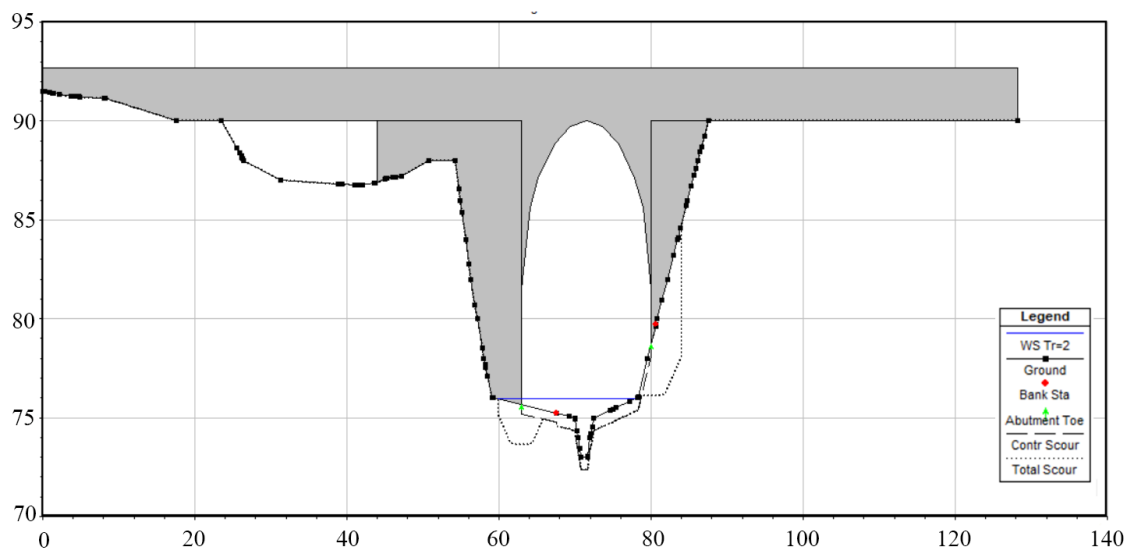
Figure 45. Graphic of contraction and total scour of the Leça bridge.

Several points can be highlighted from the results of the hydraulic model. For example, the transport of particles due to the average diameter and composition of the uppermost layer in the soil (alluvium) was accounted for the analysis by the live-bed flow condition equations. Consequently, it can be assumed that there is not only the phenomenon of sediment removal, but also that new material can be deposited in these layers. In the literature, this effect is discussed by several researchers, e.g., Arneson et al. [86]; however, its considering is beyond the scope of this study.

Moreover, according to calculations, the scour depths in the foundations are estimated to be between 1.6 and 3.5 meters. However, since the shallow layers that constitute the foundation are most likely to be removed and transported, it only has a depth of roughly three meters. Above this depth, it no longer makes sense to consider scour effects because of the bedrock profile. Although the bedrock is in a moderately weathered and fractured condition, its degradation process would be more meaningful in a long-term analysis rather than in an extreme event.

Table 12. Scour depth of the HEC-RAS.

Tr (years)	Left abutment		Channel contraction scour (m)	Right abutment	
	Local scour depth (m)	Total scour (m)		Local scour depth (m)	Total scour (m)
mean scenario					
2	1.52	2.17	0.72	1.82	2.54
5	1.58	2.34	0.83	2.16	2.99
10	1.68	2.42	0.84	2.22	3.06
25	1.79	2.55	0.90	2.33	3.23
50	1.80	2.57	0.90	2.35	3.25
100	1.87	2.66	0.95	2.41	3.36
90th percentile scenario					
2	1.56	2.32	0.83	2.17	3.00
5	1.56	2.33	0.92	2.36	3.28
10	1.57	2.34	0.92	2.37	3.29
25	1.63	2.43	0.96	2.43	3.39
50	1.63	2.44	0.97	2.43	3.40
100	1.67	2.49	0.99	2.47	3.46

These results can be used to define possible damage scenarios and analyze the behavior of the structure against these scour effects. In this way, quality control plans could be proposed to help in decision-making to mitigate damage and avoid consequences.

3.4 GEOTECHNICAL FAILURE ANALYSIS

3.4.1 BEARING CAPACITY OF FOUNDATIONS

After considering the types of failures in bridges that a flood could cause, it is intended to introduce the incidence of the soil in the multiple failure mechanisms already exposed. In this sense, soil failure occurs if the stress reaches the bearing capacity of the soil material. Therefore, establishing the bearing capacity of foundations is a necessary component of geotechnical engineering.

Statistics presented by Lin et al. [106] shown that bridges supported by reinforced concrete piles have a high failure rate, followed by spread footings. In this sense, several failure modes have been identified due to a combination of factors such as structural instability and inadequate soil support. Figure 46 shows the cases where vertical failure can occur due to loss of vertical bearing capacity.
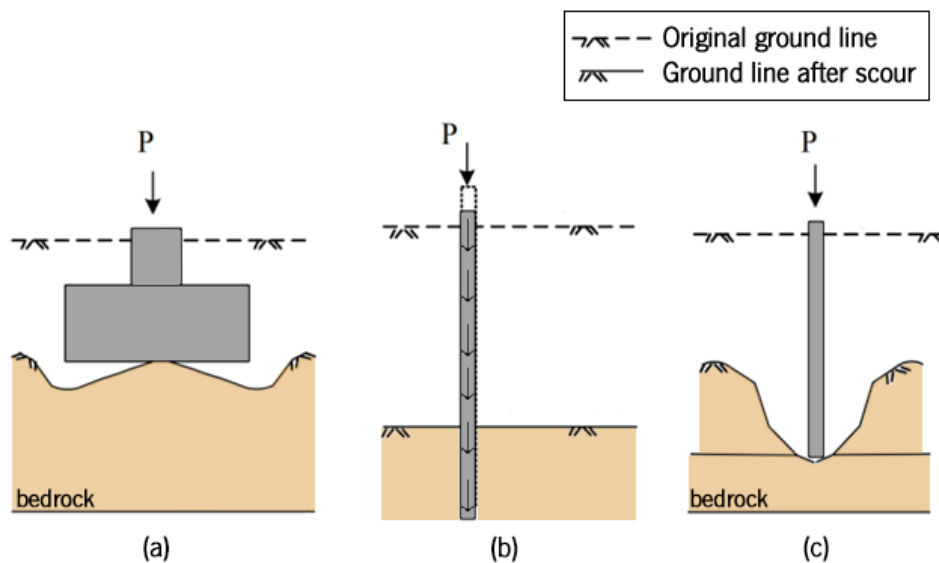
Figure 46 – Identified vertical failure in shallow and deep foundations. (a) Reduction of soil material in shallow foundations. (b) Reduction in capacity of friction piles. (c) Complete soil removal for end bearing piles. Adapted from [106]

Several methods to estimate the bearing capacity has been used over the years, as it is exposed by Alencar et al. [107], such as i) the limit equilibrium method [108], [109]; ii) the limit analysis method [110], [111]; iii) finite element models [112]–[114]; iv) artificial intelligence techniques [115]. Nevertheless, the fundamentals of the bearing capacity theory

were introduced by Terzaghi [108], which superposes the effects of the internal angle of friction, the cohesion, and the surcharge through bearing capacity factors (N_c, N_γ, and N_q). In this sense, the ultimate bearing capacity in foundations (considering uniform soil) can be estimated using the following equation:

$$q = \frac{Q}{BL} = cN_c + \gamma DN_q + \frac{1}{2}\gamma BN_\gamma \qquad (22)$$

Where Q is the applied vertical load, c is the apparent cohesion of soil, γ is the effective unit weight of soil, B and D are the foundation width and depth, respectively. However, this basic theory might be expected that it can be applied to any soil.

In reality, it does not work that way. In this sense, many authors have added their considerations which help to have accuracy when designing or analyzing modern foundations. Considerations such as the type of soil and the layers that compose it, its drained condition, the cohesion of the soil, the type of structural foundation used (shallow or deep) and its geometry, the direction and type of load received by the soil are some of the possible classifications that lead to consider different parameters. Nevertheless, addressing these methodologies and their difference exceeds the scope of this research.

Consequently, another important consideration for the proposed framework in this thesis is the type of failure related to the bearing capacity. In this sense, Terzaghi [108] defines the failure mechanism for uniform soil, which can be divided into three specific regions; i) the wedge zone is the region which is under the foundation, and it is characterized for receiving all the vertical loading from the structure while remaining intact; ii) the radial shear zone which is defined for a logarithmic spiral due to the generated rotations; iii) the passive zone formed as a linear shear zone and it is characterized for being pushed towards the top area. Figure 47 describes the geometry of the failure surface and the shape parameters considered.
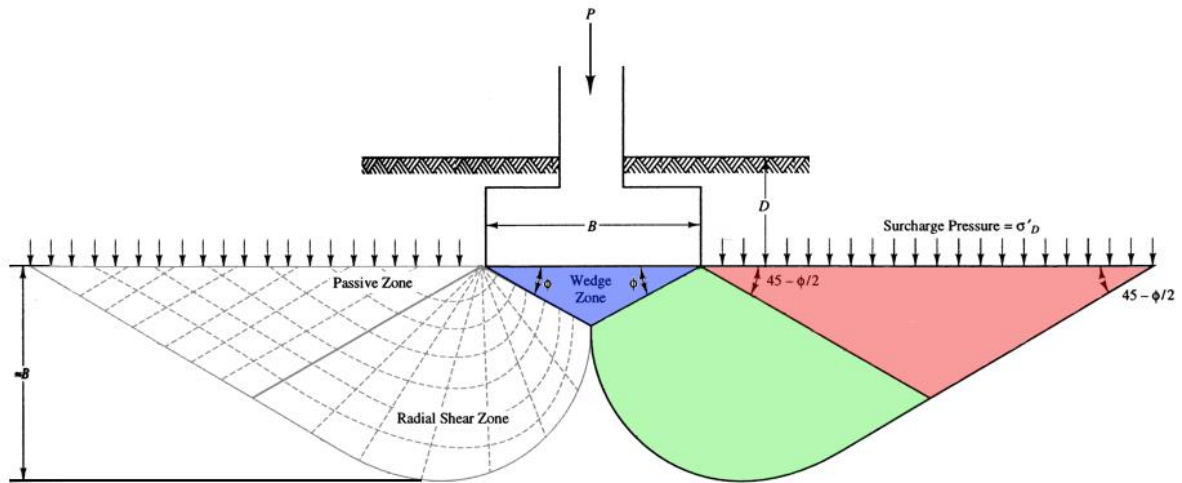
Figure 47 – Failure surface of a homogenous soil proposed by Terzaghi [108].

3.4.2 PRACTICAL CASE STUDY: URA E ZOGUT BRIDGE

A case study with a severe scour problem in its foundations is assessed to test the methodology. The bridge called "Ura e Zogut" is located on the Mati River in northern Albania (see Figure 48).

Figure 48 – Ura e Zogut bridge

In 1926 the company Mazorana & Co. started the construction of the existing bridge, which has 16 spans, of which ten are simply supported RC beams, and the rest are RC tied arch. The first ten spans are in the valley where river water is rarely riches, and the last six are in the riverbed. The simply supported RC beams have two different span lengths, six of them are 15.0 m long, and four of them are 19.2 m long, while the six tied-arch spans were identical

with a span length of 54.0 m and arch length of 53.2 m that makes the bridge entire length of 490.8 m. All the arched spans of the bridge are identical RC elements. For this reason, a single-span drawing of a tied arch is shown in Figure 49.

The Bridge system is a combination of a trustless arch with tie beams), supported by four bearings. Figure 49 identifies and locates the main structural elements of the bridge: (1) arch, (2) hangers, (3) tie beam, (4) pier, (5) pile cap/foundation, (6) pile group, (7) steel sheet pile support, (8) natural ground at construction time, (9) brace beams, (10) slab, (11) slab beams. The arch has a variable width cross-section of 0.50 m and height varying from 1.15 m to 1.34 m, longitudinal reinforced by 10Ø28 plain steel bars in the upper zone and 5Ø28 plain steel bars in the lower zone. The hangers have different clear lengths starting from 1.46 m to 9.30 m with a cross-section of 0.40x0.20 m longitudinal reinforced by 4Ø26 plain steel bars. The tie beams have a cross-section of 0.34x0.60 m, longitudinal reinforced by 14Ø40 plain steel bars. Two arches of a single span are connected by K-shaped top bracings every 3.325 m.

The main bracings have a cross-section of 0.25x0.50 m and diagonal bracings of a cross-section of 0.20x0.20 m. The slab is 0.14 m thick with four longitudinal bracing beams of cross-section 0.20x0.45 m settled on floor beams of cross-section 0.30x0.50 m. All the piers/foundations are identical reinforced concrete elements, as shown in Figure 49. The pier is 6.9 m high and has a variable rounded corner cross-section with bottom dimensions of 1.65x9.82 m and top dimensions of 1.35x9.52 m.

The foundation is 10.0 m deep, from which the first 5.7 m are a rounded corner cross-section with dimensions of 2.53x10.14 m, and the last 4.3 m are twenty-two piles of 0.35 m in diameter. The total length of the piles (including the part embedded in the pier) is 7.0 m. According to the foundation geotechnical profile, it can be stated that despite the depth, there is no bed of firm rock. Therefore, the structure is supported by sandy gravel of variable density without cohesion, making it vulnerable to particles dragging over time. Figure 50 shows the soil profile of the foundation and its properties.
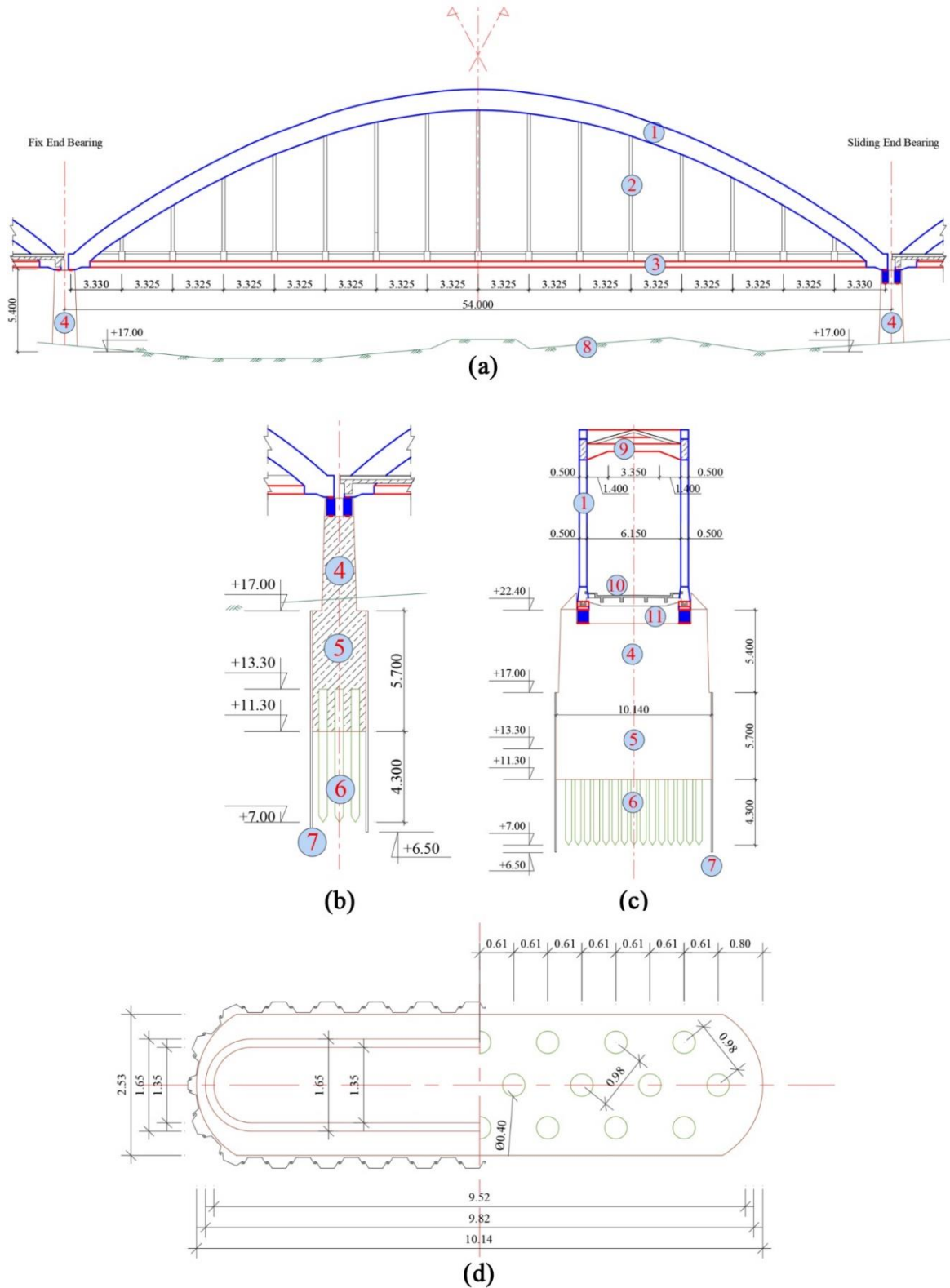
Figure 49 – Ura e Zogut bridge blueprints. (a) Single span longitudinal view. (b) Foundation sectional view. (c) Single span sectional view. (d) Foundation plan view
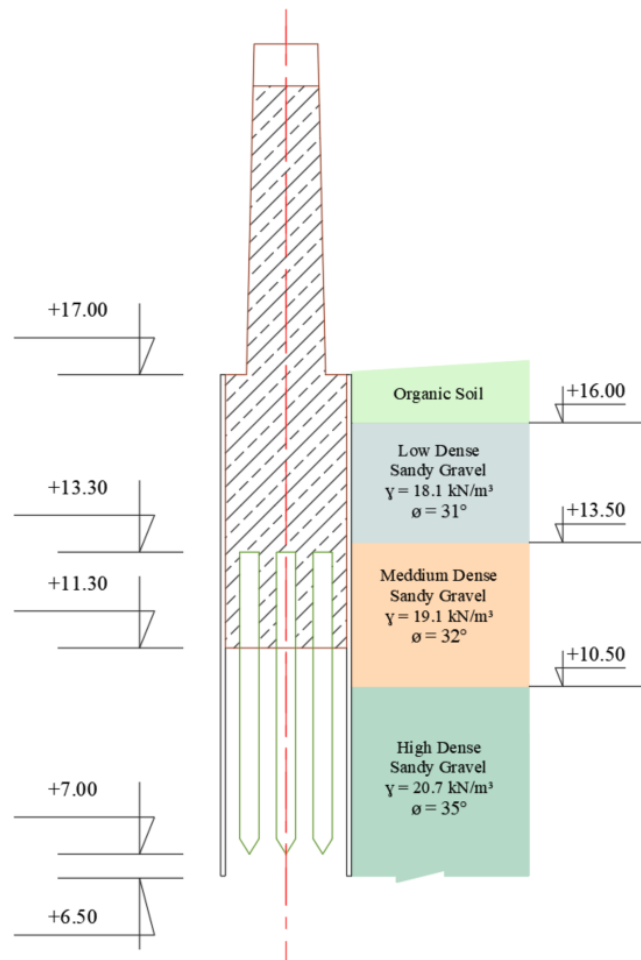
Figure 50 – Soil profile of the Ura e Zogut bridge

Currently, the bridge is closed, and the only forces acting on it are the self-weight of the structural elements. As two consecutive spans are symmetric respecting the pier axis, the foundation transmits to the ground the weight of the pier, the foundation, and the weight of two semi-arches. So, the calculating acting force on a single pier/foundation is shown in Table 13.

Therefore, the foundation of the Ura e Zogut bridge is analyzed by computing the bearing capacity of the soil. Due to its scour problems (see Figure 51), the numerical model of the foundation is divided into three states: i) As built; ii) critical equilibrium point; iii) current scour state.

Figure 51 – Scour problems in the foundation of the Ura e Zogut bridge

Table 13. Forces acting on a single pier/foundation.

	Element No.	Element	RC Volume [m^3]	RC Unit Weight [kN/m^3]	Weight [kN]
Foundation	4	Pier	96.84	24.00	2,324.20
	5	Pile Cap / Deep Foundation	164.75	24.00	3,954.07
	6	Pile Group	11.88	24.00	285.30
					6,563.57
Superstructure	1	Arch	72.55	24.00	1,741.20
	2	Hangers	17.53	24.00	420.72
	3	Tie beam	29.13	24.00	699.12
	9	Brace Beams	15.99	24.00	383.76
	10	Slab	63.72	24.00	1,529.28
	11	Transversal Beams	13.28	24.00	318.60
					5,092.68

However, a structural failure cannot be calculated due to the uncertainty associated with the soil properties, the foundation materials, and the bridge loading. Thus, the software Geo5 – foundation packages (pile group) have been used. This geotechnical tool analyzes a pile raft

foundation with a rigid pile cap by applying the analytical solution, computing the vertical bearing capacity considering a normal loading force [116]. Table 14 summarizes the methodology and equations performed by the software.

Table 14. Analytical solution methodology.

Analysis type	Analytical solution	
Type of soil	Cohesionless soil	The vertical bearing capacity is calculated by: $$R_g = \sum R_c = nR_c\eta_g$$ Where R_c is vertical bearing capacity of an isolated pile, and η_g is the pile group efficiency, and n is the number of piles in a group.
Analysis of drained conditions	NAVFAC DM 7.2 [117]	Calculation of vertical pile resistance is performed according to the publication [117]
The efficiency of pile group	La Barré (CSN 73 1002) [118], [119]	$$\eta_g = 1 - \psi\left[\frac{(n_x - 1)n_y + (n_y - 1)n_x}{90n_xn_y}\right]$$ $$\psi = arctg\frac{d}{s}$$ Where n_x is the number of piles in the x-direction, n_y is the number of piles in the y-direction, ψ is the angle having tangent expressed in degrees, s is the axial spacing of piles, and d is the diameter of piles.
Verification methodology	Safety factors (ASD)	The verification analysis for a pile group in compression follows the expression: $$\frac{R_g}{V_d + W_p} > SF_{cp}$$ Where V_d is the maximum vertical force (including the pile cap self-weight), W_p is the self-weight of piles, and SF_{cp} is the safety factor for a pile group in compression.

Thus, the foundation geometry (see Figure 52), the material and the soil profile were modelled considering all collected information from the case study. Figure 53 represents the numerical model of the foundation in the three defined states.
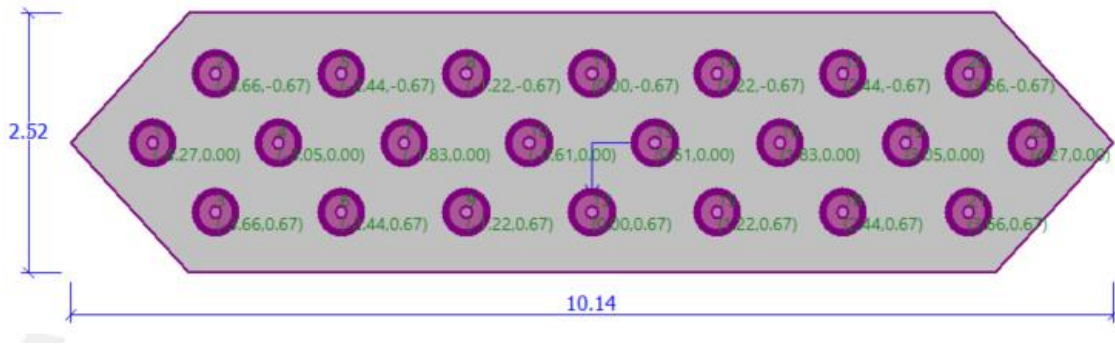
Figure 52 – Pile cap equivalent cross-section

(a)

(b)

(c)
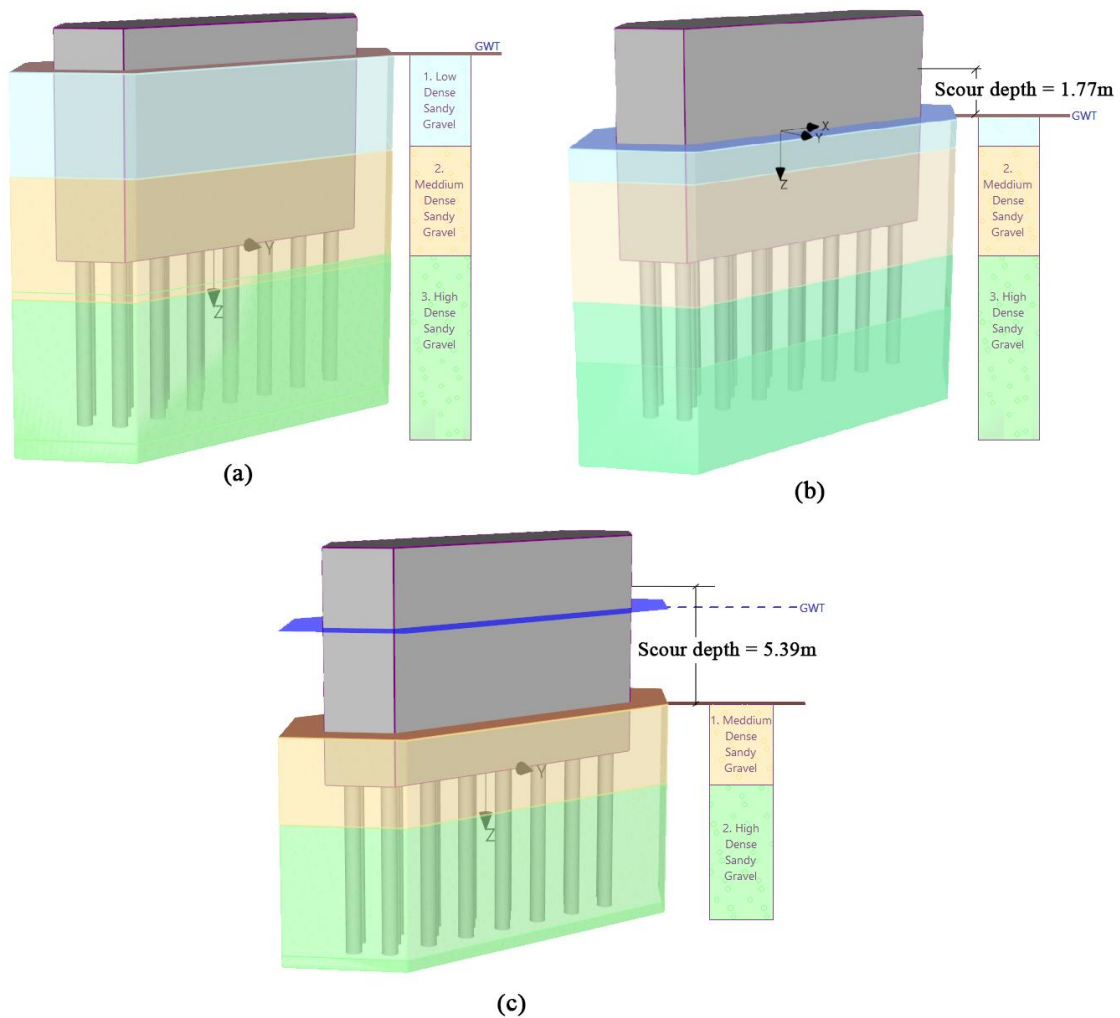
Figure 53 – Foundation numerical model. (a) As-build state. (b) Critical equilibrium point. (c) Current scour state.

The results of the analysis of the vertical bearing capacity of a pile group in cohesionless soil and drained conditions relative to the method used and the pile group efficiency η_g are presented in Table 15.

Table 15. Analysis of bearing capacity of the pile group in cohesionless soil.

	Original state	Critical state	Scour state
Pile skin bearing capacity (R_s) $[kN]$	246.12	193.11	138.60
Pile base bearing capacity (R_b) $[kN]$	593.13	488.91	389.11
Vertical bearing capacity of single pile (R_c) $[kN]$	839.26	682.03	527.71
Efficiency of pile group (η_g)	0.70	0.70	0.70
Vertical bearing capacity of pile group (R_g) $[kN]$	12924.56	10503.24	8126.78
Percentage of capacity loss compared to the original state	0%	18.73%	37.12%
Maximum vertical force (V_d) $[kN]$	10515.59	10515.59	10515.59
Safety factor $(SF_{cp}) > 1.00$	1.23	1.00	0.77
Vertical bearing capacity of pile group is:	Satisfactory	Not satisfactory	Not satisfactory

The results show that the calculated vertical bearing capacity of a pile group R_g in cohesionless soil is reduced considering the efficiency of the pile group (η_g) because individual piles statically affect each other. In general, individual piles in a group affect each other more when the spacing on centers is decreased. Therefore, the results may vary if the η_g varies depending on the methodology used.

3.5 FINAL REMARKS

In this chapter, the most common methods for describing the interaction between floods and bridges were described, with the aim of being a link between hazard analysis and structural analysis. Therefore, the failure modes that can be expected in the structure and in the soil were described. In addition, analyzes of practical cases were included to complement the theoretical methods. First, the quantification of scour in a superficial foundation. Second, the geotechnical analysis of a bridge that is in a state of severe scour.

The first case was based on the hydraulic models carried out in the previous chapter for the Leça basin. Thus, one of the bridges over the main river was analyzed. From the results it is

possible to derive, although conservatively, possible damage scenarios for risk analysis and structural reliability.

In the second case, according to an analysis of the current load-bearing capacity (without considering a probabilistic analysis), the structure is expected to be highly vulnerable. Therefore, mitigation measures have to be considered before a possible collapse due to the increasing undermining of the foundations.

Finally, this chapter provided the necessary bases for the construction of Workstream 2, which allows for an analysis of soil-structure-flood interactions and the creation of damage scenarios for the implementation of subsequent workstreams.
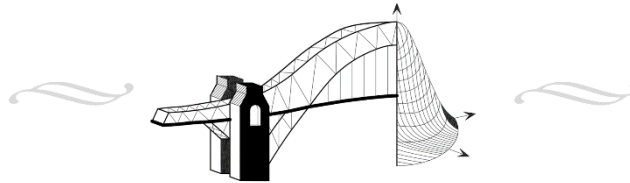
ROBUSTNESS METHODOLOGY

4.1 INTRODUCTION

The Eurocode [120] defines robustness as: "*the ability of a structure to withstand events like fire, explosions, impact or the consequences of human error, without being damaged to an extent disproportionate to the original cause*". Robustness is important for maintaining the ability of the structural system to fulfill its function during any event, such as an accidental loading or due to the consequences of human errors, addressing aspects such as: i) life safety; ii) property and environment protection; iii) protection of operations [121]. Robustness indicators are then used to assess an extreme event's most critical/vulnerable structural typologies.

The first approaches proposed are to assess structural safety by evaluating individual structural elements rather than assessing the global structural system performance. However, the failure of a structural element does not always lead to structural collapse. Consequently, researchers started to consider system-level safety assessments of structures such as buildings and bridges [122].

Although design codes have structural robustness approaches, recent research considers the robustness quantification and the determination of reference values for standardization. Table 16 presents the current methodologies for robustness assessment following three branches according to the approaches presented by the respective authors.

Table 16. Robustness assessment methodologies.

Deterministic methodology	Probabilistic methodology
Frangopol and Curley (1987) [123]	Frangopol and Curley (1987) [123]
Biondini and Restelli (2008) [124]	Lind (1995) [126]
Starossek and Haberland (2008) [125]	Ghosn and Moses (1998) [127]

4.1.1 DETERMINISTIC METHODOLOGY

Redundancy and robustness definitions were in the past considered equivalents. Nevertheless, an accurate distinction between both concepts has not yet been established. In this context, Frangopol and Curley [123] proposed a deterministic redundancy indicator expressed by equation (23), relating the resistant capacity of the structure without damage (L_{intact}) and the resistance capacity of the structure affected by damage ($L_{damaged}$).

$$L_R = \frac{L_{intact}}{L_{intact} - L_{damaged}} \qquad (23)$$

Where L_R is the redundancy factor of the structure. This value reaches its minimum when the structure has no damage, and it tends to infinity when ($L_{damaged}$) is equivalent to (L_{intact}). Regarding the estimation of the resistant capacities, the methodology is based on resistance parameters completely deterministic.

4.1.2 PROBABILISTIC METHODOLOGY

The methodology considers the uncertainties associated with the limited state of the structure, which is represented by the boundary between the structure's strength and load model. Therefore, considering the mean value and the standard deviation of the representative variables is essential for quantifying structural robustness. To include the uncertainties associated with structural strength and structural loading in assessing structural robustness, Frangopol and Curley [123] proposed a robustness indicator that depends on the structure reliability index and is defined by equation (24).

$$\beta_R = \frac{\beta_{intact}}{\beta_{intact} - \beta_{damaged}} \qquad (24)$$

Where β_{intact} is the virgin reliability index and, β_{damaged} is the reliability index considering the damage. The probabilistic redundant index β_R varies within the range between zero and ∞ with $\beta_R = 0$ indicating a "completely" damaged structure (i.e., $\beta_{\text{damaged}} = -\infty$) and $\beta_R = \infty$ indicating an intact structure (i.e., $\beta_{\text{damaged}} = \beta_{\text{intact}}$).

4.1.3 PROBABILITY OF FAILURE

The probabilistic methodology for the robustness assessment depends on the reliability index estimation as an indicator of the probability of failure of the structure (P_f). Therefore, this probability can be associated with an unwanted structural performance which the limit state function can represent:

$$P_f = P(R - S < 0) \tag{25}$$

Where R and S represent the probabilistic distribution of the resistance and solicitation load, respectively. These two random variables with different dimensions are associated with a bivariate distribution function $f_x(x)$ which can be graphically represented (see Figure 54) and the limit state can be defined when $R = S$. Moreover, the limit state function delimits the safe area (when $R - S > 0$) from the failure area (when $R - S < 0$).
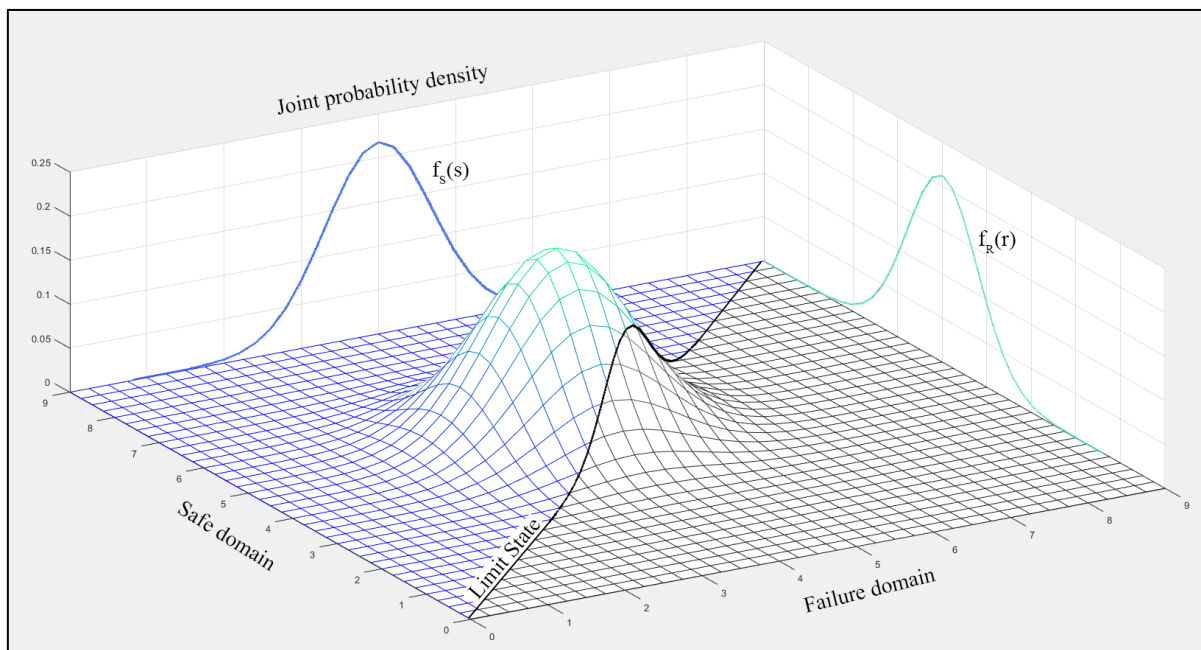
Figure 54. 3D representation of the PDF $f_x(x)$

In mathematical terms, to compute the system response of interest, it is necessary to apply equation (26), an n-fold integral using an n-vector (x) of random input variables.

$$P_f = P(R - S \leq 0) = \int_{R-S \leq 0} f_x(x) \, \mathrm{d}x \qquad (26)$$

In normal terms, the integral cannot be solved analytically. Therefore, several authors in past years developed probabilistic reliability methodologies to calculate the joint probability density function $f_x(x)$ [128]–[130], and can be classified into three different groups: i) gradient-based methods; ii) sampling-based methods; iii) metamodeling-based methods.

4.1.3.1 Gradient based methodology

This approach, also known as approximate methods, has two exponents primarily used in this field, the first and second-order reliability methods (FORM and SORM). These approaches calculate the probability of failure of a system by transforming the original space (failure surface) into the standard normal space (u). In this sense, the n-vector (x) of random input variables can be mapped by applying several approaches such as the Nataf transformation [131], Hasofer-Lind [132], the Rackwitz-Fiessler transformation [133], the Rosenblatt transformation [131], and among others. Then, the Taylor series expansion is used to approximate the integration boundary $G(u) = 0$, which now can be treated as an optimization problem, which is necessary to determine the point of mayor probability density or "design point".
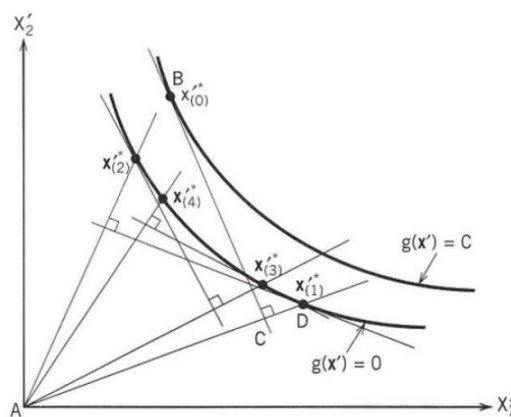
Figure 55. Graphic representation of the FORM Iterative process [134]

Consequently, the difference between FORM and SORM is determined by the Taylor series expansion order, where the first order used in FORM is a linear approximation and the second order used in SORM is a quadratic approximation. Therefore, SORM offers improved results by considering the relative non-linearity of the limit state function.

4.1.3.2 Sampling-based methodology

This approach comprises computational algorithms based on repeated random sampling as a simulation methodology. Nevertheless, all simulation techniques are based on Monte Carlo simulation (MCS).

The MCS is widely used in this field to calculate integrals and event probabilities. For example, to estimate the P_f exposed in equation (26) by rewriting the integral employing an indicator function (see equation (27)), in which if $g(x) \leq 0$, the indicator function is equal to one, and zero if the inequality is not satisfied.

$$P_f = \frac{1}{N} \sum_{j=1}^{N} I[g(x) \leq 0] \qquad (27)$$

However, the basic or crude MCS has an inefficient convergence rate and high computational impact. Therefore, more advanced MCS schemes reduce such limitations by applying variance reduction-based technics capable of lessening the required sampling size, such as Latin hypercube sampling [135], subset simulation [136], importance sampling along with its variants [137], [138], line sampling [139], [140], directional sampling [141]. Nevertheless, according to several authors [142], [143], even with the improvement of the variance reduction technic, if the problem presents low probabilities of failure, a large number of variables, and dependencies among them, the computational requirements are still expensive time-consuming.

4.1.3.3 Metamodeling-based methodology

As was exposed in the other methodologies, the difficulty and the amount of resources required to solve the equation (26) is the principal issue. Nevertheless, the general idea of replacing or transforming the function $f_x(x)$ to get easier to solve is still applied in this methodology. In this sense, mathematical algorithms called metamodels or surrogate models

are introduced to adjust an approximate function that is easier and faster to evaluate. Several kinds of metamodels may be found in the literature to be used in reliability analysis problems, such as the polynomial response surfaces [142], the polynomial chaos expansions [144], artificial neural networks [145], support vector machines [146], and kriging [147]. According to Guimarães et al. [143], the metamodels follow a general stepping which is the definition of the purpose and goal of the model, the obtention of data, fitting and validation of the model and updating until convergence.

Depending on the approach and complexity of a problem, structural reliability procedures vary for calculating failure probability. For instance, stochastic methods simplify several aspects of the structural behavior and omit uncertainties in the limit state function. On the other hand, complex methodologies consider a probabilistic non-linear structural assessment taking into account the most relevant uncertainties of the problem. Nevertheless, the introduction of surrogate modelling techniques into many areas of engineering determines the possibility of replacing traditional models by obtaining the desired outcomes and decreasing the investment in computational terms (i.e., time and effort resources). As a complementary approach, a fragility analysis is broadly used due to the capacity to represent the probability of exceeding a given limit state for an assumed intensity of a hazard.

Nevertheless, published literature on fragility functions for bridges exposed to flood hazards is far more scarce than other hazards such as earthquakes [148]. The combined effect of flood-induced scour and bridge seismic fragility has been assessed by some authors like Banerjee et al. [149], Dong et al. [150], and Yilmaz et al. [151]. However, some studies have developed flood-related fragility curves for concrete bridges with additional demands such as hydraulic forces, hydrodynamic pressure due to debris accumulation and deterioration effects owing to corrosion [152]–[155]. Recently, some research contributions have introduced surrogate modelling techniques into the probabilistic framework for quantifying the failure probability of bridges under flood hazards to overcome this issue [156], [157]. It is noteworthy to note, however, that research on the fragility modelling of bridges subjected to the combined effects of flood and scour by means of surrogate modelling is still limited.

4.1.4 ROBUSTNESS INDICATOR

The introduction to this chapter briefly defines the concept of robustness and some proposed approaches for implementing this concept in structural management methodology. However, it is not possible to determine which methodology is better or not, as there are a variety of interpretations of what should define robustness and what variables should be considered to quantify this indicator. In addition, each methodology has its advantages and disadvantages.

In this sense, to align with the proposed framework in this research for the safety assessment. It is considered to use the robustness approach proposed by Cavaco et al. [158], which first studied the existing methods and their differences/similarities. As a result, they were able to develop a framework based on the work of Biondini and Restelli [124] and Starossek and Haberland [159], considering the positive aspects of each approach. In this way, it was defined equation (28), in which the robustness indicator ($I_{R,D}$) is calculated as the area under the normalized structural performance curve $f(D)$ as a function of the normalized damage (D).

$$I_{R,D} = \int_{D=0}^{D=1} f(D)dD \qquad (28)$$

According to Cavaco et al. [158], the complexity of this methodology is given by the performance indicator used to define $f(D)$. Consequently, the reliability index (β) will be considered for this research. However, due to the difficulty of this indicator to consider the general damage spectrum, a strategy to define $f(D)$ can be proposed.

Therefore, the reliability index is calculated for several magnitudes of the evaluated damage. Subsequently, these values are adjusted to a function defined by a metamodel, making it easier to evaluate the definite integral in equation (28).

Regarding the obtained robustness indicator, it is necessary to highlight that this procedure does not consider the causes of the damage or the probability of occurrence. Otherwise, this parameter helps to represent the sensibility of the structure against the studied damage, allowing direct comparisons with different structure typologies and defining which one is more robust. Therefore, Cavaco et al. [158] defined a graphical representation of the area

down the curve expecting a minimum or maximum value of the robustness indicator shown in Figure 56.
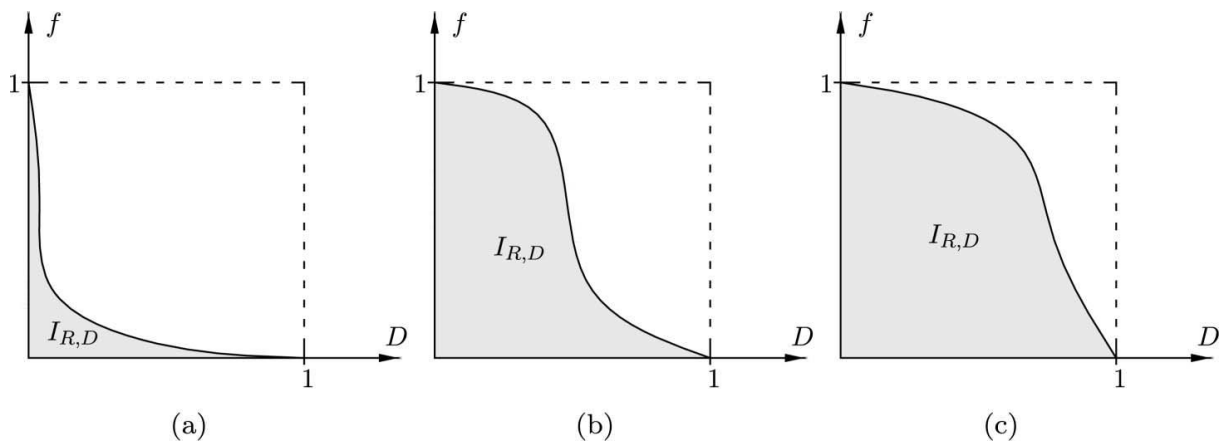
Figure 56. Graphical representation of the robustness indicator (a) minimum. (b) Intermediate. (c) maximum. defined by Cavaco et al. [158]

4.2 PRACTICAL CASE STUDIES APPLICATION

The first case study is a reinforced concrete arch bridge over the Cró River in the Guarda district, Portugal (Bridge A) (Figure 57). The bridge carries the national road EN324 and has two lanes (2.53 m and 2.51 m each), two carriageway edges (0.45 m and 0.51 m each) and two walkways of 1 m. The case study was built in 1940 and repaired in 2010. The data used for the numerical analysis are based on the design project and two inspection reports from 2007 and 2015 provided by IP.

Figure 57. Location plan. (a) Bridge A, Cró river, Guarda, Portugal.

Bridge A is an open-spandrel deck arch bridge with a total length of 24 m. Its geometrical data are shown in Figure 58. The design project indicated that a two-hinged arch supports the deck. The following nondestructive testing results were available for this case study: Concrete strength (see Table 17).
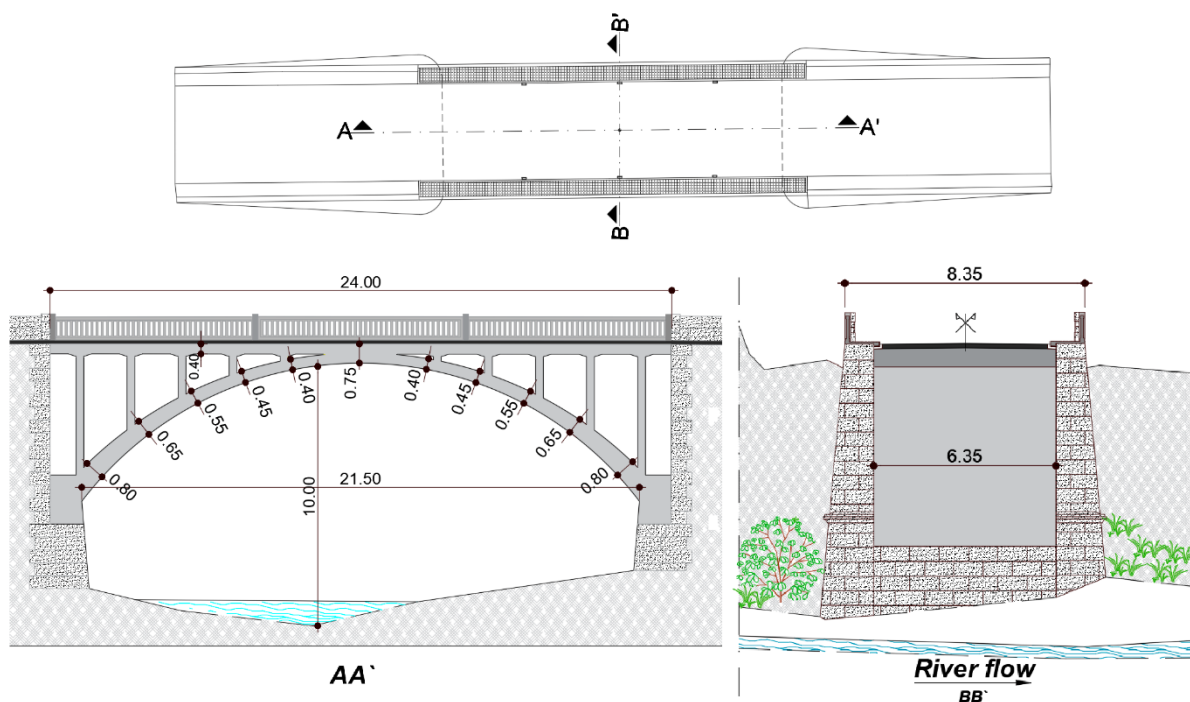
Figure 58. Bridge A blueprints.

Table 17. Compressive strength results from NDTs of Bridge A.

Spec. No	f_c [MPa]	$f_{c,avg}$ [MPa]
1	38.30	
2	43.90	
3	50.00	43.14
4	42.50	
5	41.00	

The second case study is a reinforced concrete arch bridge located in North Macedonia (Bridge B), shown in Figure 59. The bridge carries the national road M-1 (E-75) on the Katlanovo-Veles and has a total width of 9.20 m (2x3.80 m + 2x0.60 m + 2x0.20 m). It was built in 1963 and strengthened in 2007. The construction documents of the bridge were not available; therefore, the construction drawings were used. A fixed-end slab-type arch shapes bridge B

with a span of 54 m, whose approach structures consist of three spans on one side and five spans on the other side of approximately 6 m each, resulting in a bridge with a total length of 102.65 m (see Figure 60). The following test results were available for this case study: Concrete compressive strength from the extracted concrete cores and tensile strength from "pull-off" tests (see Table 18).
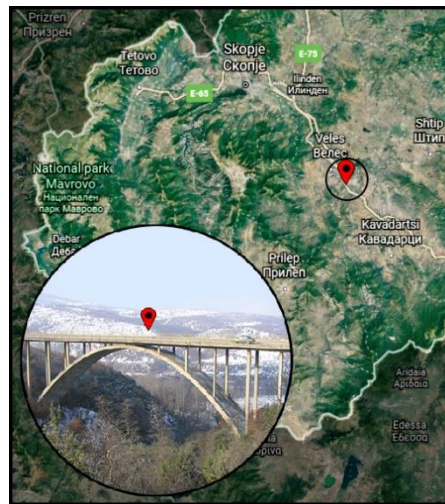
Figure 59. Location plan. Bridge B, Katlanovo-Veles, North Macedonia.
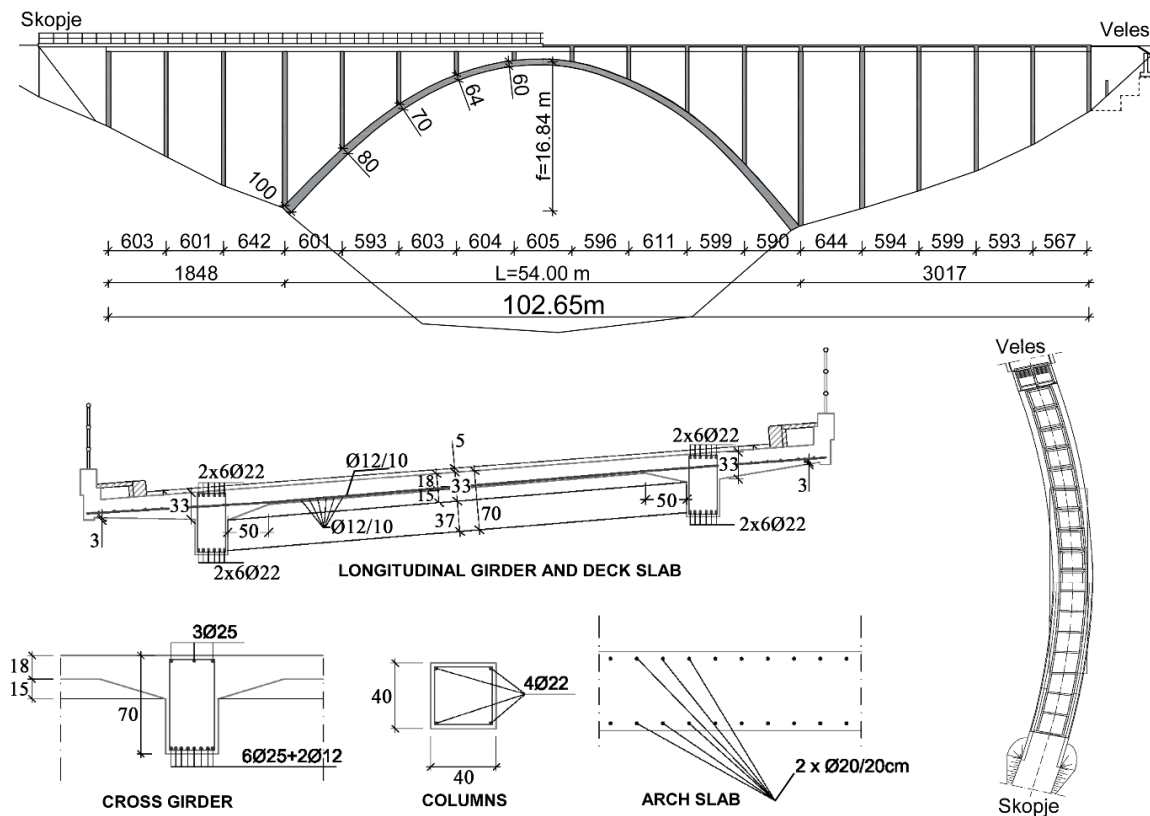
Figure 60. Bridge B blueprints.

Table 18. Compressive and tensile strength results from NDTs of bridge B.

Spec. No	f_c [MPa]	$f_{c,avg}$ [MPa]	Spec. No	f_t [MPa]	$f_{t,avg}$ [MPa]
1	51.93		1	2.5	
2	31.05		2	3.1	
3	50.13	40.96			2.4
4	40.89		3	1.6	
5	30.79				

4.2.1 VULNERABLE ZONES IDENTIFICATION

Following the WG3 report [68] of the COST action TU1406 and the best practices of structural analysis, the structural systems of the case studies were defined (the current static condition and its structural elements). Then, the vulnerable zones were carefully selected. These vulnerable zones are segments or elements of a bridge where damage affects structural safety and serviceability. Moreover, such zones can be associated with different failure modes [68]. Therefore, it is not necessary to say that they depend on the case study.

Since both bridges have similar structural systems, common vulnerable zones were defined for the load-bearing elements, namely: high moment regions HMR (critical sections of the arch and deck), high compression regions HCR (supports of the arch and piers/walls), and high deflection regions HDR (crown of the arch and middle span of the deck). The vulnerable zones of the case studies are shown in Figure 61. Later, these zones were carefully inspected, and the deficiencies identified in these zones were considered for further analysis.

(a)   (b)
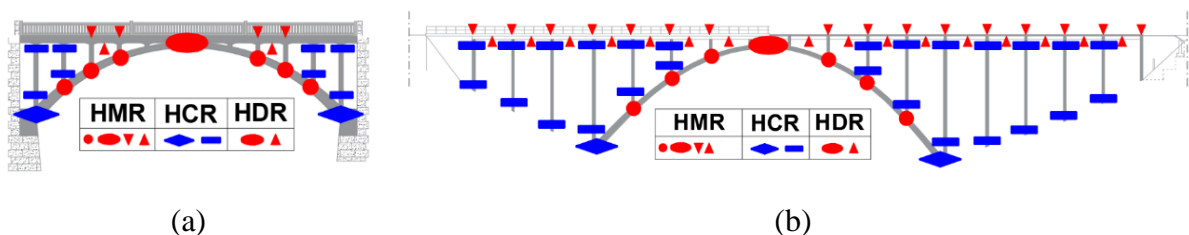
Figure 61 - Vulnerable zones. (a) Bridge A. (b) Bridge B.

4.2.2 IDENTIFICATION OF ONGOING DAMAGE PROCESSES

Information on the damage processes is essential for predicting the actual performance of the bridge (at the time of inspection) and for planning maintenance and eventual rehabilitation

work. The two bridges inspected were built some time ago, so the deterioration processes have already been initiated in the past. Figure 62 and Figure 63 show the most critical deficiencies identified during the performed inspections in the previously defined vulnerable zones.
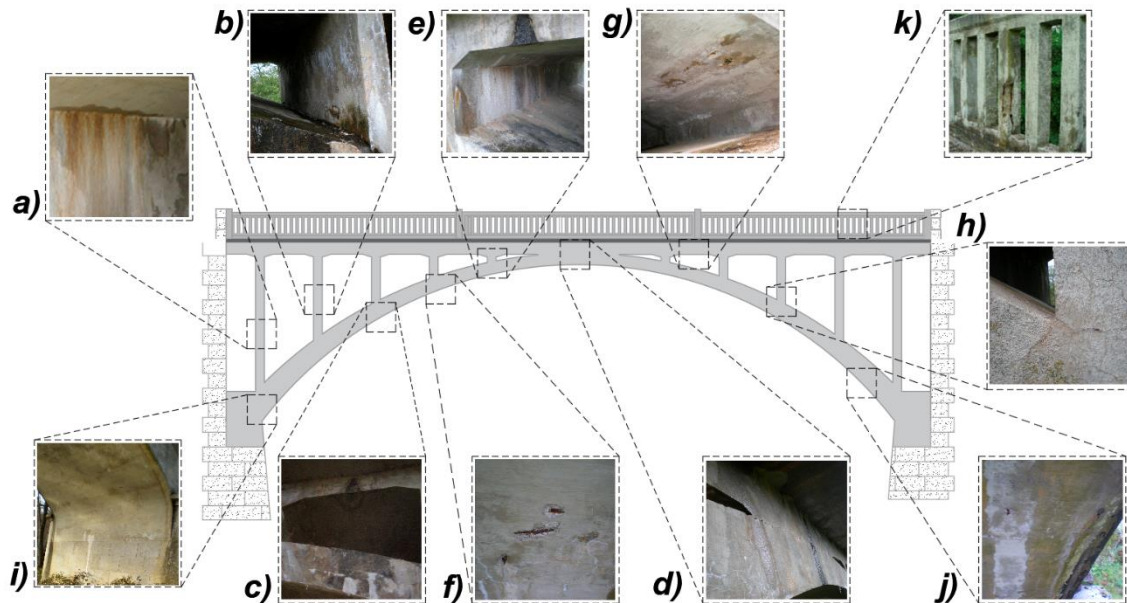
Figure 62 - Main observations in the vulnerable zones from the visual inspection (bridge A)
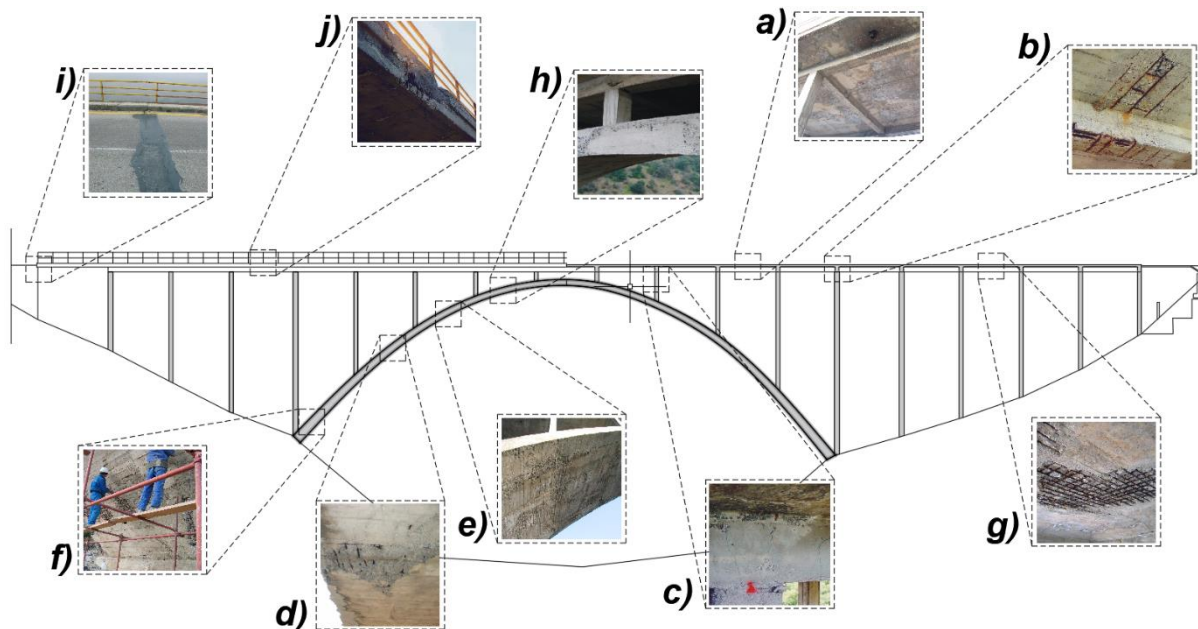
Figure 63 - Main observations in the vulnerable zones from the visual inspection (bridge B).

In the bridge A (Figure 62), the following defects were observed: concrete spalling (f,g,k), hairline cracks (b,h), calcium leaching (b,f,j), brown spots (a,g,j), direct wetting of concrete (b,c,e), steel corrosion (f,g) and drainage inadequacy (c,e).

A considerable number of defects were also observed in the bridge B (Figure 63): construction error (d, h), inappropriate water drainage (a), hefty damages due to advanced corrosion of concrete and steel reinforcement of the deck slab (b, g) and the longitudinal girders (b), expressed process of carbonization on entire deck slab (a), insufficient or spalled concrete cover (b, d, f, g), cracks at the connection with the column (c), improper expansion joint (i), visible reinforcement due to missing parts of concrete on the railing parapets (j) and inappropriate concreting and segregation (d, f, h).

To estimate the safety level (i.e., reliability index) at the time of inspection, it is necessary to identify the governing damage processes based on the observed damage in order to numerically investigate their influence on structural safety through damage scenarios. Therefore, depending on the extent and severity of the damages, the following scenarios were considered, considering the provided mean values and CoVs:

• Scenario one: Reinforcement cross-section reduction due to corrosion-global reduction of a mean value of 20% (bridge A) and 30% (bridge B) with a CoV 5%.

• Scenario two: Concrete degradation-global reduction of young's modulus mean value of 20% with a CoV of 5%.

• Scenario three: Combination of scenario one and scenario two.

According to the information gathered, a degradation of the young modulus was observed. Therefore, scenario two was established according to such information. Concerning scenario one, an estimation of the corrosion's advancement by removing the steel rust (steel oxides) was attempted. In addition, the carbonation depth information was also considered.

The estimations provided in the scenarios are a rough appraisal of what was observed and inferred. Nevertheless, a detailed investigation should be conducted using more sophisticated techniques to assess corrosion progress, such as deterioration models and the evaluation of

attachment loss between the concrete element and the reinforcement. Elaborated work on the topic can be found in [160], [161].

4.2.3 FEM NON-LINEAR ANALYSIS

Efficient techniques for non-linear numerical analysis and probabilistic methods coupled with finite element models (FEM) were implemented to set an advanced tool for assessing the actual performance of the bridges with some accuracy. Therefore, the structural safety levels of the case studies were assessed for the damage-free and damage included scenarios. Accordingly, the virgin reliability index was at first estimated for both bridges. Such safety level corresponds to the performance of the bridges at the time of their commissioning. Here, design and construction errors are disregarded.

In order to compute the reliability index of the case studies, the load-bearing capacities of the structures must be known. For that purpose, non-linear analysis considering the non-linear elasticity of the concrete, according to European Committee for Standardization [162] stress-strain curve, was performed in DIANA FEA software. Two-dimensional (2D) FEM using plane stress finite elements for concrete (a four-node quadrilateral isoperimetric element shown in Figure 64) and embedded bonded truss elements for longitudinal reinforcement. Only bending reinforcements were considered [163] to build the global numerical model (see Figure 65).
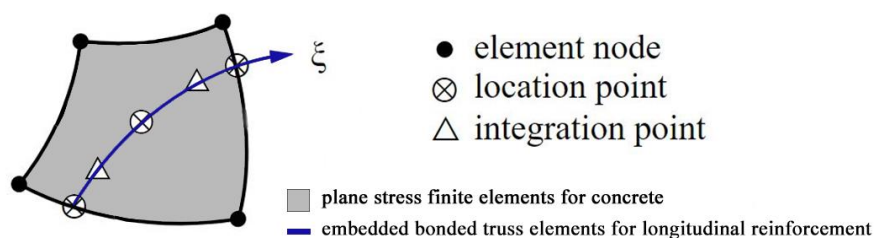
Figure 64 – Plane stress element with its embedded reinforcement

The concrete non-linear behavior is simulated with a total strain rotating crack model, while the reinforcement steel is modeled using an elastic-plastic stress-strain curve, using as an input the mechanical properties obtained through NDTs (See Table 17 & Table 18). In addition, three degrees of freedom per node were considered to reduce the computational cost for the non-linear analysis.

The load-bearing capacity of the systems was verified only for permanent (self-weight and additional dead loads) and live loads, which means this analysis did not include other loads usually considered at the designing stage (earthquake, temperature, creep and shrinkage, wind). Therefore, traffic load model 1 (LM1) of the European Committee for Standardization [164] was considered. The governing live load case considered for assessing the bridges was an equivalent uniformly distributed load of 38 kN/m and a two-axle load of 401 kN spaced in 1.2 m, applied to the deck to a section located at 1/4th of the arch span [165], [166] (Figure 65).

(a)

(b)
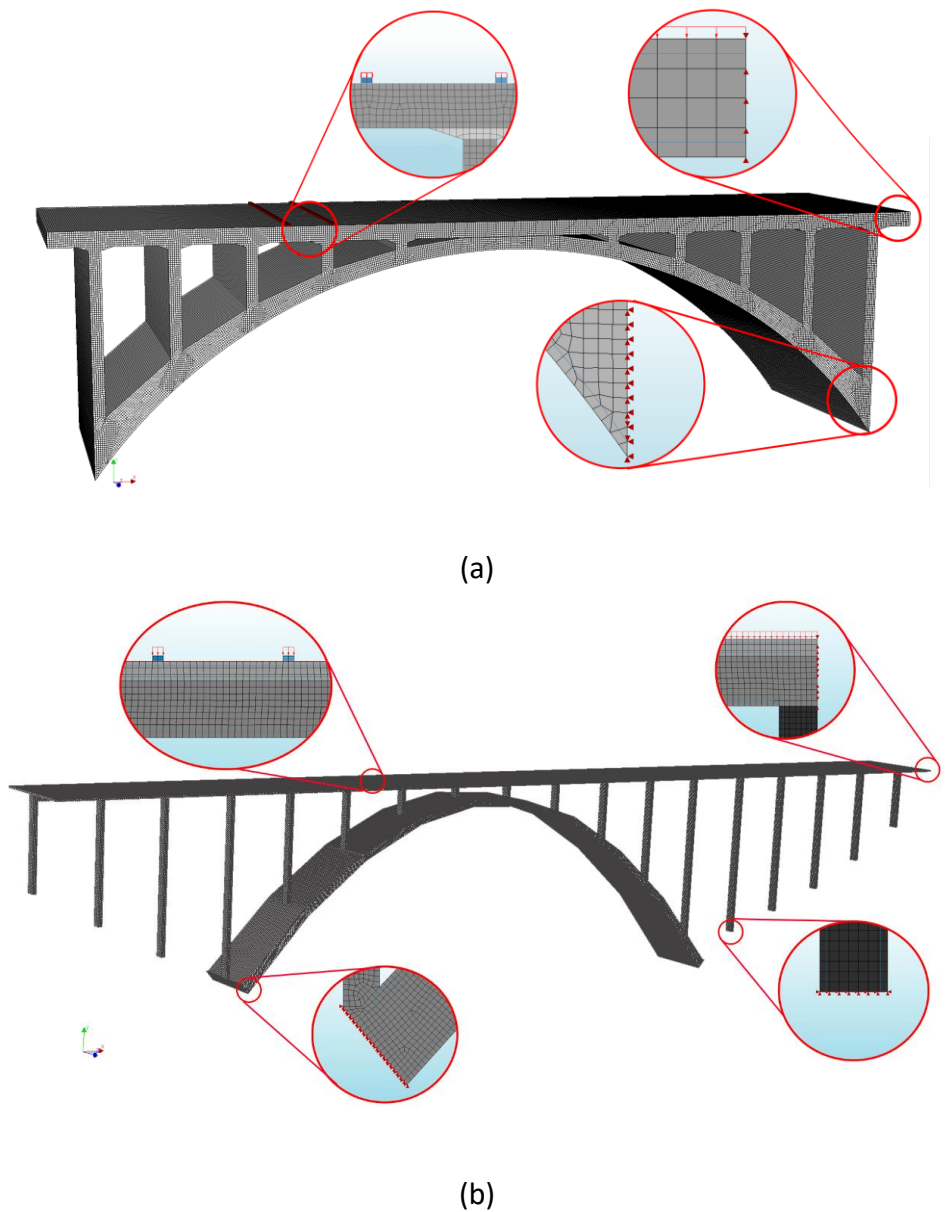
Figure 65 - FEM in DIANA Software using plane stress finite elements (extrude view). (a) Bridge A. (b) Bridge B.

The applied live load is equivalent to the mean value of LM1, considering that the provided characteristic loads of LM1 in the European Committee for Standardization [167] correspond to the 95th percentile of a normal probabilistic function with a coefficient of variation of 15%, according to Matos et al. [168] a 50-year reference period was considered.

The load-bearing capacity of the structure (without any damage) was determined through an iterative-incremental loading procedure allowing the track of the structure's non-linear behavior until its failure. The numerical results are analyzed within the load-displacement curve, and the cracking pattern showed during failure (see Figure 66). The system failure occurs as a progressive failure considering the defined vulnerable zones. The failure is triggered initially by the failure of the deck due to concrete crushing after the yielding of the reinforcement, then the HCR located in the columns presents excessive stresses leading to the failure of the arch due to the high induced moment.
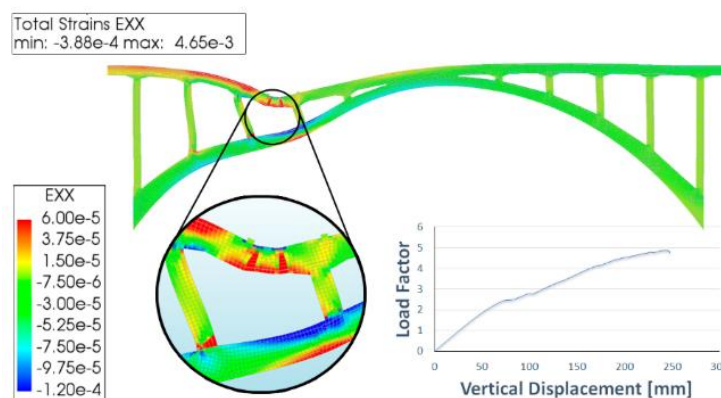
(a)
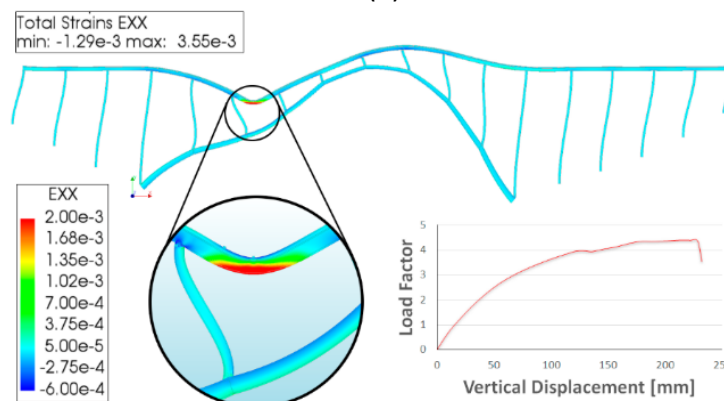
(b)

Figure 66 - Structural non-linear results in DIANA. (a) Bridge A. (b) Bridge B.

4.2.4 SENSITIVITY ANALYSIS

According to expert appraisal, a probabilistic assessment is typically preceded by a sensitive analysis seeking to decrease the number of chosen random variables [169]. Therefore, a reduction in computational cost and procedure optimization is achieved due to selecting parameters with a strong influence on the bridge resistance. The importance of each random variable can be computed according to Equation (29):

$$b_k = CV * \sum_{i=1}^{n} \left(\frac{\Delta y_k}{y_m}\right)\Big/\left(\frac{\Delta x_k}{x_m}\right) \, [\%] \qquad (29)$$

being b_k the importance measure of parameter k, Δy_k the variation in the output parameter due to a deviation of the input parameter Δx_k related to the mean value of the input parameter x_m and y_m is the average response and n is the number of generated parameters. Thus, specific uncertainties (random variables) concerning the geometry and material properties of the structures were initially taken into account, as shown in Table 19.

Table 19. Random variables considered for material and geometry probabilistic characterization.

	Description	Random Variables	Notation	Mean Values	COV
Bridge A	C35/45	Compressive strength	f_{cm}	43 MPa	12%
		Concrete self-weight	γ_c	24 kN/m^3	8%
		Poisson's ratio	ν	0.2	10%
		Modulus of elasticity	E_{cm}	35 GPa	8%
	S500	Yielding and ultimate strength	$f_{sy} \, e \, f_p$	560 MPa	5%
		Reinforcement cross-section area	A_s	--	2%
Bridge B	C40/50	Compressive strength	f_{cm}	40.96 MPa	12%
		Concrete self-weight	γ_c	24 kN/m^3	8%
		Poisson's ratio	ν	0.2	10%
		Modulus of elasticity	E_{cm}	35 GPa	8%
	GA 240/360	Yielding and ultimate strength	$f_{sy} \, e \, f_p$	240 MPa	5%
		Reinforcement cross-section area	A_s	--	2%

A normal probabilistic distribution function characterizes such random variables, and the proposed mean values and coefficient of variation were obtained from the Joint Committee on Structural Safety [170] and Wiśniewski et al. [171].

The computed importance measure of each random variable is graphically displayed in Figure 67. A threshold value of 20% is used to classify the random variables as essential or nonessential for the probabilistic analysis [168]. Therefore, the following random variables were considered for further investigation: i) yielding stress and strength of the conventional reinforcement (f_{sy} e f_p); ii) reinforcement cross-section area (A_s); iii) C40/50 concrete compressive strength (f_{cm}).
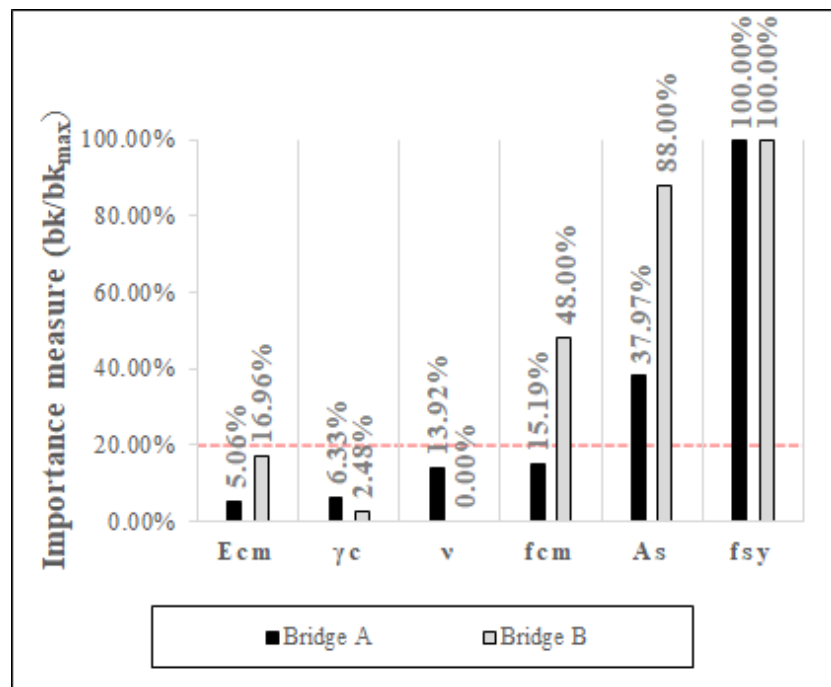
Figure 67 – Random variables importance measure.

The random variable with the highest importance measure was the yielding stress of the reinforcement in both case studies, as reported in Galvão et al. [169], Wiśniewski et al. [171], Matos et al. [168] and Nowak et al. [172] for ductile structures.

4.2.5 PROBABILISTIC ANALYSIS

A probabilistic assessment followed once the deterministic and sensitivity analyses were performed. At first, the probability of failure and reliability of the bridges in their virgin states were computed.

According to Olsson et al. [69], to generate 200 samples of the FEM models described above, aiming to characterize the probabilistic resistance distribution, the Latin hypercube sampling technique was implemented. For each generated sample, a non-linear analysis was performed to quantify the load-bearing capacity of each of the samples. Thus, the probability distribution function of the load-carrying capacity of the case studies was obtained (see Figure 68).

Considering the obtained information concerning the structural system resistance and loading uncertainty in both case studies reliability index can be computed using the Cornell formulation in Equation (30) [173] if a normally distributed function models the resistance and the load.

$$\beta = \frac{\mu_R - \mu_S}{\sqrt{\sigma_R^2 + \sigma_S^2}}$$

(30)

Where: μ_R represent the mean value and σ_R the standard deviation of the resistance, and μ_S and σ_S the mean value and the standard deviation of the load, respectively.

(a)   (b)
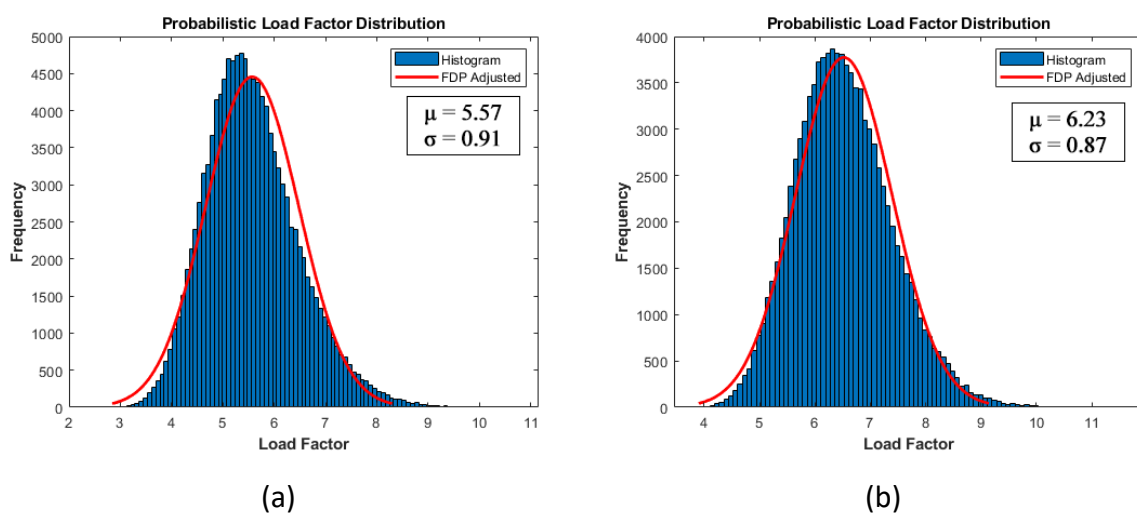
Figure 68 – Probabilistic distribution function of the load-bearing capacity of (a) Bridge A. (b) Bridge B.

Aiming to consider the uncertainty of the model itself in predicting the real behavior of the bridges, numerical model uncertainty concerning the structure's resistance capacity was considered. Such uncertainty model results from simplifications or negligence of the mathematical relations (e.g., 3D effects, inhomogeneities, interactions, boundary effects, simplification of connection behavior, imperfections, among others). The model uncertainty was modeled by a log-normal probabilistic distribution function with a mean value of 1.2 and a coefficient of variation of 0.15, according to the Joint Committee on Structural Safety [170]. Such values are recommended for standard structural finite element models.

The characterization of the structural system resistance previously determined is directly associated with the applied live load, and it is the result of the maximum applied load factor relative to the LM1. Thus, the resistance curve multiplies the mean value of the probabilistic distribution function describing the live load, where its coefficient of variation depends on the random variables that influence the resistance. Therefore, the mean value of the loading probabilistic distribution function shall be defined as a unitary load factor. The associated coefficient of variation is 15%, as Matos et al. [64] recommended. Nevertheless, ideally, the uncertainty concerning the live load should be assessed through monitoring data obtained, for instance, by weight in motion systems.

The obtained indexes (see Table 20) for both bridges are higher than the target reliability index (β_{target}=4.3) established according to the European Committee for Standardization [173] and Sykora et al. [174] for a structural system, considering a 50-year reference period. The relatively high values can be explained by the fact that the performed analysis considers the overall structural behavior considering the moment redistribution through the system. Moreover, the values are often lower order when the analysis is performed at the cross-sectional or element level [169].

4.2.6 RELIABILITY INDEX CONSIDERING DAMAGE PROCESSES

The main goal of the probabilistic analysis, including the previously mentioned damage scenarios (see Section 4.2.2), was to obtain the reliability index of the structures that can estimate the actual condition of the bridge at the time of its inspection. Table 20 presents the obtained reliability indexes for the considered damage scenarios.

Table 20. Obtained reliability indexes for the considered damaged scenarios.

Scenario	Bridge A			Bridge B		
	β	μ	σ	β	μ	σ
No damage	4.96	5.57	0.91	6.23	6.52	0.87
Scenario 1	4.68	5.15	0.87	5.35	5.24	0.78
Scenario 2	4.61	4.24	0.69	6.05	6.24	0.85
Scenario 3	3.89	3.97	0.75	4.92	4.86	0.78

4.2.7 ROBUSTNESS ASSESSMENT

An analysis of the impact of damage is executed in a probabilistic approach as part of the methodology for managing railway bridge safety. Therefore, the magnitude of the identified damages in this section for bridges A and B is progressively increased to understand the structure's capacity numerically against the assessed damage (see Table 21). According to Galvão et al. [175], it is essential to analyze the global impact of the damages with a gradual variation between zero and 100% due to its possible non-linear behavior.

Table 21. Definition of magnitudes for the identified damages scenarios.

Scenario	Bridge A	Bridge B	Damage magnitude			
	Parameters	Parameters				
1	$S_1 = 0.8A_s$	$S_1 = 0.7A_s$	$0.85S_1$	$0.55S_1$	$0.25S_1$	$0.0S_1$
2	$S_2 = 0.8E_{cm}$	$S_2 = 0.8E_{cm}$	$0.85S_2$	$0.55S_2$	$0.3S_2$	$0.2S_2$
3	$S_3 = 0.8A_s + 0.8E_{cm}$	$S_3 = 0.7A_s + 0.8E_{cm}$	$0.85S_3$	$0.55S_3$	$0.3S_3$	$0.2S_3$

The reliability index variation was calculated for each of the bridges and is presented in Figure 69. From the graphics, the behavior of bridge A against the increasing magnitude in the damage scenarios with respect to bridge B is significantly better. In addition, it can be seen that in bridge B, there is a greater affectation to corrosion, making it difficult to maintain its structural capacity.

(a)

(b)
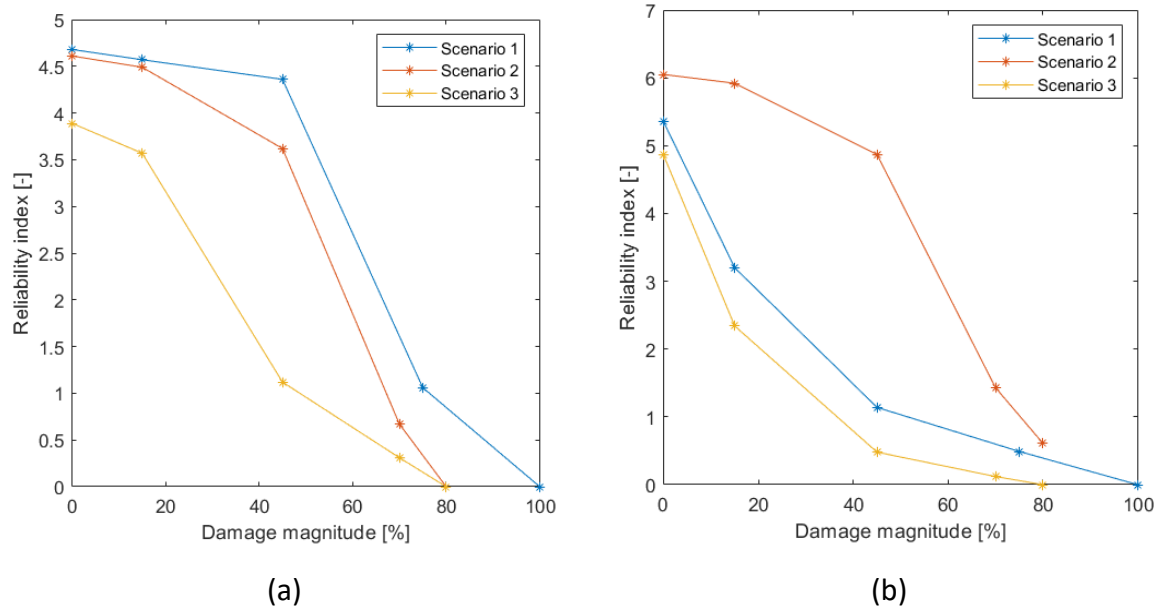
Figure 69 – Variation of the reliability index considering increasing damages (a) Bridge A. (b) Bridge B.

As already explained in subsection 4.1, to calculate the robustness indicator, it is necessary to normalize the results obtained from the variation of the reliability index and thus define $f(D)$. However, due to the computational expense for the calculation of each β, we proceed to define $f(D)$ as a discrete function considering critical points of its behavior. Figure 70 shows the areas formed for each of the damage scenarios. Once the results are normalized and graphed for both bridges, comparisons are allowed. Therefore, it can be deduced how robust the bridge is for each damage scenario and magnitude, for example, at 45% or 100%. Thereby, calculating the area under the curve in the desired limits is necessary to obtain the robustness indicator at that magnitude.
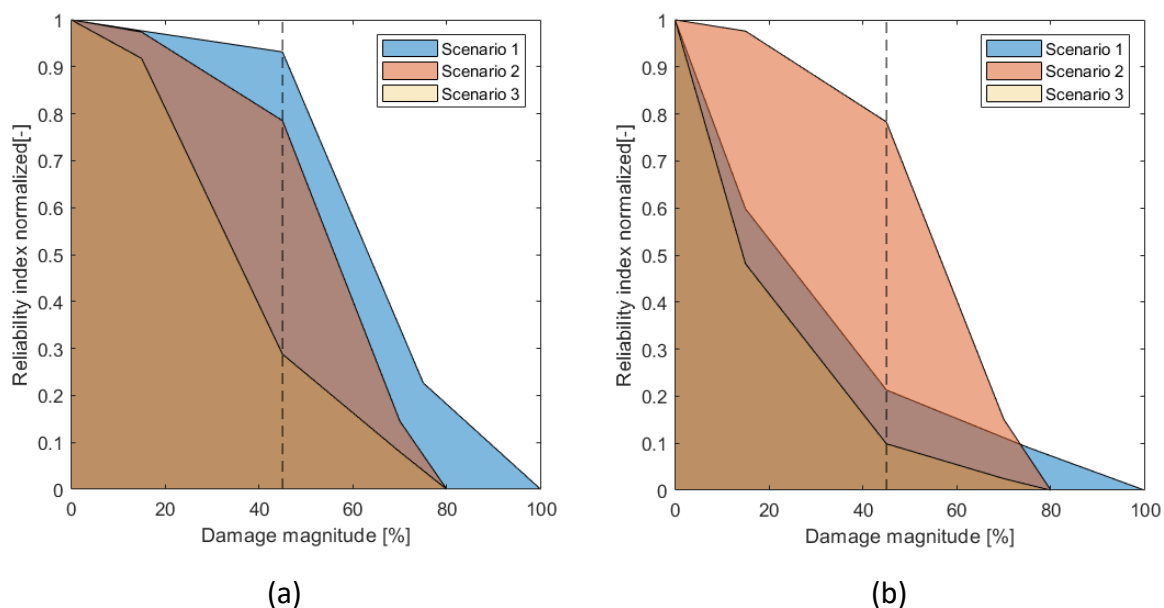
Figure 70 – Graphical display of robustness indicator for each damage scenario (a) Bridge A. (b) Bridge B.

The robustness indicator was calculated following equation (28) for the 45% and 100% magnitudes. However, since the function to be evaluated is discrete, numerical integration is performed by calculating trapezoidal areas, and the results are presented in Table 22.

Table 22. Robustness indicator results.

Scenario	Bridge A		Bridge B	
	$I_R^{45\%}$	$I_R^{100\%}$	$I_R^{45\%}$	$I_R^{100\%}$
1	43.45%	63.65%	24.15%	29.87%
2	41.19%	53.55%	41.21%	53.64%
3	32.47%	37.46%	19.82%	21.48%

As the robustness indicator was designed to compare different types of structures in the presence of common damage or hazards, the following points can be highlighted: i) The results obtained for bridge A show a behavior between medium and maximum robustness for the pathologies studied. However, Bridge B shows a minimum robustness behavior, considering the 45% and 100% magnitude of corrosion of the reinforcing steel. ii) Bridge A has a smaller span between the piers than Bridge B, which can explain the lower tensile stresses in the elements of Bridge A, which take longer to reach their maximum stress; iii) for Bridge B, it is noted that brittle failure of the structural elements and their subsequent collapse can occur

from a 15% increase in corrosion levels, unlike Bridge A where the cross-sections of the structural elements are much larger.

4.3 FINAL REMARKS

The aim of this chapter was to describe the theoretical and practical basis for conducting and implementing the workstreams 3 and 4 proposed for this research. In this sense, subchapter 4.1 was dedicated to compiling the state of the art on the methods to be used. Consequently, in subchapter 4.2, the probabilistic analysis is carried out considering a FEM approach. In this sense, two case studies of the same bridge type and structural similarities were selected for analysis and subsequent comparison in terms of reliability and robustness.

With respect to these case studies, several limitations can be described in terms of the general framework. First, the finite element models do not consider soil-structure interaction due to the studied problems for these bridges did not include deficiencies in their foundations or problems related to flooding. Second, the probabilistic approach for the reliability calculations did not consider the methodology based on surrogate models because the elements used in DIANA were 2D shells and the computational effort for each scenario is much lower than considering solid elements in 3D. Third, only one type of collapse under static loading was considered. However, for the type of structural pathologies studied, other types of failure could be considered.
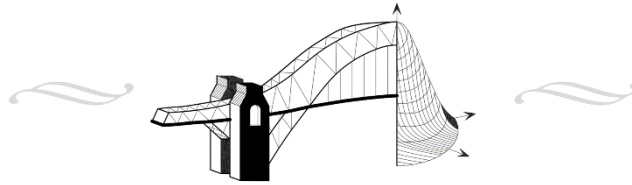
LEÇA RAILWAY BRIDGE ASSESSMENT

5.1 CASE STUDY DESCRIPTION

The case study comprises a granite stone arch bridge over the Leça river in Ermesinde, Portugal. It is located at the PK09 of the Minho railroad and was built in 1875. The arch bridge has a 16 m span with a maximum height of 18 m and a total width of 5.31 m which means the bridge only supports one rail track composed of concrete monoblock sleepers and UIC60 rails on a ballast layer with variable height. The voussoirs thickness composited by the same material is approximately one meter. As part of the design, four granite stone masonry wing walls were proposed to reinforce the bridge abutments. Subsequently, a new pre-stress concrete bridge was built next to it, with the objective of a second track in the Minho line (see Figure 71 and Figure 72).

(a)   (b)

Figure 71 – Leça railway bridge: (a) upstream view, and (b) downstream view.

The Leça railway bridge has been under several studies and inspections to maintain its serviceability and preserve it as a structure heritage. Infraestruturas de Portugal (IP), the Portuguese authority for the conservation of bridges, performed the last global inspection at the end of 2020, assessing the structural components through a visual inspection. Therefore, the overall state of the bridge elements is summarized in Table 23.
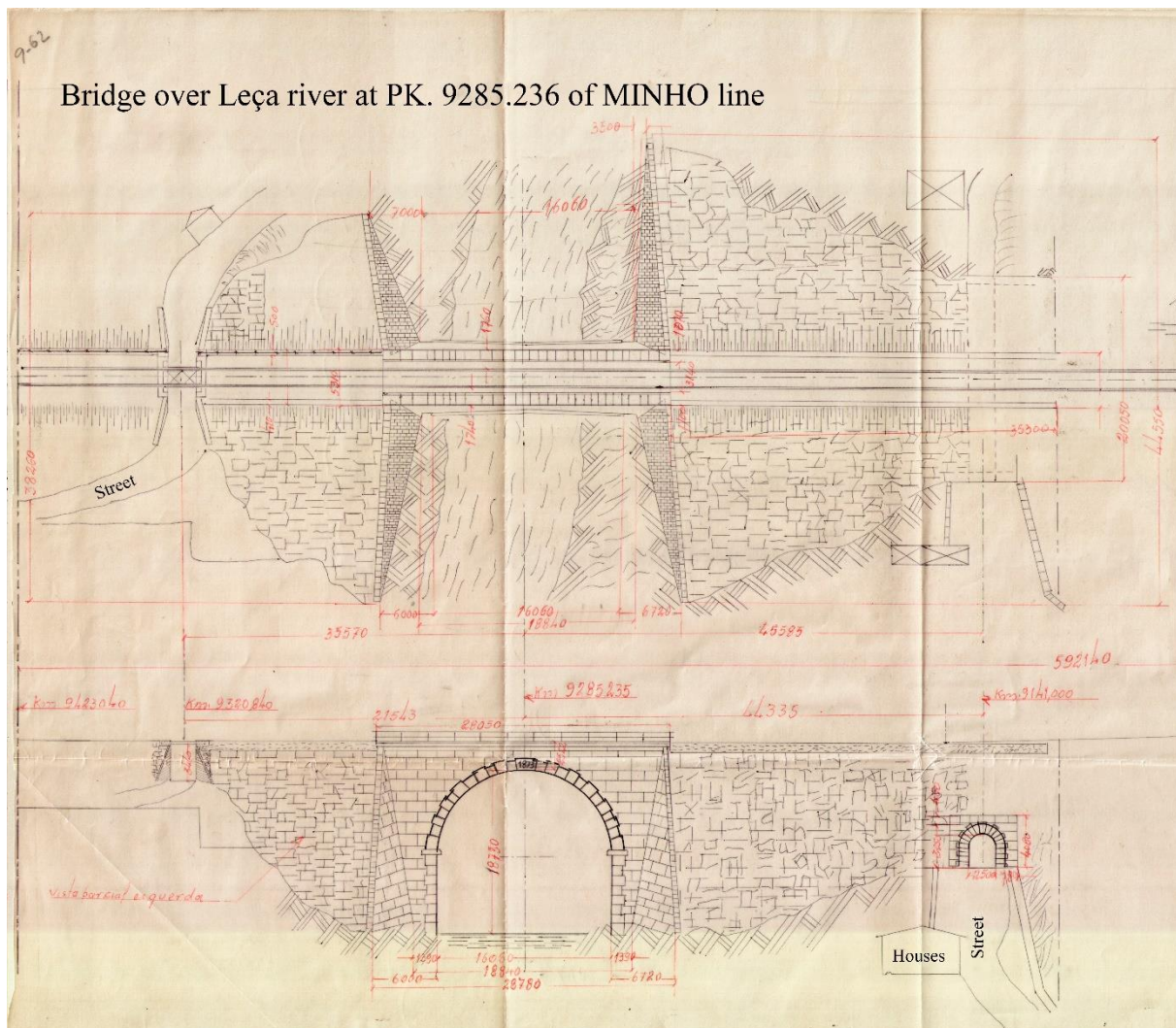
Figure 72 – Leça railway bridge original blueprints provided by "Infraestruturas de Portugal".

Taking into account the overall assessment, the inspection report specifies the structural anomalies on the railway bridge to provide an overview of its current condition. Therefore, the elements with a score of 1 to 2 are considered to compromise the structure's durability. Figure 73 depicts the location and respective photos of the observed anomalies: (a) biological pollution on the retaining walls; (b) efflorescence on the deck and arch (caused by lack of

drainage); (c) corrosion into the parapets; and (d) crack in the stone joints. However, the problems encountered do not affect the structural behavior and are insignificant as a degradation scenario for the safety assessment.

Table 23. General results of the visual inspection of the Leça railway bridge [176].

Elements	Conservation state	Description
General overview	2 (IC)	Existence of anomalies with impact on the durability but insignificant impact on the structural behavior
Retained walls	2 (IC)	Existence of anomalies with impact on the durability but insignificant impact on the structural behavior
Abutments	0	Insignificant anomalies
Deck	1	Existence of anomalies that compromise the durability
Rail	0	Insignificant anomalies
Ballast	0	Insignificant anomalies
Parapets	2	Existence of anomalies with impact on the durability but insignificant impact on the structural behavior
0 – Excellent state 1 – Normal state 2 – Satisfying state 3 – Deficient state 4 – Severe state 5 – Limit state IC – Conditional inspection: used when total element verification is impossible.		

This case study has been the subject of various studies to characterize its behavior and structural capacity. Several factors determined the selection of this bridge: (1) the need for financial support to improve various aspects of the rail network, and the railway bridge was selected as the structure to achieve this goal; (2) the age, type, and foundation of the bridge (masonry with shallow foundations and a single span), which are consistent with the statistics of the most common railway bridges in Europe; (3) the availability of various types of data, such as e.g., structural blueprints, dynamic measurements, hydrological data, geotechnical characterization, and topographic information for the area. For example, Arêde et al. [177] performed an experimental characterization of the bridge materials (granite stone) and the

masonry joints through core sampling and in-situ tests on the bridge abutments and the arch, compiled in Table 24. Moreover, Silva et al. [178] used the Arêde et al. [177] experimental results and provided calibrated and validated parameters for the Drucker-Prager model, resulting from the agreement between those data and the numerical simulation outcomes. Therefore, the resulting constitutive model is applied in the present investigation to analyze and calibrate the finite element model (FEM) [179], [180].
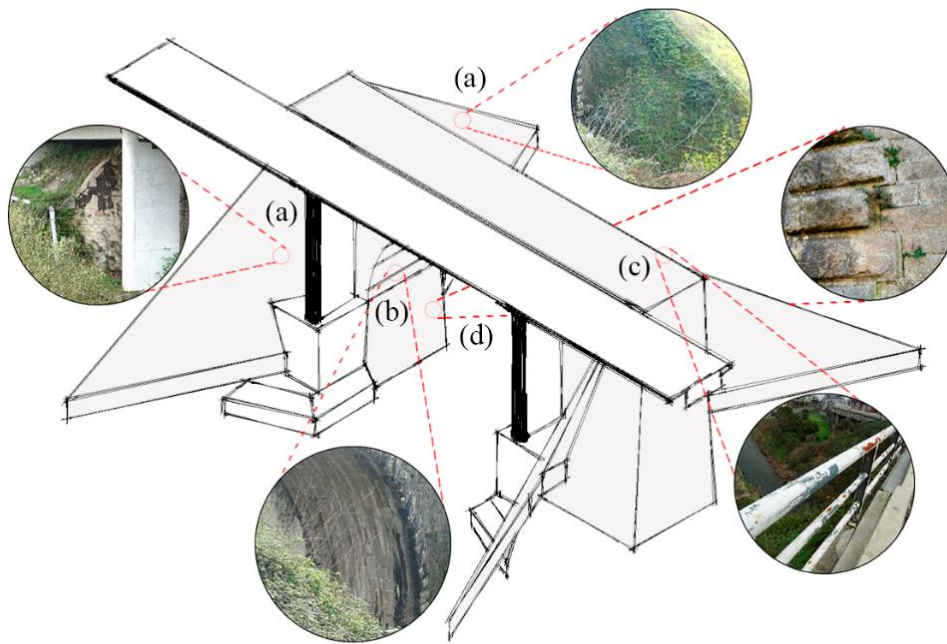
Figure 73 –Main observations of the visual inspection and corresponding anomalies: (a) biological pollution; (b) efflorescence effects; (c) corrosion; and (d) crack.

Table 24. Physical and mechanical parameters of the Leça river bridge stone [177].

Parameter	Experimental data (average values)	Test type standard
Unit weight (kN/m³)	25.2 - 25.7	-
Compressive strength (MPa)	35.9 – 81.4	NP EN 12504-1 NP EN 12390-3
Tensile strength by diametrical compression (MPa)	2.3 – 5.2	NP EN 12390-6
Elastic modulus (GPa)	6.8 – 10.9	NP EN 14580

5.2 NUMERICAL MODELING

5.2.1 FE MODEL GENERALITIES

The methodology outlined in subsection 4.2 and Baron et al. [181] was used to conduct the safety assessment for the case study. In this sense, a finite element model (FEM) was built to analyze the structural behavior of the Leça railway bridge. The DIANA FEA software was considered in this study applying a three-dimensional model using an eight-node quadratic element, where the nodes of the solid simulate the translations u_x, u_y and u_z yielding the deformations du_x, du_y and du_z of an infinitesimal part $(dx\, dy\, dz)$ of the element. Moreover, DIANA calculates from these deformations the strains and Cauchy stresses of each component (see Figure 74).
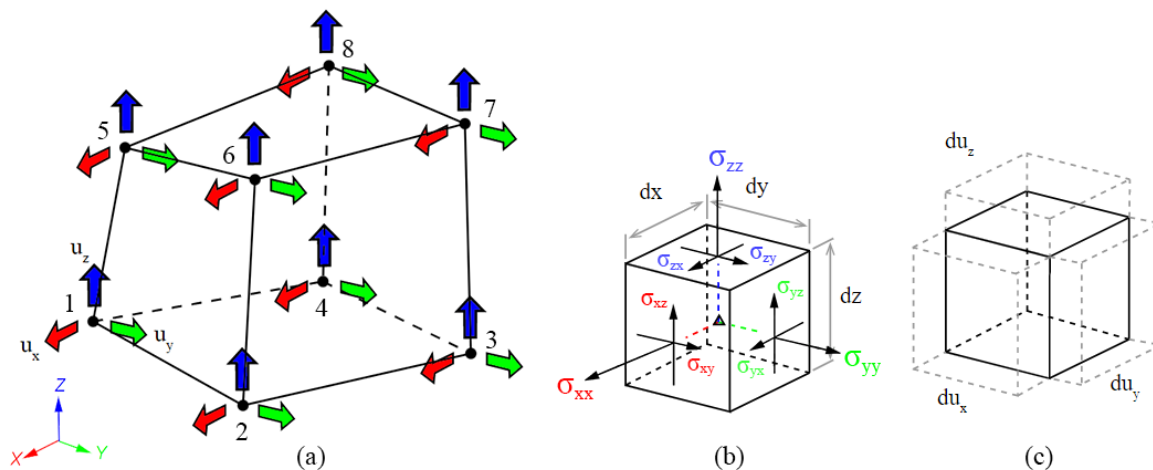
Figure 74 – Solid element: (a) displacements; (b) strains and Cauchy stress; and (c) deformation.

The FEM of the railway bridge is divided into several components (e.g., spandrel walls, arch, abutments, among others) modelled by the solid elements under a macro modelling approach [182]. The non-linear behavior of the granite stone and the soil layers was simulated with a constitutive model based on the Drucker-Prager model available in the Diana model's library [163], which considers the elastic-plastic behavior. Besides, the Drucker-Prager model has a yield condition approximating the Mohr-Coulomb yield surface (conical surface in the principal stress space), while the hardening behavior is defined as an exponential function (see Figure 75).
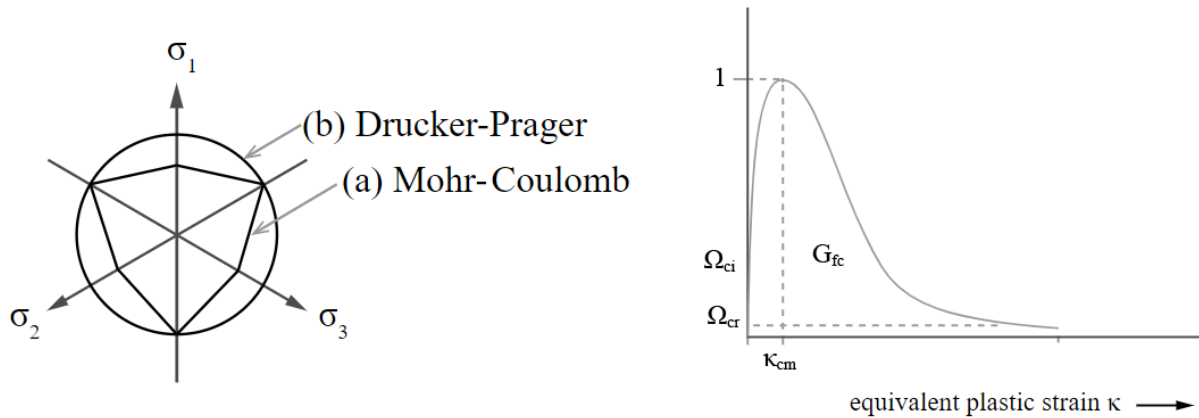
Figure 75 – Drucker-Prager yield condition and exponential hardening [163].

Several types of loads were used to test the case study's load-bearing capacity, including permanent, hydrostatic, and live loads. The last type of load used was the model LM71 proposed for railway bridges design by the Eurocode [167], which consists of the application of four punctual loads of 250 kN spaced in 1.6 m and a uniformly distributed load of 80 kN/m, applied in the most unfavorable position, which according to Adrião [183] is located near the ¼ span of the arch; this assumption is sustained after calculating the influence line diagram of the case study. Figure 76 shows the characteristic values applied to the rail tracks considering regular traffic.
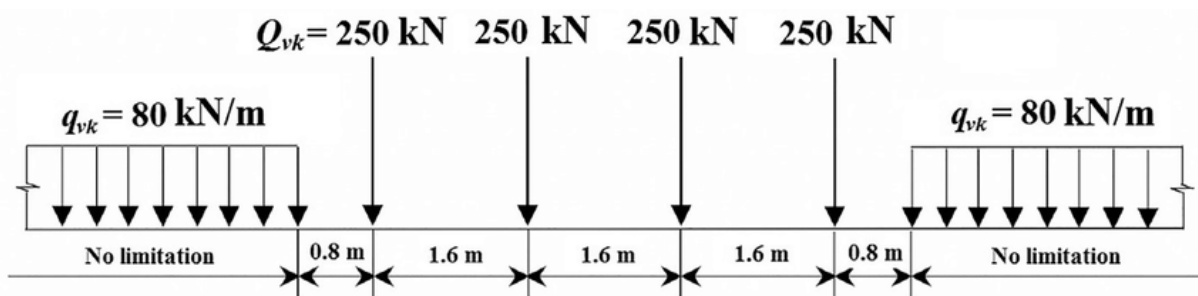
Figure 76 –Load model LM71 [167].

5.2.2 BOUNDARY CONDITIONS

Concerning the boundary conditions, rigid supports were used in the transversal direction to simulate contact with the wing walls. Besides, the bridge presents confinement in the longitudinal direction, and it was modelled by restricting all degrees of freedom of the abutment's out-layer plane. Nevertheless, the definition of foundation support and how it will

be simulated is not an easy choice. The soil-structure interaction in a 3D model directly impacts the model's computational time and effort. However, the modelling strategy has to be in accordance with the representation of the scour damages. In this sense, the soil was represented as a component of the FEM by using an eight-node quadratic element as well. Regarding the confinement of the ground, it was limited in the direction perpendicular to the out-layer planes (except for the top layer). Figure 77 shows graphically the boundary conditions assumed in the FE model.
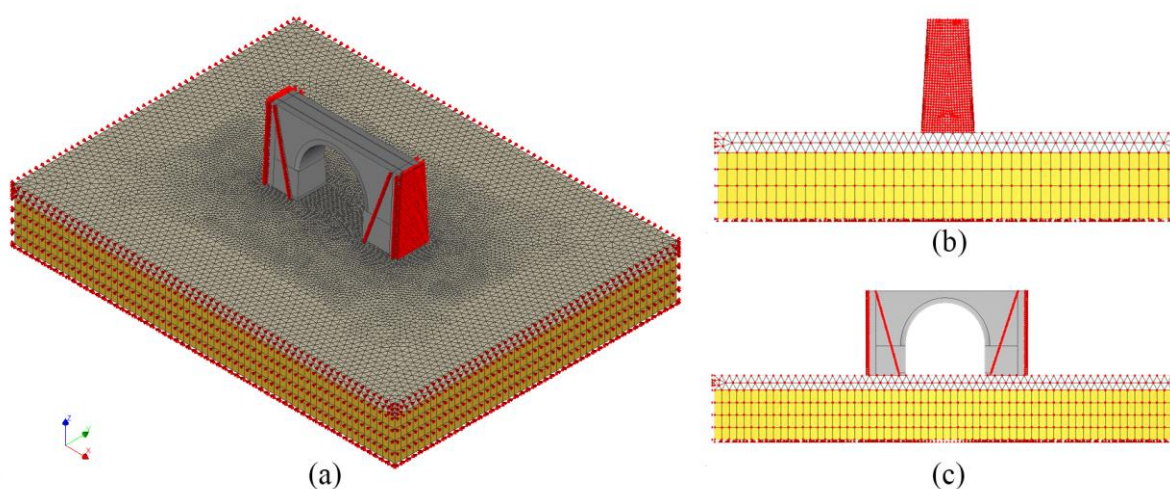
Figure 77 – FEM in DIANA software using solid elements: (a) 3D view; (b) lateral view; and (c) front view.

5.2.3 DYNAMIC CALIBRATION

In order to characterize the dynamic properties with field measurements, different types of vibration tests have been developed; the aim of these tests is collecting voltage data generated by the vibration of the structure. However, a numerical process of modal identification is required to determine the acceleration of the structure, since this is the basis of the dynamic properties sought [184].

According to Carvajal [185], vibration tests can be divided into two types, experimental modal analysis (EMA) and operational modal analysis (OMA). The main difference between them is the excitation of the structure. EMA is triggered by a known excitation force, while OMA is based on environmental excitations (e.g., wind forces, vehicle traffic). However, since these forces cannot be measured, they are assumed to be white noise.

There are two types of EMA tests: i) forced oscillations and ii) free oscillations. In the first test, a controlled excitation must be applied to the structure under study (this parameter is considered as an input signal). The output data are recorded with a special device (acceleration data). This type of test is very complex due to the high cost of the equipment and the safety of the structure.

For the second test, the authors in [184], [185] define the excitation used as an initial deformation that produces free motion. This test can be performed using strain cables or an impact force in a specific zone. As mentioned earlier, the OMA is based on an ambient excitation where only the initial parameters are recorded, since no artificial excitation is required, and is referred to as an ambient vibration test (AVT). According to Jaishi [186] the advantage of AVT is its low-cost equipment and uninterrupted operating condition while the test is being performed.

As already mentioned, there has always been uncertainty in all the variables that compound a FE model. Nevertheless, deterministic values are traditionally used in the design or the analysis of existing structures. Therefore, the FE model parameters must be adjusted to reality through characterization and validation [186]–[188].

This research used the experimental data processed from the ambient vibration test recorded by Adrião [183] and the procedure performed by Costa et al. [179] and Silva [189] to calibrate and validate the modelled bridge case study. The modal analysis of the bridge was performed using the mean values as a basis of the FE model obtained from Silva [180], where the comparable values are the first two vibration modes (i.e., natural frequencies and mode shapes). Figure 78 shows the graphical comparison between the numerical analysis and the experimental test results.
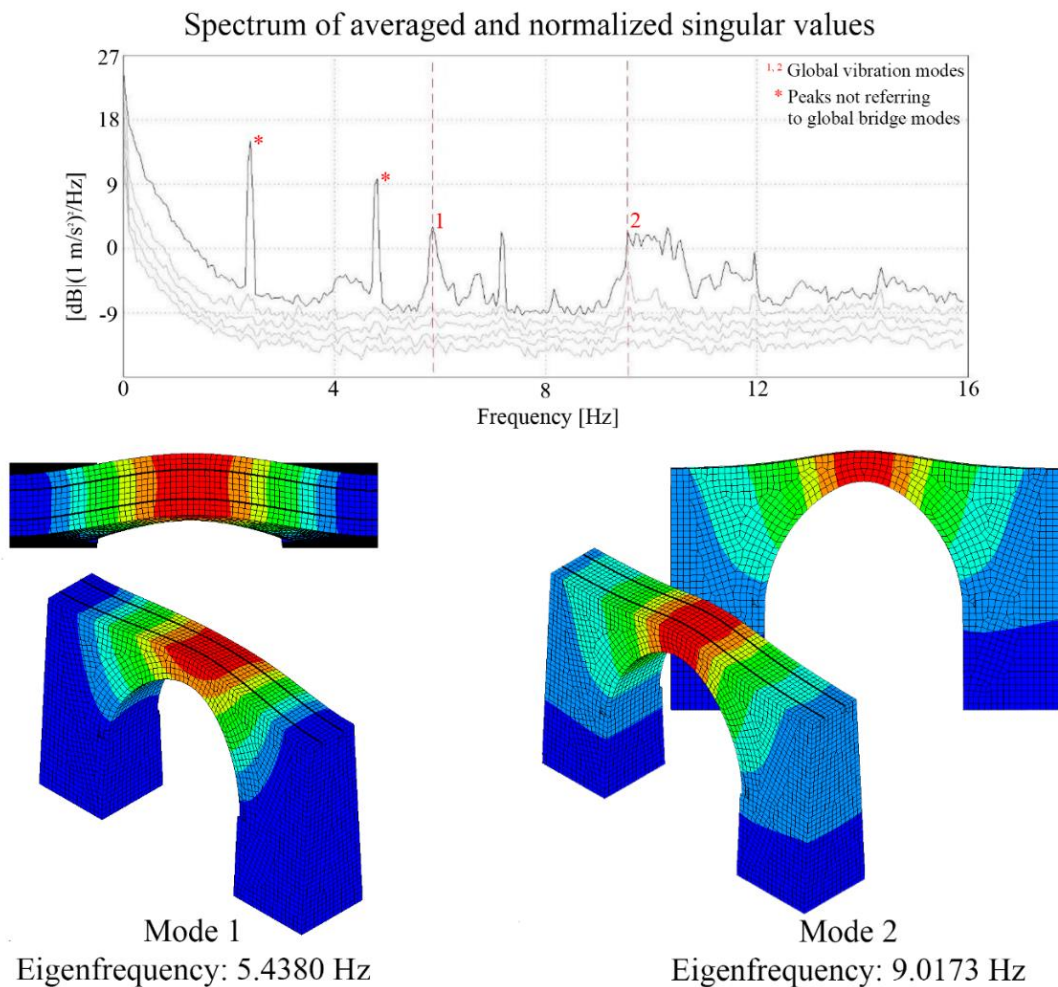
Figure 78 – Graphical comparison between the numerical analysis and the experimental test results [183].

Due to the high value of the obtained error, the numerical model must be calibrated. Consequently, the FEM requires a modification of the parameters to achieve a permissible error, and the dynamic response corresponds to the experimental tests. According to Rangel [184], the model adjustments are implemented through the calibration parameters. In this sense, the mass and stiffness are the variables with a direct impact on the structure's dynamic. Since there is uncertainty about the elasticity modulus of the granite stone masonry, it was chosen as the basis for assessing the accuracy of the model.

$$\text{Error} = \left| \frac{v_A - v_E}{v_E} \right| \times 100\% \qquad (31)$$

Table 25 shows the variation of the masonry elasticity modulus through iterations and the associated percentage errors with the experimental data by Equation (31) where ν_A is the numerical value, and the ν_E is the experimental value.

Table 25. FE model calibration through modulus of elasticity iteration of granite stone masonry.

Elasticity modulus [GPa]	Mode 1 - frequency [Hz]		Error	Mode 2 - frequency [Hz]		Error
	Experimental	Numerical		Experimental	Numerical	
2.00	5.850	5.438	7.04%	9.700	9.017	7.04%
2.02	5.850	5.492	6.12%	9.700	9.107	6.11%
2.11	5.850	5.773	1.31%	9.700	9.568	1.36%
2.15	5.850	5.871	0.35%	9.700	9.729	0.30%

Despite the acceptable error percentage obtained for a modulus of elasticity of 2.11 GPa (relative error less than 5%), a slightly higher modulus of elasticity (with an increase of less than 2%) of 2.15 GPa was chosen in the present study because it provides more conservative values (see Table 25). This is particularly important since this study only considered the calibration of one parameter, namely the elasticity modulus of the granite stone masonry (E_m). Reducing the discrepancy between the experimental and numerical results by more than 70% (from 2.11 to 2.15 GPa) provides a higher level of confidence for performing the sensitivity analysis (topic of Subsection 3.4).

5.2.4 SENSITIVITY ANALYSIS

A sensitivity analysis at this stage is applied to reduce the random variables to be considered in the optimized numerical simulation. Therefore, the sensitivity analysis tested the FE model in two distinct ways: i) physical properties of the bridge materials considering only the performance of the bridge until failure; and ii) physical properties of the soil and bridge materials, regarding the soil-structure interaction and the maximum bearing capacity of the foundation soil. The random variables were characterized by a normal distribution in which the selected mean values and corresponding covariances (COV) were selected based on the suggestions and experimental results from Conde et al. [190] and the JCSS [170] and are summarized in Table 26.

Table 26. Considered random variables for probabilistic material characterization.

Description	Random Variables	Notation	Units	Mean Values	COV (%)
Granite stone masonry	Modulus of elasticity	E_m	[MPa]	2150	10
	Cohesion	C_m	[MPa]	0.45	15
	Friction angle	F_m	[º]	35.5	10
	Dilatancy angle	D_m	[º]	17.75	10
	Tensile strength	f_t	[Mpa]	2.5	10
Granite stone infill	Modulus of elasticity	E_i	[MPa]	343	10
	Cohesion	C_i	[MPa]	0.45	15
	Friction angle	F_i	[º]	35.5	10
	Dilatancy angle	D_i	[º]	17.75	10
Soil Layer 1 and 2	Modulus of elasticity	$E_{s_{1,2}}$	[MPa]	150	10
	Friction angle	$F_{s_{1,2}}$	[º]	40	10
Soil Layer 3	Modulus of elasticity	E_{s_3}	[MPa]	7000	10
	Cohesion	C_{s_3}	[MPa]	70	15

Figure 79 illustrates the results of applying Equation (29) to the two types of failure criteria for determining the important measure of the random variables. Therefore, this analysis considers a 20% limit to the importance measure to obtain the variables that have more influence on the probabilistic analysis. [168].

For the first scenario, the random variable with the highest importance measure on the failure bridge response was granite stone cohesion, as reported in [191]. For the second scenario, several variables have a direct impact while the soil reaches its maximum bearing capacity. Therefore, the following variables were selected for the probabilistic assessment: i) elasticity modulus of the masonry (E_m); ii) cohesion of the masonry granite stone (C_m); iii) elasticity modulus of the soil layer 1 and 2 ($E_{s_{1,2}}$); iv) friction angle of the soil layer 1 and 2 ($F_{s_{1,2}}$).
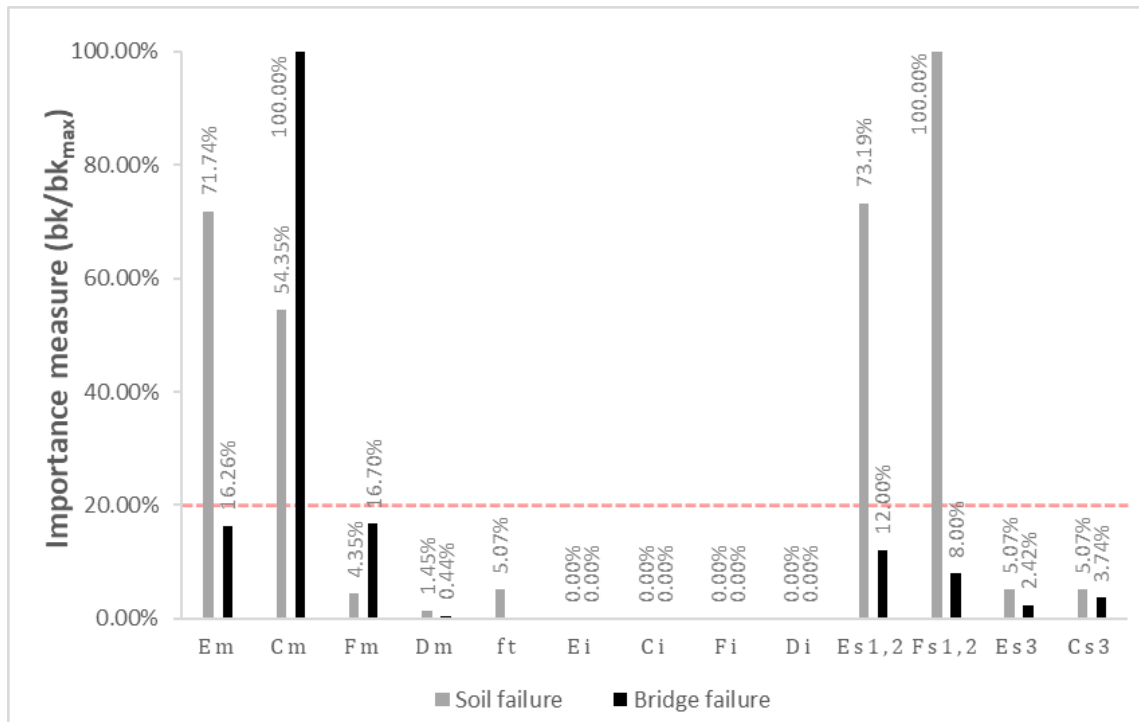
Figure 79 – Importance measure for random variables considering failure modes.

5.3 DAMAGE SCENARIOS

Thereafter, it was necessary to simulate the effects of extreme floods in the FE model, in order to subsequently develop and test the application of the surrogate model. In this sense, the following damage scenarios were proposed (see Table 27), where the main parameter to be considered was the sum of the scour depth due to the contraction scour caused by the decreasing cross-section of the channel and the local scour at the abutments. Therefore, these damage scenarios were introduced into the numerical model by removing the soil material under the foundation according to the geometric scour profile recommended by Zampieri et al. [192], as shown in Figure 80.

Subsequently, 200 FE models for each damage scenario were defined considering the selected random variables and generated through the Latin Hypercube Sampling (LHS). Therefore, the load-bearing capacity of each generated sample is quantified by performing a non-linear analysis.
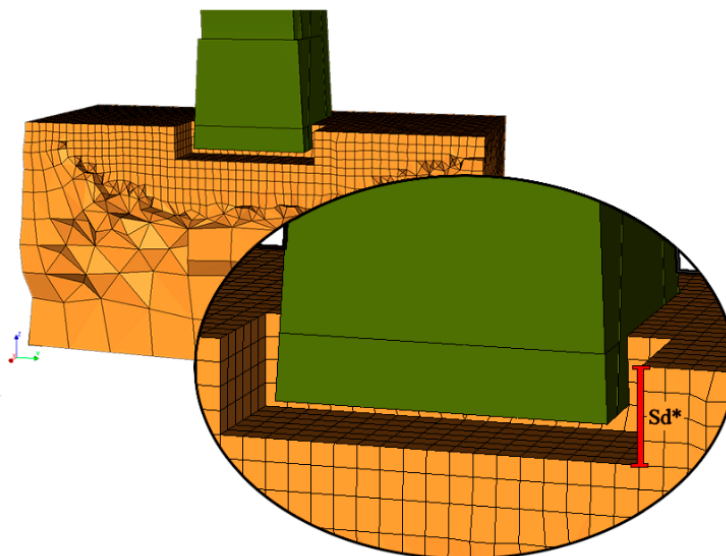
Figure 80 – Scour depth (S_d) modelling strategy.

Table 27. Definition of the damages introduced into the FE model.

Scenario	Scour depth (Sd) [m]	Hydrostatic load (water level) [m]
1	1.0	1.0
2	1.5	1.5
3	1.6	3.5
4	1.7	4.3
5	1.8	5.0
6	1.9	3.79
7	2.0	2.0
8	2.1	1.5
9	2.2	3.7
10	2.5	2.5
11	3.0	3.0
S_1: Damages introduced to the right abutment.		
S_2: Damages introduced to the left abutment.		

5.3.1 STRUCTURAL FAILURE MODE

After the previous section established the FE model guidelines, the structure is analyzed through a non-linear probabilistic-based analysis where the total static load capacity of the

structural failure is determined. At first, the structure is analyzed without any damage to characterize the maximum capacity of the structure (see Figure 81). Therefore, after a load factor of 12, the arch and the spandrel walls enter a state of plasticity. The failure occurred in the arch through one plastic hinge near the loading zone. Then, the damage scenarios are gradually applied to analyze the behavior of the bridge against the instabilities caused by the lack of soil. In this sense, after reaching a depth of 1.5 m (considering that the foundation is buried at this total depth), cracking patterns can be observed in the piers, the base of the foundation, the spandrel walls, and the arch with an increase of magnitude in the last two elements (compared to the undamaged model). However, the failure mode remains the same, considering a lower static loading applied. Figure 82 shows the cracking example assuming scour in the left abutment with a depth of 2 m.
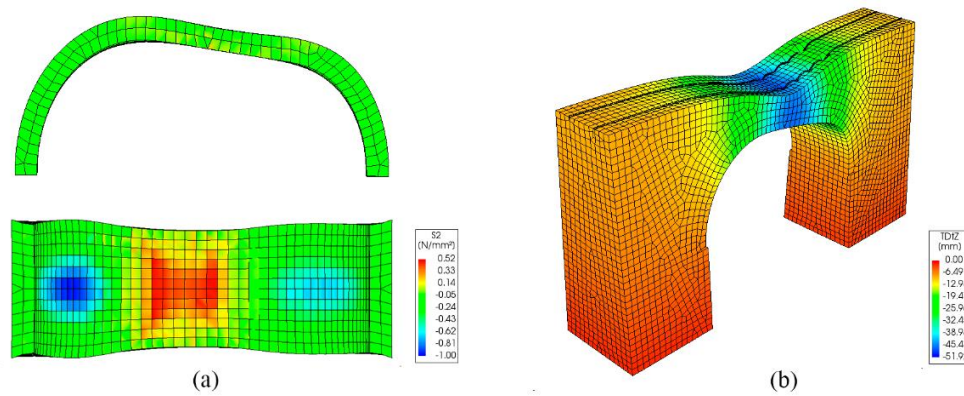
Figure 81 – Structural behavior under incremental static load: (a) stress located in the arch; and (b) 3D graphic of global displacements.
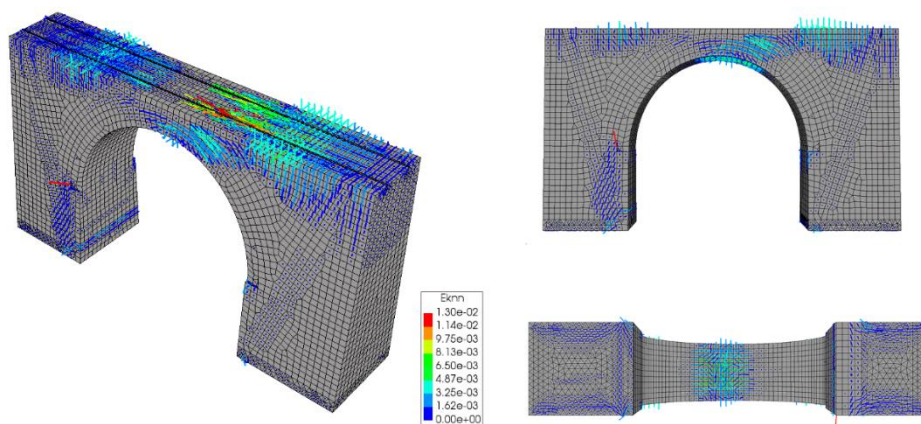
Figure 82 – Crack strains obtained from the FE model ($S_f = 2\ m$).

5.3.2 SOIL FAILURE MODE

For the second failure mechanism analyzed, the ultimate bearing capacity of the soil (R_d) was investigated in its undamaged form. Moreover, the design contact stress (σ) was specified with a value of 470 kPa for the shallow foundation defined by the ratio of F/A_{eff}, where the F is the applied vertical force and A_{eff} is the effective area of the foundation. The vertical bearing capacity of the foundation soil was verified according to the inequality of $\sigma \leq R_d/SF$, where SF is a safety factor which in this case adopted a value of one. Consequently, the theoretical R_d (the bearing capacity of the foundation) was estimated by applying the formulation based on the J. Brinch - Hansen theory [193], which considers factors of the foundation such as the bearing capacity, geometry of the foundation (shape, depth, inclination), and slope of the terrain.

Nevertheless, the configuration of the soil layers (weaker soil underlined by stronger soil) requires the definition of the failure mechanism. According to Yang et al. [194], the failure surface depends on the relation between (h/b), where h is the thickness of the weaker soil and b is the half-width of the footing (see Figure 83). As this relationship is lower than 1, the failure surface is fully located in the weaker soil layer. Therefore, the theoretical R_d was estimated considering the parameters of the weaker soil, obtaining a value of 6050 kPa.
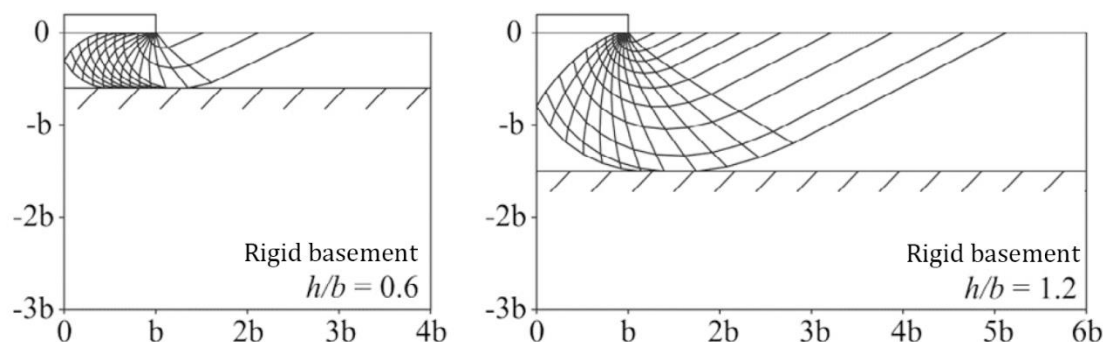
Figure 83 – Failure mechanism considering a weaker soil underline by stronger soil for different values h/b (adopted from [194].

Moreover, the bearing capacity of the soil was calculated from the FE model by testing the soil material, by applying incremental pressure as a result of the non-linear analysis of the arch bridge. Different load cases were inspected to determine the vertical displacement of the soil

(z-direction). Figure 84 shows the contour plot of TDtz for the 1.37, 2.24, 3.47, 4.60 and 5.95 load factors of the imposed load (1 Mpa).
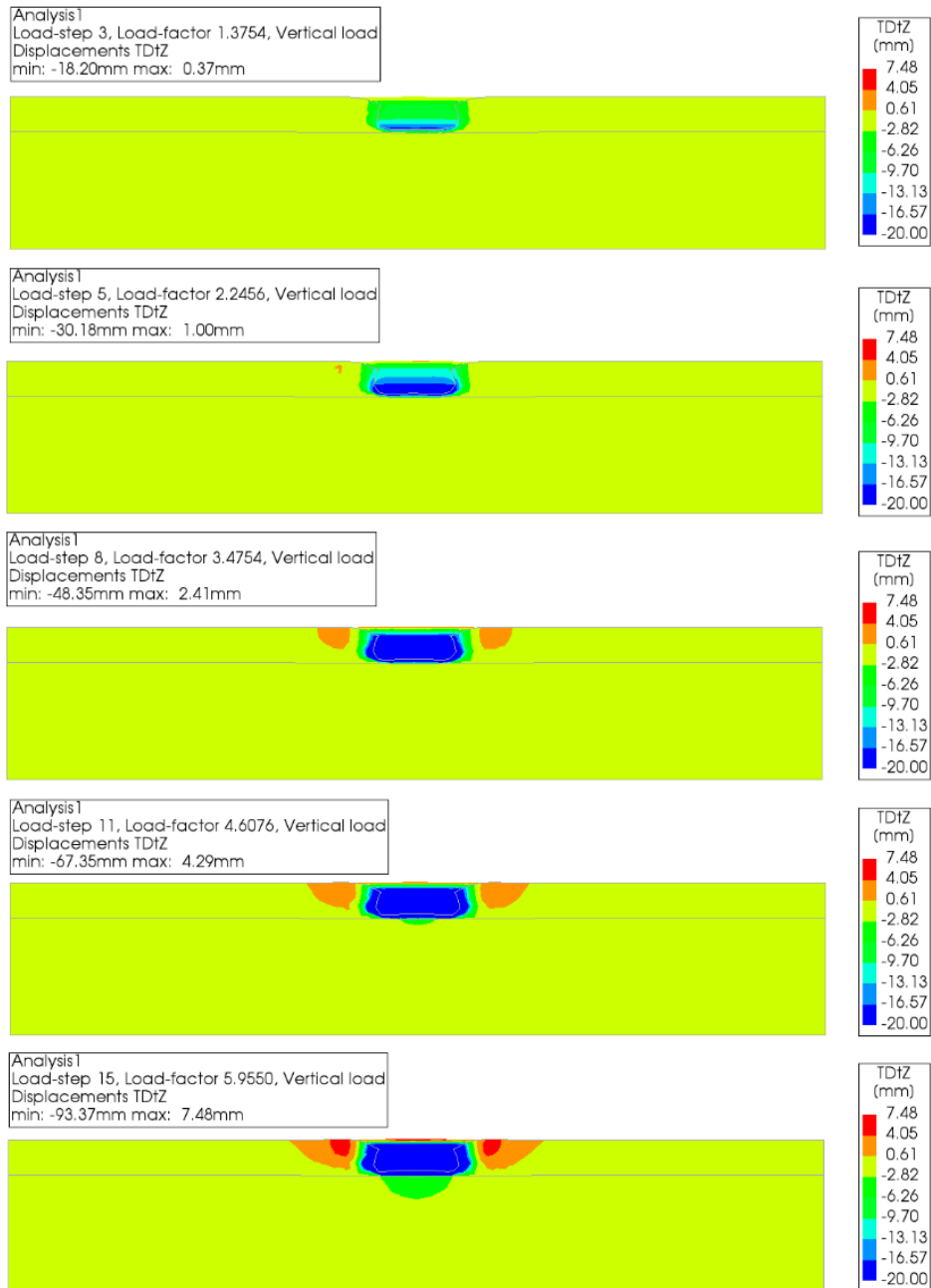
Figure 84 – Displacements TDtz results from the non-linear analysis.

From the results, it can be observed the vertical displacement of the footing increased with the imposed pressure. In particular, it was possible to observe a soil region where all points

had similar vertical displacement. The load step 15 plot of the total displacement provided visual information regarding the failure mechanism of the soil.

In this sense, it was possible to identify the failure surfaces in the soil. The first region (in blue) denotes the vertical movement of the soil with the footing. The second region (in green) is under rotation and is also called the radial shear zone. Finally, the third region (in red) is pushed towards the top and is known as the Rankine passive zone.

The elements on the soil surface with the highest stress were located to determine the ultimate bearing capacity of the soil. As expected, the soil reached a maximum bearing capacity when $q_u \approx 6000$ kPa, which was hereinafter the criteria to determine the failure of the soil. This failure mechanism was therefore considered when the scour depth in the abutment exceeded 2.5 meters.

5.4 RELIABILITY ANALYSIS

5.4.1 GENERALITIES

The reliability analysis takes advantage of the capabilities of the surrogate modelling technique to optimize the computational resources [143]. After the sensitivity analysis is performed, it is possible to identify the variables with the highest impact on the structure's load-carrying capacity, which will be used to implement a surrogate model [195]. Subsequently, the capacity curve of the structure for a given scour depth value is obtained and compared with the loading curve to compute the reliability index using the subset simulation technique [196]. Additionally, model uncertainties are being considered in the process to obtain the failure probability of the structure JCSS [197]. Finally, a fragility curve is then constructed by repeating the process for each value of scour depth.

5.4.2 SURROGATE MODEL

Kriging metamodels used in combination with subset simulation (AK-SS) have been used to describe the non-linear limit state function [143] and successfully applied to the reliability and fragility assessment of arch bridges under scour scenarios [156]. Then, a Kriging surrogate model using UQlab was created and validated based on previously defined random variables. The surrogate model uses a universal trend type, an anisotropic ellipsoidal Matérn 5/2

correlation function, which defines the Gaussian process and cross-validation estimation method [198]. The leave one out method was used to validate the surrogate model.

Using the surrogate model and the relevant variables, a Monte-Carlo sampling method was used to evaluate an experimental design of 10000 simulations to estimate the capacity curve [143]. Then, using the probability distribution function (i.e., GEV, Gumbel, and Kernel), it was fitted based on the generated histogram of adequacy factors (i.e., the number of load increments that the structure can withstand without collapsing based on the acting load), which allowed to define the resistance curve, R. Figure 85 depicts the process for the results related to the S_1 damages. In (a), the Monte Carlo sampling performed on each variable is indicated, while (b) showcases the resulting histograms for each scour depth.

Noticeable differences between the histograms can be observed, which can be attributed to the number of experiments conducted. However, by adjusting the suggested Probability Density Functions, this issue can be overcome, allowing for a more accurate characterization of the data. Furthermore, it is evident from the histograms that as the scour depth increases, the bridge capacity is adversely affected. This explains the higher frequency of results falling within the range of 0 to 2.

The previously determined structural system resistance characterization is directly associated with the applied live load. In this sense, it results from the maximum applied load factor relative to the LM71 model. Therefore, the resistance curve multiplies the mean value of the PDF describing the live load, where its COV depends on the random variables that influence the resistance. Hence, the loading PDF's mean value should be defined as a unitary load factor. The associated COV was 15%, as recommended by Matos et al. [168]. Nevertheless, the uncertainty around the live loads should be obtained through monitoring data.

The reliability of the structure was evaluated by Equation (32), which is the limit state function. The variable G was introduced to UQlab, using the probabilistic distribution of both loading curve, S and resistance curve, R.

$$G = R - S$$

(32)
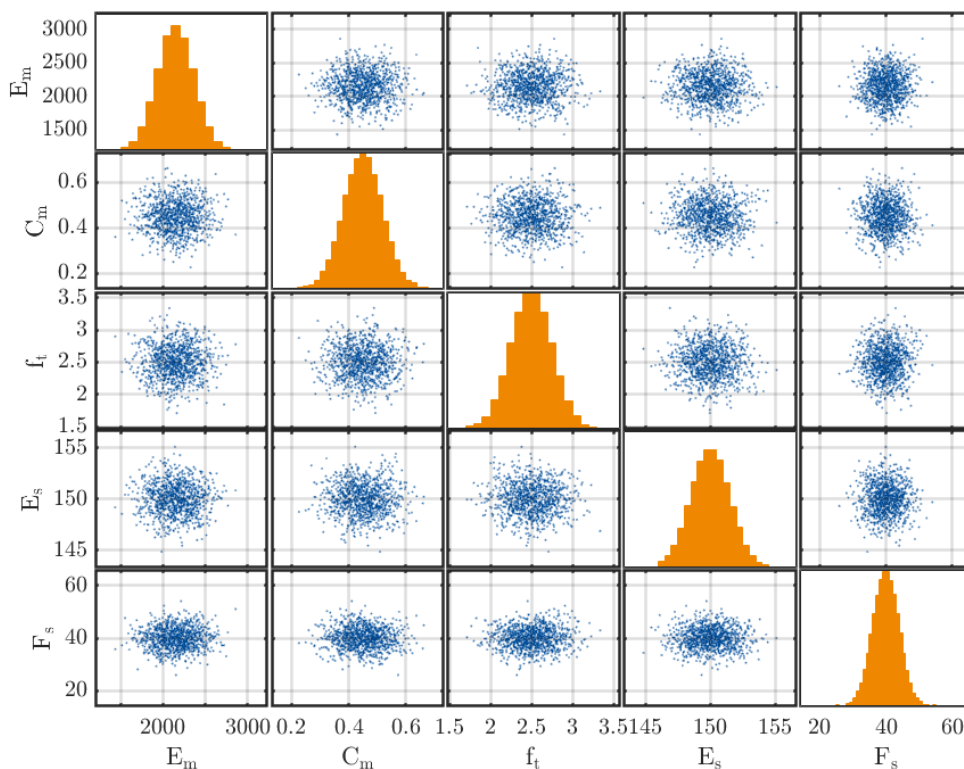
(a)
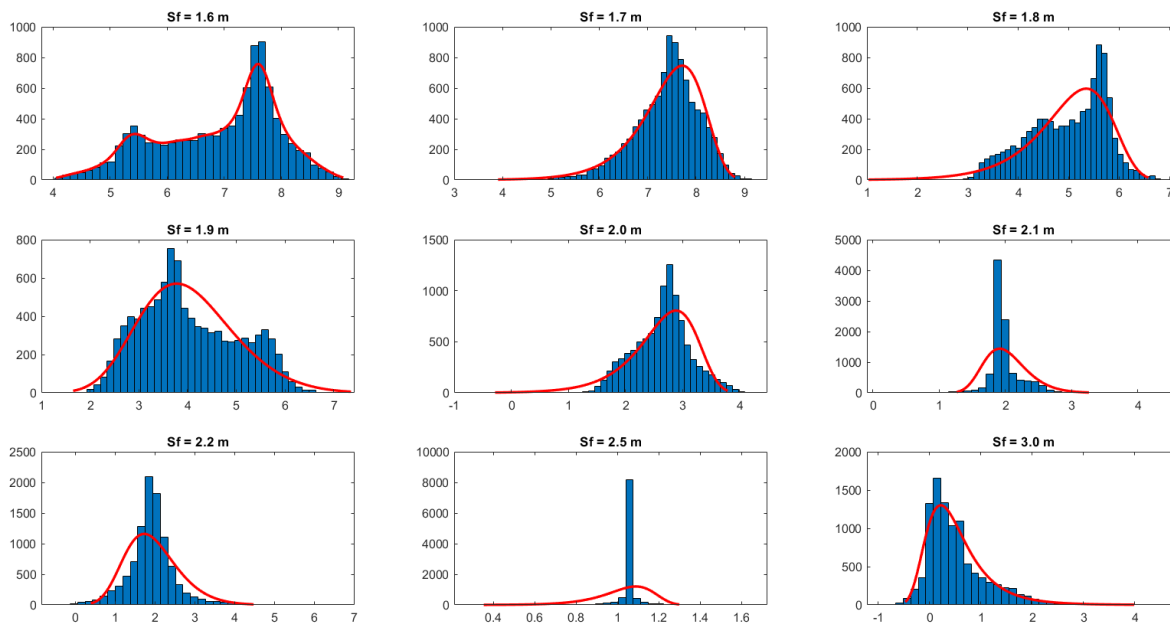
(b)

Figure 85 – Process for obtaining the capacity curve of a value of scour depth: (a) Monte Carlo sampling; and (b) fitting to a probability distribution function.

Additionally, model uncertainties for limit state models (defined by a Gaussian distribution of mean one and COV 15%) were also considered based on the recommendations of the Joint Committee on Structural Safety [170] model code, for shallow foundations' stability with homogeneous soil profiles. To obtain the reliability index of the structure for a given discharge value, traditional methods like MC may require numerous simulations to converge with a satisfactory level of accuracy. Therefore, subset simulation techniques were herein employed to overcome such limitations, by solving simpler reliability problems with intermediate thresholds [196]. Once the reliability analysis was completed, the failure probability and reliability index were obtained for each scour depth value (see Figure 86).

(a)   (b)
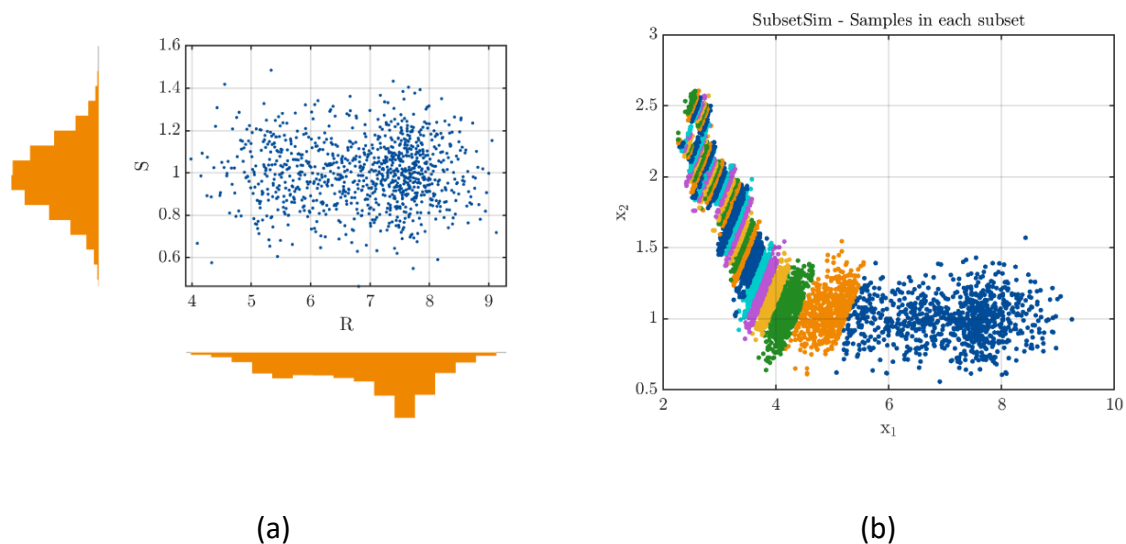
Figure 86 – Process to obtain failure probability: (a) starting sampling (model uncertainties not in the graph); and (b) subset simulation graphical process (where X_1 is S and X_2 is R).

Figure 87 shows the reliability index for different values of scour depths, in which it can be observed that the reliability decreases with each increment for both foundations studied. Finally, when compared with the target reliability (i.e., $\beta_{target} = 4.3$ corresponding to a failure probability below 10^{-5}) for structures with consequences involving high human and economic losses, according to NP 1990 [199], it may be concluded that the structure may not be within the safety levels when facing harsh scour conditions (i.e., reaching below the foundation).
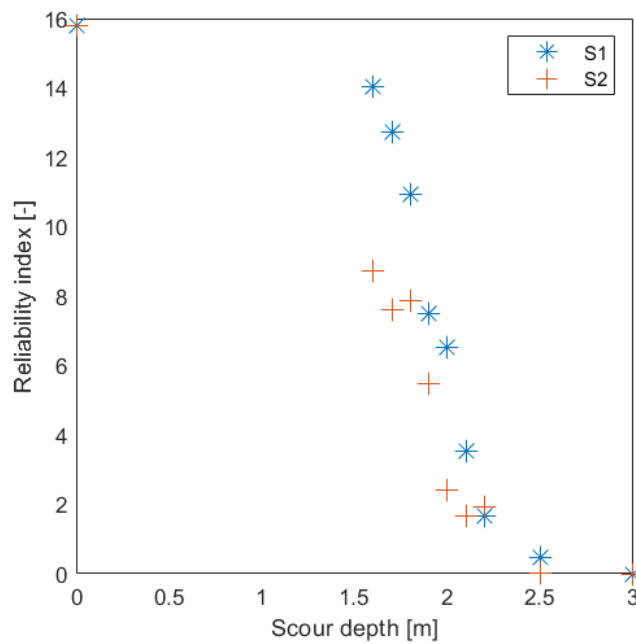
Figure 87 – Reliability index of the case study for each value of scour depth.

5.4.3 FRAGILITY ANALYSIS

A fragility function generally correlates a given hazard, represented by an intensity measure, with expected physical damage (e.g., collapse) using exceedance probability. Moreover, they are useful due to the possibility of introducing uncertainties in both capacity and demand, while also providing the reliability of a structure over a range of loads expressed commonly by a lognormal distribution [200]. Flood-related fragility curves can also assist the quality control strategies before, during, and after a flood event [201].

For the fragility curve that fits the failure probabilities previously found, a lognormal adjustment was performed. A script was employed to obtain the coefficients based on the Generalized linear model [202]. For this application, the generalized linear regression model was considered, in which the response (dependent variable) was expressed as a linear function of all the predictors (independent variables), as stated in [202]. Figure 88 presents the fragility curve fitted to a lognormal distribution where it can be observed that the capacity of the bridge decreases with each increment of the scour depth. As expected, it was found that for scour profiles where the scour depth does not erode the soil beneath the foundation

base; its influence on the structural response is minor, causing a slight decrease in the bridge reliability index of the masonry arch bridge is neglectable [156], [203].
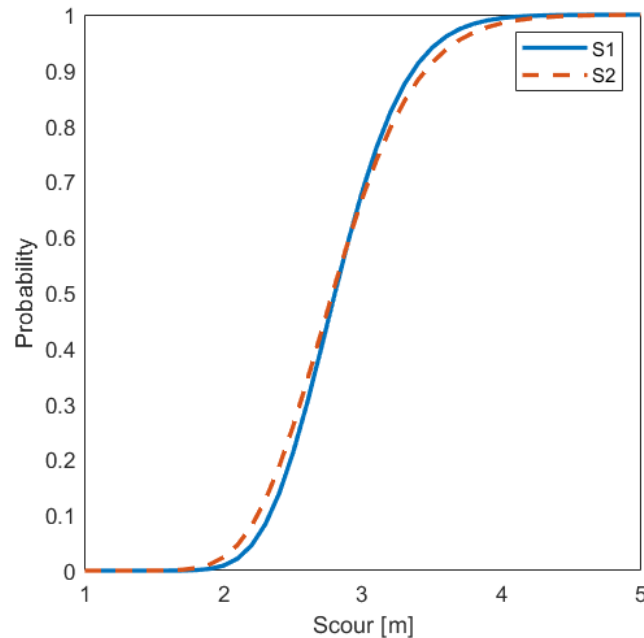
Figure 88 – Fragility curve for both foundations.

It can be observed a similar behavior of each of the foundations (S1 and S2) when subjected to local scouring, which was expected due to the bridge symmetry. Additionally, both fragility curves were created based on the failure modes described in subsection 5.3, where soil failure prevails only when the scour depth is over 2.5 meters, and the soil beneath the foundations has a limited loading capacity.

5.5 ROBUSTNESS ANALYSIS

A robustness assessment is implemented to finalize the framework applicable to the Leça bridge case study. Therefore, the robustness indicator was estimated using the methodology proposed in subsection 4.2. To define the hazard's magnitude, the proposed damage scenarios consider the maximum scour (S_d = 3 m) as 100% and the undamaged as 0%. This way, it is possible to implement the normalization of the already calculated reliability indices and their subsequent graphing (see Figure 89).
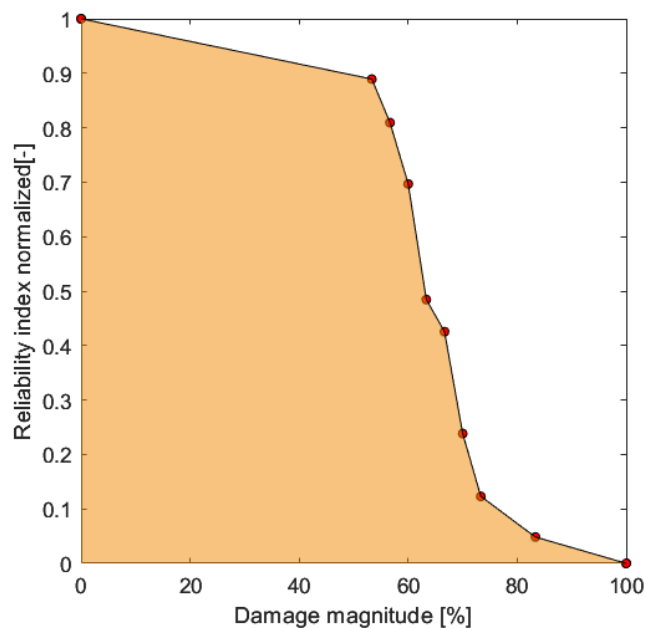
Figure 89 – Normalized reliability index considering scour magnitudes.

After normalizing the reliability indices, the robustness indicator can be estimated. Nevertheless, the discrete data available are higher than those executed in the practical example of section 4.2. In this sense, it is proposed to apply equation (x) using two different approaches: i) trapezoidal areas calculation; ii) fitting the data to a generalized linear model (GLM) and using the resulting function as $f(D)$. Figure 90 shows both graphical approaches.

(a)   (b)
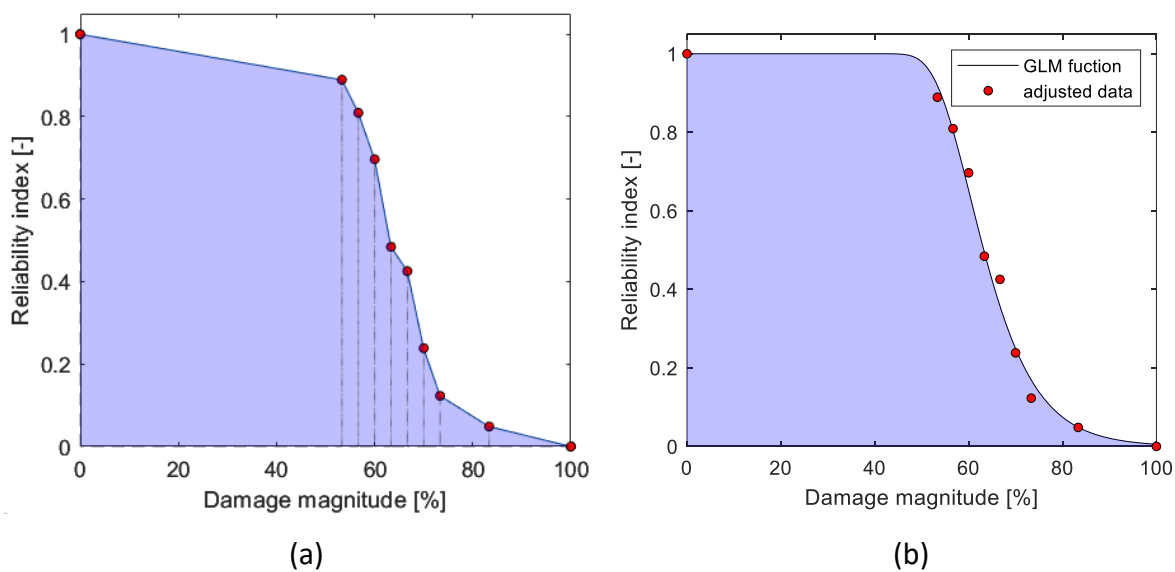
Figure 90 – Robustness indicator from normalized structural performance curve (a) trapezoid area of discrete data. (b) area of GLM fitting function.

The resulting $I_{R,D}$ for both approaches considering a damaging magnitude of 100%, was 62.18% and 64.79%, respectively, showing the high robustness against scour problems of the Leça river bridge. Therefore, although both estimations are alike, it is recommended to adjust the normalized data into a continuous function that can provide accurate outcomes.

5.6 FINAL REMARKS

Based on the obtained results, the following conclusions can be drawn:

Finite element modelling provides a good representation of the structure allowing, in combination with a dynamic calibration, to obtain a more detailed response of the structure. Nevertheless, due to the stochastic nature of the reliability analyses, the computational requirements may be too demanding. To overcome this, surrogate models with a sensitivity analysis provide a more efficient framework for the assessment of structures. Thus, the implementation into a network level for industrial purposes can be simplified.

Regarding the sensitivity analysis, the most relevant parameters regarding the failure mode are the mechanical parameters used for the constitutive model of the soil's weaker layers and masonry materials. Consequently, the common parameter is the elasticity modulus, i.e., stiffness, which are important for the soil-structure interaction.

For the fragility analysis, only the information where the soil removal affects the behavior of the structure, and its stability was considered. In other words, for values where the scour depth was below the foundation level. This explains the range in which the fragility curves were defined, i.e., scour depth higher than 1.5 m. The behavior of both foundations, when they were subject to scour, was not similar. This can be explained by the geometry difference between both piers and the loading location during the analysis. However, when the failure mechanism is located in the soil, it shows the same behavior due to its symmetry to transfer the loading into the ground. The bridge reliability decreased with each increment of the scour depth. Nevertheless, the loss of bearing capacity for values of the scour depth lower than the foundation level was slight when compared with higher values. Moreover, a decrease in the reliability index below the safety levels was identified for the cases in which most of the values obtained for scour depth were below the foundation height.
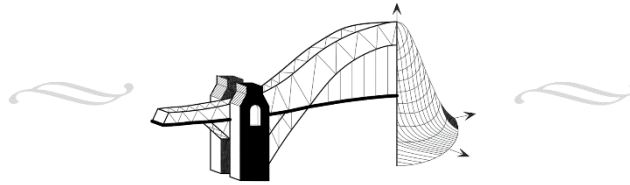
CONCLUSIONS AND FUTURE WORKS

6.1 CONCLUSIONS

This thesis focused on the proposal and implementation of a framework for railway bridge assessment. The main idea was to prioritize simplifying the data collection and the calculations effort, intending to focus on specific complexities of the structure analysis. Therefore, the framework was divided into four workstreams for its successful implementation. The first one is related to the hazard study. Although for this thesis, it was determined that flooding and, consequently, scour was the leading cause of bridge collapsing worldwide. Then, it was decided to pay attention to its implications and assessment procedures. At the industry level for structure management and design, it was found that simple techniques based on empirical formulas are still used and accepted. In this sense, it was determined to take these processes further by implementing machine learning algorithms to analyze databases. In this sense, it was decided to take these processes further by implementing machine learning algorithms to analyze databases. The critical point for using these algorithms was considering data related to climate change. In this way, it was aimed to take this phenomenon into account without resorting to complex statistical procedures or obtaining specific data to execute them. This way, it was possible to implement a neural network considering rainfall projections in the studied region that was validated and implemented in hydraulic models. The second workstream studies the causes of the structure's failure due to the studied hazard. Therefore,

an overview was made of structural and geotechnical problems and their interactions considering the flooding hydraulic effects.

Nevertheless, many limitations were found due to the broad spectrum of found phenomena, additionally, the number of variables for each specific case, for example, the type of structure and its foundation, topographic characteristics, and soil type. For this reason, an attempt was made to cover the theoretical basis of the problem. Finally, it was applied to practical case studies, which can serve as a reference for implementing this current work in the proposed framework.

The third workstream is related to the finite element modeling of structures and was the primary basis for developing the fourth workstream. This methodology aimed to present a modeling approach in several practical cases using different 2D and 3D elements of the DIANA FEA software allowing a high degree of detail into the non-linear analysis and the considered uncertainties. Finally, the fourth workstream is related to the calculation of structural reliability and its robustness against the studied hazard. Therefore, various surrogate model tools were used to optimize all calculation processes to make the framework viable for application in the industry.

The methodology tested in this study applies a reliability technique (surrogate modeling) in a 3D finite element model. The study shows that it is possible to perform an analysis of complex models without compromising accuracy in a reasonable time frame. This means that the methodology can be applied to a network scale when the accuracy of scour damage needs to be determined.

This has several real-world implications, particularly in civil engineering and infrastructure management. For example, the ability to analyze complex network-scale models accurately and efficiently can help identify areas of potential scour damage in bridges and other structures, which can then be addressed to improve safety and reduce the risk of failure. Additionally, the methodology can be used to optimize the design of new structures and improve the resilience of existing structures, which can have significant implications for the field of civil engineering and infrastructure management. Overall, this methodology can

improve the reliability and safety of transportation networks while reducing maintenance and repair costs.

The study has some limitations that may have influenced the results. One limitation is that certain sources of uncertainty, such as bridge geometry and loading, were not considered. This means that the model may not be able to account for all possible variations in these parameters and may not be applicable to all types of bridges.

Another limitation is that the calibration of the model is based on dynamic data from only one experimental campaign. The use of real-time data, collected over a longer period of time, could improve the model by providing more data points and a wider range of conditions to consider. In addition, the study may not be able to capture the full dynamic response of the bridge and provide enough information to design bridges for different scenarios. It is important to note that these limitations may affect the accuracy and generalizability of the results, and that further research is needed to address these issues and improve the model.

Implementing the improved accuracy and efficiency of the methodology into practice can help reduce the risk of structural failures and minimize the consequences, such as human lives or economic losses. In the case of bridges, for example, the methodology can be used to predict structural problems or vulnerabilities to natural hazards such as earthquakes or floods and prevent disasters.

An example of how the results could be put into practice is regular monitoring of the structural condition of critical infrastructure such as bridges, dams, and buildings. This can help identify potential problems early and take appropriate action to prevent catastrophic failure.

Another example of implementation is for contractors and municipalities to use the methodology when designing and maintaining new structures to ensure they are more resilient to natural hazards and reduce the risk of failure.

Potential benefits of implementing the methodology include reducing the risk of structural failure, improving safety, and reducing economic losses caused by structural failure.

6.2 FUTURE WORKS

The methodology developed covered the basics for analyzing damage caused by scour effects on bridges improving computational effort and timing. However, the development of this work left several aspects that could be improved and considered for future developments.

• Use of emerging machine learning technologies, such as deep learning, to improve the accuracy and efficiency of structural management and quality control.

• Use image recognition and processing techniques to extract and analyze data from structural inspections and update numerical models and reliability algorithms.

• Explore the use of natural language processing (NLP) to analyze and extract information from unstructured data sources such as inspection reports and maintenance logs.

• Investigate the potential benefits of incorporating virtual and augmented reality technologies into structural inspection and maintenance tasks.

• Investigate the scalability and practicality of implementing the machine learning-based approach in real industrial environments.

• Investigate the feasibility of using the approach to predict structural failure and develop proactive maintenance strategies.

• Investigate the integration of the approach with other technologies such as IoT and sensor networks to collect and analyze structural data in real-time.

• Investigate the potential use of the approach to optimize the design of new structures.

REFERENCES

[1]   M. Haltuf, "Shift2Rail JU from Member State's Point of View," in *Transportation Research Procedia*, 2016. doi: 10.1016/j.trpro.2016.05.148.

[2]   Technical Strategy Leadership Group, "The Rail Technical Strategy 2012," 2012.

[3]   I. Olofsson *et al.*, "Assessment of European railway bridges for future traffic demands and longer lives – EC project 'Sustainable Bridges,'" *Structure and Infrastructure Engineering*, vol. 1, no. 2, pp. 93–100, 2005, doi: 10.1080/15732470412331289396.

[4]   K. Douben, "CHARACTERISTICS OF RIVER FLOODS AND FLOODING : A GLOBAL OVERVIEW, 1985–2003," vol. 21, pp. 25–27, 2006, doi: 10.1002/ird.239.

[5]   D. Proske, "Comparison of Bridge Collapse Frequencies with Failure Probabilities Comparison of Bridge Collapse Frequencies with Failure Probabilities," no. March, 2018.

[6]   W. Cook, "Bridge Failure Rates, Consequences, and Predictive Trends," *All Graduate Theses and Dissertations*, 2014.

[7]   I. E. Harik, A. M. Shaaban, H. Gesund, G. Y. Valli, and S. T. Wang, "United states bridge failures, 1951-1988," *Journal of Performance of Constructed Facilities*, 1990, doi: 10.1061/(ASCE)0887-3828(1990)4:4(272).

[8]   S. B. Mohan and S. Sharma, "Status of bridge failures in the United States (1800-2009)," 2011.

[9]   K. Wardhana, F. C. Hadipriono, and F. Asce, "Analysis of Recent Bridge Failures in the United States," no. August, pp. 144–150, 2003.

[10]   G. C. Lee, S. Mohan, C. Huang, and B. N. Fard, *A study of US bridge failures (1980-2012)*. MCEER, 2013.

[11]   M. I. Hersi, "Analysis of Bridge Failures in the United States (2000-2008)." The Ohio State University, 2009.

[12]   J. Scheer, *Failed bridges: case studies, causes and consequences*. John Wiley & Sons, 2011.

[13]   D. Imhof, "Risk assessment of existing bridge structures." University of Cambridge, 2004.

[14]   M. R. TARICSKA, "AN ANALYSIS OF RECENT BRIDGE FAILURES IN THE UNITED STATES (2000-2012)," 2014. doi: 10.1192/bjp.205.1.76a.

[15]   D. SMITH, "BRIDGE FAILURES.," *Proceedings of the Institution of Civil Engineers*, 1976, doi: 10.1680/iicep.1976.3389.

[16]   M. V. Biezma and F. Schanack, "Collapse of steel bridges," *Journal of Performance of Constructed Facilities*, vol. 21, no. 5, pp. 398–405, 2007, doi: 10.1061/(ASCE)0887-3828(2007)21:5(398).

[17]   L. Deng, W. Wang, and Y. Yu, "State-of-The-Art Review on the Causes and Mechanisms of Bridge Collapse," *Journal of Performance of Constructed Facilities*, vol. 30, no. 2, pp. 1–13, 2016, doi: 10.1061/(ASCE)CF.1943-5509.0000731.

[18]   Z. Fu, B. Ji, M. Cheng, and H. Maeno, "Statistical analysis of cause of bridge collapse in China," *Forensic Engineering 2012: Gateway to a Better Tomorrow - Proceedings of the 6th Congress on Forensic Engineering*, pp. 75–83, 2013, doi: 10.1061/9780784412640.009.

[19]   I. Olofsson *et al.*, "Assessment of European railway bridges for future traffic demands and longer lives – EC project 'Sustainable Bridges,'" *Structure and Infrastructure Engineering*, vol. 1, no. 2, pp. 93–100, 2005, doi: 10.1080/15732470412331289396.

[20]   D. Proske, "Comparison of Bridge Collapse Frequencies with Failure Probabilities," in *Proceedings of the 15th International Probabilistic Workshop*, 2017, pp. 15–23.

[21]   M. V. Biezma and F. Schanack, "Collapse of steel bridges," *Journal of Performance of Constructed Facilities*, vol. 21, no. 5, pp. 398–405, 2007.

[22]   K. Douben, "Characteristics of river floods and flooding: a global overview, 1985–2003," *Irrigation and Drainage: The journal of the International Commission on Irrigation and Drainage*, vol. 55, no. S1, pp. S9–S21, 2006.

[23]   D. Y. Yang and D. M. Frangopol, "Risk-informed bridge ranking at project and network levels," *Journal of Infrastructure Systems*, vol. 24, no. 3, p. 4018018, 2018.

[24]   A. M. Bento, A. Gomes, T. Viseu, L. Couto, and J. P. Pêgo, "Risk-based methodology for scour analysis at bridge foundations," *Eng Struct*, vol. 223, p. 111115, 2020.

[25]   R. Barber, "MMO Climate Change Adaptation Report," p. 20, 2015.

[26]   C. B. Field, V. Barros, T. F. Stocker, and Q. Dahe, *Managing the risks of extreme events and disasters to advance climate change adaptation: special report of the intergovernmental panel on climate change*. Cambridge University Press, 2012.

[27]   R. W. Katz, "Towards a statistical paradigm for climate change," *Clim. Res*, vol. 2, no. 1, pp. 167–175, 1993.

[28]   B. Imam, *Climate Change Impact for Bridges Subjected to Scour and Corrosion*. Elsevier Inc., 2019. doi: 10.1016/b978-0-12-816782-3.00006-1.

[29]   T. F. Stocker *et al.*, "Climate change 2013: The physical science basis." Cambridge University Press Cambridge, 2013.

[30]   R. Tanty and T. S. Desmukh, "Application of artificial neural network in hydrology—A review," *Int. J. Eng. Technol. Res*, vol. 4, pp. 184–188, 2015.

[31]   L. Yang, J. Li, H. Sun, Y. Guo, and B. A. Engel, "Calculation of nonstationary flood return period considering historical extraordinary flood events," *J Flood Risk Manag*, vol. 12, no. 2, pp. 1–10, 2019, doi: 10.1111/jfr3.12463.

[32]   S. E. Debele, W. G. Strupczewski, and E. Bogdanowicz, "A comparison of three approaches to non-stationary flood frequency analysis," *Acta Geophysica*, vol. 65, no. 4, pp. 863–883, 2017, doi: 10.1007/s11600-017-0071-4.

[33] W. G. Strupczewski and W. Feluch, "Flood frequency analysis under non-stationarity," *Geogr Pol*, vol. 71, pp. 19–34, 1998.

[34] K. Kochanek, W. G. Strupczewski, E. Bogdanowicz, W. Feluch, and I. Markiewicz, "Application of a hybrid approach in nonstationary flood frequency analysis–a Polish perspective," *Natural Hazards and Earth System Sciences Discussions*, vol. 1, no. 5, pp. 6001–6024, 2013.

[35] R. A. Rigby and D. M. Stasinopoulos, "Generalized additive models for location, scale and shape," *J R Stat Soc Ser C Appl Stat*, vol. 54, no. 3, pp. 507–554, 2005.

[36] Z.-M. Liang, Y.-M. Hu, and J. Wang, "Advances in hydrological frequency analysis of non-stationary time series," *Advances in Water Science*, vol. 22, no. 6, pp. 864–871, 2011.

[37] L. Zhao, C. Liu, L. Sobkowiak, X. Wu, and J. Liu, "A review of underlying surface parameterization methods in hydrologic models," *Journal of Geographical Sciences*, vol. 29, no. 6, pp. 1039–1060, 2019.

[38] E. Paquet, "A distributed application of the SCHADEX stochastic method for extreme flood estimation," 2019.

[39] P. Valent, R. Výleta, J. Szolgay, and E. Paquet, "Stochastic Flood Frequency Analysis Using the SCHADEX Method in Slovakia," in *EGU General Assembly Conference Abstracts*, 2014, vol. 16.

[40] P. Brigode, P. Bernardara, E. Paquet, J. Gailhard, P. Ribstein, and R. Merz, "Complete application of the SCHADEX method on an Austrian catchment: Extreme flood estimation on the Kamp river," in *Geophys. Res. Abstr*, 2011, vol. 14, p. 6771.

[41] G. A. Holemba and T. Matsumoto, "Flood-induced Bridge Failures in Papua New Guinea," *MATEC Web of Conferences*, vol. 258, p. 03014, 2019, doi: 10.1051/matecconf/201925803014.

[42] C. Cunnane, "Methods and merits of regional flood frequency analysis," *J Hydrol (Amst)*, vol. 100, no. 1–3, pp. 269–290, 1988, doi: 10.1016/0022-1694(88)90188-6.

[43] S. M. E. C. (Australia), P. N. Guinea., and B. of W. Resources., *Papua New Guinea flood estimation manual*. [Boroko?]: [Papua New Guinea, Dept. of Environment and Conservation, Bureau of Water Resources], 1990.

[44] E. Velhas, "A bacia hidrográfica do Rio Leça: estudo hidroclimatológico," *Geografia: Revista da Faculdade de Letras da Universidade do Porto*, vol. 7, 1991.

[45] A. C. de Lencastre and F. M. Franco, *Lições de hidrologia*. Universidade Nova de Lisboa, 1984.

[46] A. C. Quintela, "Curso Internacional de Hidrologia Operativa, vol. 2," *Direcçao-Geral dos Recursos e Aproveitamento Hidráulicos*, 1984.

[47] P. Témez, "JR 1978. Tiempo de concentración," *Cálculo Hidrometeorológico de Caudales Máximos en Pequeñas Cuencas Naturales. Dirección General de Carreteras. Ministerio de Obras Públicas y Urbanismo. Madrid, España. pp*, pp. 79–91.

[48] D. Gorissen DIRKGORISSEN, U. Ivo Couckuyt, P. Demeester, T. Dhaene TOMDHAENE, and K. Crombecq KARELCROMBECQ, "A Surrogate Modeling and Adaptive Sampling Toolbox for Computer Based Design," *Journal of Machine Learning Research*, 2010.

[49] G. E. P. Box and K. B. Wilson, "On the experimental attainment of optimum conditions," *Journal of the Royal Statistical Society: Series B (Methodological)*, vol. 13, no. 1, pp. 1–38, 1951.

[50] B. J. Bichon, "Efficient surrogate modeling for reliability analysis and design." Vanderbilt University, 2010.

[51] J. Ghosh, J. E. Padgett, and L. Dueñas-Osorio, "Surrogate modeling and failure surface visualization for efficient seismic vulnerability assessment of highway bridges," *Probabilistic Engineering Mechanics*, 2013, doi: 10.1016/j.probengmech.2013.09.003.

[52] N. Bakhary, H. Hao, and A. J. Deeks, "Damage detection using artificial neural network with consideration of uncertainties," *Eng Struct*, 2007, doi: 10.1016/j.engstruct.2007.01.013.

[53]   T. L. LEE, D. S. JENG, G. H. ZHANG, and J. H. HONG, "Neural network modeling for estimation of scour depth around bridge piers," *Journal of Hydrodynamics*, 2007, doi: 10.1016/S1001-6058(07)60073-0.

[54]   S.-U. Choi and S. Cheong, "Prediction of local scour around bridge piers using artificial neural networks," *JAWRA Journal of the American Water Resources Association*, 2006, doi: 10.1111/j.1752-1688.2006.tb03852.x.

[55]   W. T. Kearney, "Using genetic algorithms to evolve artificial neural networks," 2016. doi: 10.4156/jcit.vol5.issue8.6.

[56]   P. Gonçalves, I. Marafuz, and A. Gomes, "Flood hazard, Santa Cruz do Bispo Sector, Leça River, Portugal: A methodological contribution to improve land use planning," *J Maps*, vol. 11, no. 5, pp. 760–771, 2015.

[57]   L. Soares, A. Araújo, and A. A. Gomes, "Contexto geográfico do território do Leça," *O Rio da memória: Arqueologia do território do Leça*, 2011.

[58]   Sistema Nacional de Informação de Recursos Hídricos, "Informação sobre os pontos de monitorização.," 2021. https://snirh.apambiente.pt/

[59]   The World Bank Group, "The Climate Change Knowledge Product," 2021. https://climateknowledgeportal.worldbank.org

[60]   J. Lynn and N. Peeva, "Communications in the IPCC's Sixth Assessment Report cycle," *Clim Change*, vol. 169, no. 1–2, Nov. 2021, doi: 10.1007/S10584-021-03233-7.

[61]   R. J. Aristizabal, "Estimating the parameters of the three-parameter lognormal distribution," 2012.

[62]   N. Millington, S. Das, and S. P. Simonovic, "The comparison of GEV, log-Pearson type 3 and Gumbel distributions in the Upper Thames River watershed under global climate models," 2011.

[63]   J. R. M. Hosking and J. R. Wallis, *Regional Frequency Analysis: An Approach Based on L-Moments*. Cambridge: Cambridge University Press, 1997. doi: DOI: 10.1017/CBO9780511529443.

[64]   T. A. Solaiman, "Uncertainty estimation of extreme precipitations under climate change: A non-parametric approach," 2011.

[65]   A. M. Bento, A. Gomes, J. P. Pêgo, T. Viseu, and L. Couto, "Improved assessment of maximum streamflow risk management of hydraulic infrastructures. A case study.," *International Journal of River Basin Management*, no. just-accepted, pp. 1–39, 2021.

[66]   K. Okoli, K. Breinl, L. Brandimarte, A. Botto, E. Volpi, and G. Di Baldassarre, "Model averaging versus model selection: estimating design floods with uncertain river flow data," *Hydrological Sciences Journal*, vol. 63, no. 13–14, pp. 1913–1926, 2018.

[67]   G. W. Brunner, "HEC-RAS river analysis system. Hydraulic reference manual. Version 5.0.," 2016.

[68]   R. Hajdin, M. Kusar, S. Masovic, P. Linneberg, J. Amado, and N. Tanasić, "Establishment of quality control plan - Cost Action TU1406: WG," 2018. doi: 10.13140/RG.2.2.28730.03526.

[69]   B. Solan, A. NOWROOZPOUR, P. Clopper, C. Watters, and R. Ettema, "SCOUR-INDUCED FAILURE OF MASONRY ARCH BRIDGES: CAUSES AND COUNTERMEASURES," in *E-proceedings of the 38th IAHR World Congress*, 2019.

[70]   J. Heyman, *The Mansonry Arch*. 1982.

[71]   G. A. Drosopoulos, G. E. Stavroulakis, and C. V Massalas, "Limit analysis of a single span masonry bridge with unilateral frictional contact interfaces," *Eng Struct*, vol. 28, no. 13, pp. 1864–1873, 2006.

[72]   A. Orduña and P. B. Lourenço, "Three-dimensional limit analysis of rigid blocks assemblages. Part I: Torsion failure on frictional interfaces and limit analysis formulation," *Int J Solids Struct*, vol. 42, no. 18–19, pp. 5140–5160, 2005.

[73]   M. Gilbert, "Limit analysis applied to masonry arch bridges: state-of-the-art and recent developments," in *5th International arch bridges conference*, 2007, pp. 13–28.

[74]   R. K. Livesley, "A computational model for the limit analysis of three-dimensional masonry structures," *Meccanica*, vol. 27, no. 3, pp. 161–172, 1992.

[75]   LimitState Ltd, *LimitState:RING Manual VERSION 3.2.c*. Sheffield, United Kingdom, 2020.

[76]   T. M. Browne, T. J. Collins, M. J. Garlich, and J. E. ; O'Leary, "FHWA-NHI-10-027:Underwater Bridge Inspection," 2010.

[77]   P. Zampieri, M. A. Zanini, F. Faleschini, L. Hofer, and C. Pellegrino, "Failure analysis of masonry arch bridges subject to local pier scour," *Eng Fail Anal*, vol. 79, no. January, pp. 371–384, 2017, doi: 10.1016/j.engfailanal.2017.05.028.

[78]   J. A. and N. T. R. Hajdin, M. Kušar, S. Mašović, P. Linneberg, "WG3 Technical Report – Establishment of a Quality Control Plan.," 2018.

[79]   Aashto, *AASHTO LRFD Bridge Design Specifications*. 2010. doi: 10.1111/febs.12237.

[80]   M. E. G. Alvarez, *Socavacion en puentes*. 2016.

[81]   B. W. Melville and S. E. Coleman, *Bridge scour*. Water Resources Publication, 2000.

[82]   B. W. Melville, "Pier and abutment scour: integrated approach," *Journal of hydraulic Engineering*, vol. 123, no. 2, pp. 125–136, 1997.

[83]   E. V Richardson and S. R. Davis, "Evaluating scour at bridges (HEC-18)," *US Department of Transportation, Federal Highway Administration, Colorado, 4th edn. FHWA NHI*, p. 1, 2001.

[84]   D. M. Sheppard and W. Miller Jr, "Live-bed local pier scour experiments," *Journal of Hydraulic Engineering*, vol. 132, no. 7, pp. 635–642, 2006.

[85]   D. M. Sheppard, B. Melville, and H. Demir, "Evaluation of existing equations for local scour at bridge piers," *Journal of Hydraulic Engineering*, vol. 140, no. 1, pp. 14–23, 2013.

[86]   L. A. Arneson, L. W. Zevenbergen, P. F. Lagasse, and P. E. Clopper, "Evaluating scour at bridges–Fifth Edition, Federal Highway Administration Hydraulic Engineering Circular No. 18," FHWA-HIF-12-003, FHWA, Washington, DC, 2012.

[87]   E. M. Laursen, "Scour at bridge crossings: Journal of the Hydraulics Division, American Society of Civil Engineers, v. 86, no." HY2, 1960.

[88]   H.-K. Liu, F. M. Chang, and M. M. Skinner, "Effect of bridge constriction on scour and backwater," Colorado State University. Libraries, 1961.

[89]   E. M. Laursen and A. Toch, *Scour around bridge piers and abutments*, vol. 4. Iowa Highway Research Board Ames, IA, 1956.

[90]   D. C. Froehlich, "Local scour at bridge abutments," in *Hydraulic Engineering*, 1989, pp. 13–18.

[91]   B. W. Melville, "Local scour at bridge abutments," *Journal of Hydraulic Engineering*, vol. 118, no. 4, pp. 615–631, 1992.

[92]   L. W. Zevenbergen, L. A. Arneson, J. H. Hunt, and A. C. Miller, "Hydraulic design of safe bridges," United States. Federal Highway Administration, 2012.

[93]   S. A. I. Global, "Bridge Design (AS 5100-2004)," *Standards Australia*, 2004.

[94]   M. Sassu, L. Giresini, and M. L. Puppio, "Failure scenarios of small bridges in case of extreme rainstorms," *Sustain Resilient Infrastruct*, vol. 2, no. 3, pp. 108–116, 2017.

[95]   G. B. Crosta and P. Frattini, "Rainfall-induced landslides and debris flows," *Hydrological Processes: An International Journal*, vol. 22, no. 4, pp. 473–477, 2008.

[96]   D. S. Chang and L. M. Zhang, "Simulation of the erosion process of landslide dams due to overtopping considering variations in soil erodibility along depth," *Natural Hazards and Earth System Sciences*, vol. 10, no. 4, pp. 933–946, 2010.

[97]   D. S. Chang, L. M. Zhang, Y. Xu, and R. Q. Huang, "Field testing of erodibility of two landslide dams triggered by the 12 May Wenchuan earthquake," *Landslides*, vol. 8, no. 3, pp. 321–332, 2011.

[98]   G. W. Annandale, *Scour technology*. McGraw-Hill, 2006.

[99]   K. Kerenyi, T. Sofu, and J. Guo, "Hydrodynamic forces on inundated bridge decks," 2009.

[100]   T. E. Fenske, C. J. Apelt, and A. C. Parola, "Debris forces and impacts on highway bridges," *Proceedings, International Association for Bridge and Structural Engineering*, pp. 1017–1022, 1995.

[101]   ISRM, "Basic geotechnical description of rock masses. ISRM Commission on the Classification of Rocks and Rock Masses," *Int. J. Rock Mech. Mining Sci. Geom. Abst.*, vol. 18, pp. 85–110, 1981.

[102]   W. R. Dearman, "Description and classification of weathered rocks for engineering purposes: the background to the BS5930: 1981 proposals," *Quarterly Journal of Engineering Geology and Hydrogeology*, vol. 28, no. 3, pp. 267–276, 1995.

[103]   M. Heidari, A. A. Momeni, and F. Naseri, "New weathering classifications for granitic rocks based on geomechanical parameters," *Eng Geol*, vol. 166, pp. 65–73, Nov. 2013, doi: 10.1016/J.ENGGEO.2013.08.007.

[104]   A. J. P. V. da Fonseca, "Geomecânica dos solos residuais do granito do Porto: Critérios para dimensionamento de fundações directas," 1996.

[105]   A. Viana da Fonseca, M. Matos Fernandes, A. S. Cardoso, and J. Barreiros Martins, "Portuguese experience on geotechnical characterization of residual soils from granite," in *International conference on soil mechanics and foundation engineering*, 1994, pp. 377–380.

[106]   C. Lin, J. Han, C. Bennett, and R. L. Parsons, "Case History Analysis of Bridge Failures due to Scour," pp. 204–216.

[107]   A. Alencar, R. Galindo, and C. Olalla Marañón, "Assessment of the bearing capacity of bridge foundation on rock masses," *Applied Sciences*, vol. 11, no. 24, p. 12068, 2021.

[108]   K. Terzaghi, "Stress conditions for failure in soils," *Theoretical Soil Mechanics; John Wiley and Sons: New York, NY, USA*, pp. 7–11, 1943.

[109] G. G. Meyerhof, "The ultimate bearing capacity of foudations," *Geotechnique*, vol. 2, no. 4, pp. 301–332, 1951.

[110] S. W. Sloan, "Lower bound limit analysis using finite elements and linear programming," *Int J Numer Anal Methods Geomech*, vol. 12, no. 1, pp. 61–77, 1988.

[111] S. W. Sloan, "Upper bound limit analysis using finite elements and linear programming," *Int J Numer Anal Methods Geomech*, vol. 13, no. 3, pp. 263–282, 1989.

[112] D. v Griffiths, "Computation of bearing capacity factors using finite elements," *Geotechnique*, vol. 32, no. 3, pp. 195–202, 1982.

[113] M. A. Millán, R. Galindo, and A. Alencar, "Application of discontinuity layout optimization method to bearing capacity of shallow foundations on rock masses," *ZAMM-Journal of Applied Mathematics and Mechanics/Zeitschrift für Angewandte Mathematik und Mechanik*, vol. 101, no. 10, p. e201900192, 2021.

[114] R. S. Merifield, A. v Lyamin, and S. W. Sloan, "Limit analysis solutions for the bearing capacity of rock masses using the generalised Hoek–Brown criterion," *International Journal of Rock Mechanics and Mining Sciences*, vol. 43, no. 6, pp. 920–937, 2006.

[115] M. A. Millán, R. Galindo, and A. Alencar, "Application of artificial neural networks for predicting the bearing capacity of shallow foundations on rock masses," *Rock Mech Rock Eng*, vol. 54, no. 9, pp. 5071–5094, 2021.

[116] N. Dudek, "Pile group settlement analysis on the basis of Static Load Test," in *E3S Web of Conferences*, 2019, vol. 97, p. 4031.

[117] D. M. NAVFAC, "7.2 (1984): Foundation and Earth Structures," *US Department of the Navy*.

[118] P. Koudelka, "SIMILARITY OF BEARING CAPACITY OF BORED PILES ACCORDING TO ČSN 73 1002".

[119] B. S. EN, "Eurocode 7: geotechnical design–Part 1: general rules," *British Standards: London, UK*, 2004.

[120] prEN 1991-7, *Eurocode 1: Actions on Structures: Part 1-7: General actions - Accidental Actions*. 2003.

[121] FIB, "federation international du béton: Model Code for Concrete Structures," 2010.

[122] M. Ghosn *et al.*, "Performance indicators for structural systems and infrastructure networks," *Journal of Structural Engineering*, vol. 142, no. 9, p. F4016003, 2016.

[123] D. M. Frangopol and J. P. Curley, "Effects of damage and redundancy on structural reliability," *Journal of structural engineering*, vol. 113, no. 7, pp. 1533–1549, 1987.

[124] F. Biondini and S. Restelli, "Damage propagation and structural robustness," in *Life-Cycle Civil Engineering: Proceedings of the International Symposium on Life-Cycle Civil Engineering, IALCCE'08, Held in Varenna, Lake Como, Italy on June 11-14 2008*, 2008, p. 131.

[125] U. Starossek and M. Haberland, "Measures of structural robustness—Requirements and applications," in *Structures Congress 2008: Crossing Borders*, 2008, pp. 1–10.

[126] N. C. Lind, "A measure of vulnerability and damage tolerance," *Reliab Eng Syst Saf*, vol. 48, no. 1, pp. 1–6, 1995.

[127] M. Ghosn and F. Moses, *Redundancy in highway bridge superstructures*, vol. 406. Transportation Research Board, 1998.

[128] A. S. Nowak and K. R. Collins, *Reliability of structures*. CRC press, 2012.

[129] O. Ditlevsen and H. O. Madsen, *Structural reliability methods*, vol. 178. Wiley New York, 1996.

[130] M. Lemaire, *Structural reliability*. John Wiley & Sons, 2013.

[131] R. E. Melchers and A. T. Beck, *Structural reliability analysis and prediction*. John wiley & sons, 2018.

[132] H. A. M. and L. N. C., "Exact and Invariant Second-Moment Code Format," *Journal of the Engineering Mechanics Division*, vol. 100, no. 1, pp. 111–121, Feb. 1974, doi: 10.1061/JMCEA3.0001848.

[133] R. Rackwitz and B. Flessler, "Structural reliability under combined random load sequences," *Comput Struct*, vol. 9, no. 5, pp. 489–494, 1978, doi: https://doi.org/10.1016/0045-7949(78)90046-9.

[134] A. Haldar and S. Mahadevan, *Probability, reliability, and statistical methods in engineering design*. John Wiley & Sons Incorporated, 2000.

[135] B. M. Ayyub and R. H. Mccuen, "Simulation-based reliability methods," in *Probabilistic structural mechanics handbook*, Springer, 1995, pp. 53–69.

[136] S.-K. Au and J. L. Beck, "Estimation of small failure probabilities in high dimensions by subset simulation," *Probabilistic Engineering Mechanics*, vol. 16, no. 4, pp. 263–277, 2001, doi: https://doi.org/10.1016/S0266-8920(01)00019-4.

[137] R. E. Melchers, "Radial importance sampling for structural reliability," *J Eng Mech*, vol. 116, no. 1, pp. 189–203, 1990.

[138] P. Bjerager, "Probability integration by directional simulation," *J Eng Mech*, vol. 114, no. 8, pp. 1285–1302, 1988.

[139] P. S. Koutsourelakis, H. J. Pradlwarter, and G. I. Schuëller, "Reliability of structures in high dimensions, part I: algorithms and applications," *Probabilistic Engineering Mechanics*, vol. 19, no. 4, pp. 409–417, 2004, doi: https://doi.org/10.1016/j.probengmech.2004.05.001.

[140] H. J. Pradlwarter, G. I. Schuëller, P. S. Koutsourelakis, and D. C. Charmpis, "Application of line sampling simulation method to reliability benchmark problems," *Structural Safety*, vol. 29, no. 3, pp. 208–221, 2007, doi: https://doi.org/10.1016/j.strusafe.2006.07.009.

[141] J. Nie and B. R. Ellingwood, "A new directional simulation method for system reliability. Part II: application of neural networks," *Probabilistic Engineering Mechanics*, vol. 19, no. 4, pp. 437–447, 2004, doi: https://doi.org/10.1016/j.probengmech.2004.03.005.

[142] E. Zio, "Monte carlo simulation: The method," in *The Monte Carlo simulation method for system reliability and risk analysis*, Springer, 2013, pp. 19–58.

[143] H. Guimarães, J. C. Matos, and A. A. Henriques, "An innovative adaptive sparse response surface method for structural reliability analysis," *Structural Safety*, vol. 73, pp. 12–28, 2018, doi: 10.1016/j.strusafe.2018.02.001.

[144] G. Blatman and B. Sudret, "An adaptive algorithm to build up sparse polynomial chaos expansions for stochastic finite element analysis," *Probabilistic Engineering Mechanics*, vol. 25, no. 2, pp. 183–197, 2010, doi: https://doi.org/10.1016/j.probengmech.2009.10.003.

[145] J. E. Hurtado and D. A. Alvarez, "Neural-network-based reliability analysis: a comparative study," *Comput Methods Appl Mech Eng*, vol. 191, no. 1, pp. 113–132, 2001, doi: https://doi.org/10.1016/S0045-7825(01)00248-1.

[146] J.-M. Bourinet, F. Deheeger, and M. Lemaire, "Assessing small failure probabilities by combined subset simulation and Support Vector Machines," *Structural Safety*, vol. 33, no. 6, pp. 343–353, 2011, doi: https://doi.org/10.1016/j.strusafe.2011.06.001.

[147] I. Kaymaz, "Application of kriging method to structural reliability problems," *Structural Safety*, vol. 27, no. 2, pp. 133–151, 2005, doi: https://doi.org/10.1016/j.strusafe.2004.09.001.

[148] S. A. Argyroudis, S. A. Mitoulis, M. G. Winter, and A. M. Kaynia, "Fragility of transport assets exposed to multiple hazards: State-of-the-art review toward infrastructural resilience," *Reliab Eng Syst Saf*, vol. 191, p. 106567, 2019.

[149] S. Banerjee and G. Ganesh Prasad, "Seismic risk assessment of reinforced concrete bridges in flood-prone regions," *Structure and Infrastructure Engineering*, vol. 9, no. 9, pp. 952–968, 2013.

[150] Y. Dong, D. M. Frangopol, and D. Saydam, "Time-variant sustainability assessment of seismically vulnerable bridges subjected to multiple hazards," *Earthq Eng Struct Dyn*, vol. 42, no. 10, pp. 1451–1467, 2013.

[151] T. Yilmaz, S. Banerjee, and P. A. Johnson, "Uncertainty in risk of highway bridges assessed for integrated seismic and flood hazards," *Structure and infrastructure engineering*, vol. 14, no. 9, pp. 1182–1196, 2018.

[152] C.-C. Hung and W.-G. Yau, "Vulnerability evaluation of scoured bridges under floods," *Eng Struct*, vol. 132, pp. 288–299, 2017.

[153] H. Kim, S.-H. Sim, J. Lee, Y.-J. Lee, and J.-M. Kim, "Flood fragility analysis for bridges with multiple failure modes," *Advances in Mechanical Engineering*, vol. 9, no. 3, p. 1687814017696415, 2017.

[154] T. Ahamed, J. G. Duan, and H. Jo, "Flood-fragility analysis of instream bridges–consideration of flow hydraulics, geotechnical uncertainties, and variable scour depth," *Structure and Infrastructure Engineering*, vol. 17, no. 11, pp. 1494–1507, 2021.

[155] S. A. Argyroudis and S. A. Mitoulis, "Vulnerability of bridges to individual and multiple hazards-floods and earthquakes," *Reliab Eng Syst Saf*, vol. 210, p. 107564, 2021.

[156] C. Mendoza Cabanzo, M. Santamaría, H. S. Sousa, and J. C. Matos, "In-Plane Fragility and Parametric Analyses of Masonry Arch Bridges Exposed to Flood Hazard Using Surrogate Modeling Techniques," *Applied Sciences*, vol. 12, no. 4, p. 1886, 2022.

[157] O. Khandel and M. Soliman, "Integrated framework for assessment of time-variant flood fragility of bridges using deep learning neural networks," *Journal of Infrastructure Systems*, vol. 27, no. 1, p. 4020045, 2021.

[158] E. S. Cavaco, J. R. Casas, L. A. C. Neves, and A. E. Huespe, "Robustness of corroded reinforced concrete structures - a structural performance approach," *Structure and Infrastructure Engineering*, vol. 9, no. 1, pp. 42–58, 2013, doi: 10.1080/15732479.2010.515597.

[159] U. Starossek and M. Haberland, "Approaches to measures of structural robustness," *Structure and Infrastructure Engineering*, vol. 7, no. 7–8, pp. 625–631, 2011.

[160] E. Cavaco, L. A. C. Neves, and J. R. Casas, "Reliability-based approach to the robustness of corroded reinforced concrete structures," *Structural Concrete*, vol. 18, no. 2, pp. 316–325, 2017, doi: 10.1002/suco.201600084.

[161] M. G. Stewart and A. Al-Harthy, "Pitting corrosion and structural reliability of corroding RC structures: Experimental data and probabilistic analysis," *Reliab Eng Syst Saf*, vol. 93, no. 3, pp. 373–382, Mar. 2008, doi: 10.1016/j.ress.2006.12.013.

[162] European Committee for Standardization, *EN 1992-1-2, Eurocode 2: Design of concrete structures - Part 1-2: General rules Structural fire design*. Brussels, Belgium, 2010.

[163] TNO DIANA, *User's Manual - Element Library*, Release 10. Delft, The Netherlands, 2016.

[164] European Committee for Standardization, *EN 1991-2, Eurocode 1: Actions on structures - Part 2: Traffic loads on bridges*. Brussels, Belgium, 2003.

[165] R. Onstein, "Arches, Nonlinear? Investigating the geometrically nonlinear behaviour of arches in 2D.," Delft University of Technology, 2013.

[166] M. Chajes, D. Hall, W. L. Taylor, J. Lewis, S. Wolfe, and R. Taylor, "Load Rating of Arch Bridges," 2002.

[167] European Committee for Standardization, *EN 1991-2, Eurocode 1: Actions on structures - Part 2: Traffic loads on bridges*. Brussels, Belgium, 2003.

[168] J. C. Matos, V. N. Moreira, I. B. Valente, P. J. S. Cruz, L. C. Neves, and N. Galvão, "Probabilistic-based assessment of existing steel-concrete composite bridges – Application to Sousa River Bridge," *Eng Struct*, vol. 181, no. December 2018, pp. 95–110, 2019, doi: 10.1016/j.engstruct.2018.12.006.

[169] N. Galvão, J. C. Matos, D. V Oliveira, and R. Hajdin, "Human error impact in structural safety of a reinforced concrete bridge," *Structure and Infrastructure Engineering*, vol. 0, no. 0, pp. 1–15, 2021, doi: 10.1080/15732479.2021.1876105.

[170] Joint Committee on Structural Safety, *Probabilistic Model Code - Part 3: Material properties*. 2000. doi: 10.1093/jicru/ndm007.

[171] D. F. Wiśniewski, P. J. S. Cruz, A. A. R. Henriques, and R. A. D. Simões, "Probabilistic models for mechanical properties of concrete, reinforcing steel and pre-stressing steel," *Structure and Infrastructure Engineering*, vol. 8, no. 2, pp. 111–123, Feb. 2012, doi: 10.1080/15732470903363164.

[172] A. S. Nowak, A. S. Yamani, and S. W. Tabsh, "Probabilistic models for resistance of concrete bridge," *ACI Struct J*, vol. 91, no. 3, pp. 269–276, 1994, doi: 10.14359/4354.

[173] European Committee for Standardization, *EN 1990, Eurocode 0: Basis of structural design*. Brussels, Belgium, 2002.

[174] M. Sykora, D. Diamantidis, M. Holicky, and K. Jung, "Target reliability for existing structures considering economic and societal aspects," *Structure and Infrastructure Engineering*, vol. 13, no. 1, pp. 181–194, 2017, doi: 10.1080/15732479.2016.1198394.

[175] N. Galvão, J. Matos, D. V Oliveira, and C. Santos, "Assessment of roadway bridges damaged by human errors using risk indicators and robustness index," 2019.

[176] Infraestruturas de Portugal, "Relatório de inspeção principal global [Global main inspection report]," 2020.

[177] A. Arede *et al.*, "Experimental characterization of the mechanical behaviour of components and materials of stone masonry railway bridges," *Constr Build Mater*, vol. 153, pp. 663–681, 2017.

[178] R. Silva, C. Costa, and A. Arede, "Experimental and numerical approaches for calibration of the material parameters used in models of stone masonry railway bridges," in *The Fourth International Conference on Railway Technology*, 2018.

[179] C. Costa, D. Ribeiro, P. Jorge, R. Silva, A. Arêde, and R. Calçada, "Calibration of the numerical model of a stone masonry railway bridge based on experimentally identified modal parameters," *Eng Struct*, 2016, doi: 10.1016/j.engstruct.2016.05.044.

[180] R. Silva, C. Costa, A. Arêde, R. Calçada, and D. V Oliveira, "Structural analysis of a stone arch bridge under incremental railway static loading," 2019.

[181] E. A. Baron, N. Galvão, M. Docevska, J. C. Matos, and G. Markovski, "Application of quality control plan to existing bridges," *Structure and Infrastructure Engineering*, pp. 1–17, 2021.

[182] P. B. Lourenço, "Computations on historic masonry structures," *Progress in Structural Engineering and Materials*, vol. 4, no. 3, pp. 301–319, 2002.

[183] V. dos Santos Adrião, "Modelação numérica da ponte ferroviária em alvenaria de pedra sobre o rio Leça," 2018.

[184] C. C. Rangel, "Evaluación del impacto de las alteraciones climáticas en un puente de concreto preesforzado," Universidade do Minho, 2016.

[185] L. A. V. Carvajal, "Propuesta de plan de monitoreo del comportamiento dinámico para la salud estructural del nuevo puente Gómez Ortiz en la vía Girón-Zapatoca," *Universidad Industrial de Santander*, 2016.

[186] B. Jaishi and W.-X. Ren, "Structural Finite Element Model Updating Using Ambient Vibration Test Results," *Journal of Structural Engineering*, 2005, doi: 10.1061/(ASCE)0733-9445(2005)131:4(617).

[187] L. F. Ramos, J. Sena-Cruz, and R. M. Ferreira, "Caracterização dinâmica da ponte Luiz Bandeira em Sejães," in *2º Congresso de Segurança e Conservação de Pontes (ASCP2011)*, 2011, pp. 143–152.

[188] C. Costa, D. Ribeiro, P. Jorge, R. Silva, A. Arêde, and R. Calçada, "Avaliação experimental e numérica dos parâmetros modais da ponte ferroviária de Durrães," *JPEE 2014, 5as Jornadas Portuguesas de Engenharia de Estruturas*, pp. 26–28, 2014.

[189] R. Silva, C. Costa, and A. Arêde, "Numerical methodologies for the analysis of stone arch bridges with damage under railway loading," *Structures*, vol. 39, no. March, pp. 573–592, 2022, doi: 10.1016/j.istruc.2022.03.063.

[190] B. Conde, J. C. Matos, D. V Oliveira, and B. Riveiro, "Probabilistic-based structural assessment of a historic stone arch bridge," *Structure and Infrastructure Engineering*, vol. 17, no. 3, pp. 379–391, 2021.

[191] B. Conde, L. F. Ramos, D. V. Oliveira, B. Riveiro, and M. Solla, "Structural assessment of masonry arch bridges by combination of non-destructive testing techniques and three-dimensional numerical modelling: Application to Vilanova bridge," *Eng Struct*, vol. 148, pp. 621–638, 2017, doi: 10.1016/j.engstruct.2017.07.011.

[192] P. Zampieri, F. Faleschini, M. A. Zanini, and N. Simoncello, "Collapse mechanisms of masonry arches with settled springing," *Eng Struct*, vol. 156, no. November 2017, pp. 363–374, 2018, doi: 10.1016/j.engstruct.2017.11.048.

[193] J. Hansen, "A revised and extended formula for bearing capacity," 1970, Accessed: Oct. 27, 2022. [Online]. Available: https://trid.trb.org/view/125129

[194] F. Yang, X.-C. Zheng, L.-H. Zhao, and Y.-G. Tan, "Ultimate bearing capacity of a strip footing placed on sand with a rigid basement," *Comput Geotech*, vol. 77, pp. 115–119, 2016.

[195] B. Conde, J. C. Matos, D. v. Oliveira, and B. Riveiro, "Probabilistic-based structural assessment of a historic stone arch bridge," *Structure and Infrastructure Engineering*, vol. 0, no. 0, pp. 1–13, 2020, doi: 10.1080/15732479.2020.1752261.

[196] S. K. Au and J. L. Beck, "Estimation of small failure probabilities in high dimensions by subset simulation," *Probabilistic Engineering Mechanics*, vol. 16, no. 4, pp. 263–277, 2001, doi: 10.1016/S0266-8920(01)00019-4.

[197] JCSS PROBABILISTIC MODEL CODE, "Section 3.7: Soil properties," *JCSS Probabilistic Model Code*, no. August, 2006.

[198] S. Marelli and B. Sudret, "UQLab: a Framework for Uncertainty Quantification in MATLAB," in *The 2nd International Conference on Vulnerability and Risk Analysis and Management (ICVRAM 2014)*, 2014, pp. 2554–2563. doi: 10.1061/9780784413609.257.

[199] NP EN 1990: 2009, "Norma Portuguesa - Eurocódigo 0 - Bases para o projeto de estruturas," *Instituto Português da Qualidade*, vol. 1999, p. 88, 2009.

[200] S. A. Argyroudis, S. Mitoulis, M. G. Winter, and A. M. Kaynia, "Fragility of transport assets exposed to multiple hazards: State-of-the-art review toward infrastructural resilience," *Reliab Eng Syst Saf*, vol. 191, no. December 2018, p. 106567, 2019, doi: 10.1016/j.ress.2019.106567.

[201] O. Khandel and M. Soliman, "Integrated Framework for Assessment of Time-Variant Flood Fragility of Bridges Using Deep Learning Neural Networks," *Journal of Infrastructure Systems*, vol. 27, no. 1, p. 04020045, 2021, doi: 10.1061/(asce)is.1943-555x.0000587.

[202] J. A. Nelder and R. W. M. Wedderburn, "Generalized Linear Models," *J R Stat Soc Ser A*, vol. 135, no. 3, p. 370, 1972, doi: 10.2307/2344614.

[203] P. Zampieri, M. A. Zanini, F. Faleschini, L. Hofer, and C. Pellegrino, "Failure analysis of masonry arch bridges subject to local pier scour," *Eng Fail Anal*, vol. 79, no. May, pp. 371–384, 2017, doi: 10.1016/j.engfailanal.2017.05.028.

ANNEX

ANNEX A – CHAPTER 2

This annex contains the MATLAB code for the flood frequency analysis applying an Artificial Neural Network divided into three different files. i) probabilistic fitting of initial database; ii) ANN training and function definition; iii) results processing.

i) Probabilistic_fitting_forANN.m

```matlab
clear
clc
% Initial data
Pd = xlsread('Datafile');
N = length(Pd);
pf = [0.5 0.9 0.1];
pf3d = zeros(N,3);
Fe = zeros(100,106);
Fe1 = zeros(106,3);
F = zeros(N,1);
F(:,1)=1-((rango)/(N+1));
% Initial matrices
for i = 1:N
    pf3d(i,:) = pf;
end
rango = zeros(N,1);
for i = 1:N
    rango(i) = i;
end
for i=1:3
    Fe1(:,i)=F;
end
for i=1:100
    Fe(i,:)=F(:,1);
end
%Probabilistic fitting
Pf_IM_1=zeros(100,N);
for j=1:N
    x1=evfit(Pd(j,:));
    for i=1:1:100
        Pf_IM_1(i,j)=evcdf(i,x1(1),x1(2));
    end
end
x_graph=zeros(100,106);
x_g=(1:1:100);
```

```matlab
for i=1:106
    x_graph(:,i)=x_g;
end
%Final graphic
figure()
plot3(Fe,x_graph,Pf_IM_1,'o','MarkerSize',0.3,'MarkerEdgeColor','red')
hold on
plot3(Fe1,Pd,pf3d,'o','MarkerSize',1,'MarkerEdgeColor','black')
hold off
xlabel('Probability');
ylabel ('Precipitation');
zlabel('confidance');
```

ii)   myNeuralNetworkFunction_general.m

```matlab
function [y1] = myNeuralNetworkFunction_general(x1)
% ===== NEURAL NETWORK CONSTANTS =====
% Input 1
x1_step1.xoffset = [0.006;0.00934579439252337];
x1_step1.gain = [2.01409869083585;2.03809523809524];
x1_step1.ymin = -1;
b1 = [-0.45711764196304222052;34.621534982910972644;-
0.098057969097652783463;3.0593636825049408401;1.6213763517557204796;-
40.871806665041894746;4.0991478141326913587;0.38677443336019473596;-
2.3233123545412803779;12.086512813794389132;12.378766036745101786;-
12.687079482167261446;-2.9222120820858212831;-6.4723566363931519518;-
5.67838600830334439];
IW1_1 = [0.48389484095001106256 0.38833839272147768762;-
0.020735667377400610056 -32.224579524622733118;0.0041093314747353655234
3.7083860359396347839;1.9773804315390470787 -
0.60427463124486824331;0.28778644314404538962 -
5.3056030379320926471;38.543867674567501069 0.15117713612424507619;-
0.56406844006387812929 -1.7735190862835836789;0.07224160482720685905 -
2.0967440633490461721;-1.5401563116088607952 -
0.39921082477506114605;0.57234814570132797051 -
9.2918548663738373961;0.058930694468588880539 11.056317499781428637;-
0.09521173991884328804 -11.999270753439708059;-1.6004461395708093896 -
0.43878948992985300492;4.4644210593610074156 0.16632819043941610149;-
4.5568453717577872553 -0.31766538688951251324];
% Layer 2
b2 = 2.7410709547947540443;
LW2_1 = [0.62468713280362542228 -5.3771888138359011933 0.10637225606573010028
0.73458601987953042745 -0.061832128552163814761 4.4035723756701434795 -
4.7589202375030126291 0.31878501016148924618 -3.3387909593389548668
7.5767351628749892711 13.623910707589542923 4.4228405093449314478
7.2541189520449842476 3.4133649382879140965 -1.6337680047257794325];
```

```
% Output 1
y1_step1.ymin = -1;
y1_step1.gain = 0.0164443133265896;
y1_step1.xoffset = 0.00199524394307105;
% ===== SIMULATION ========
% Dimensions
Q = size(x1,2); % samples
% Input 1
xp1 = mapminmax_apply(x1,x1_step1);
% Layer 1
a1 = tansig_apply(repmat(b1,1,Q) + IW1_1*xp1);
% Layer 2
a2 = repmat(b2,1,Q) + LW2_1*a1;
% Output 1
y1 = mapminmax_reverse(a2,y1_step1);
end
% ===== MODULE FUNCTIONS ========
% Map Minimum and Maximum Input Processing Function
function y = mapminmax_apply(x,settings)
  y = bsxfun(@minus,x,settings.xoffset);
  y = bsxfun(@times,y,settings.gain);
  y = bsxfun(@plus,y,settings.ymin);
end
% Sigmoid Symmetric Transfer Function
function a = tansig_apply(n,~)
  a = 2 ./ (1 + exp(-2*n)) - 1;
end
% Map Minimum and Maximum Output Reverse-Processing Function
function x = mapminmax_reverse(y,settings)
  x = bsxfun(@minus,y,settings.ymin);
  x = bsxfun(@rdivide,x,settings.gain);
  x = bsxfun(@plus,x,settings.xoffset);
end
```

iii)   ANN_results_processing.m

```
clear
clc
% Initial data
Pd11 = xlsread('P11');
Pd21 = xlsread('P21');
Pd31 = xlsread('P31');
Pd41 = xlsread('P41');
Pd51 = xlsread('P51');
confidence1=0.001:0.005:0.9;
confidence2=0.9:0.001:0.999;
s=length(confidence2)+length(confidence1);
```

```matlab
for i=1:s
    if i<= length(confidence1)
        confidence(i)=confidence1(i);
    else
        confidence(i)=confidence2(i-length(confidence1));
    end
end
N=length(Pd11);
rango=zeros(N,1);
for i=1:N
    rango(i)=i;
end
F=zeros(N,1);
F(:,1)=1-((rango)/(N+1));
Pd11_new=zeros(s,N);
Pd21_new=zeros(s,N);
Pd31_new=zeros(s,N);
Pd41_new=zeros(s,N);
Pd51_new=zeros(s,N);
for j=1:N
    x11=evfit(Pd11(j,:));
    x21=evfit(Pd21(j,:));
    x31=evfit(Pd31(j,:));
    x41=evfit(Pd41(j,:));
    x51=evfit(Pd51(j,:));

    for i=1:1:s
        Pd11_new(:,j)=evinv(confidence,x11(1),x11(2));
        Pd21_new(:,j)=evinv(confidence,x21(1),x21(2));
        Pd31_new(:,j)=evinv(confidence,x31(1),x31(2));
        Pd41_new(:,j)=evinv(confidence,x41(1),x41(2));
        Pd51_new(:,j)=evinv(confidence,x51(1),x51(2));
    end
end
k=1;
for i=1:N
    for j=1:s
        if Pd11_new(j,i)>0
            outputs(k,1)=Pd11_new(j,i);
            inputs(k,1)=confidence(1,j);
            inputs(k,2)=F(i);
            k=k+1;
        end
    end
end
for i=1:N
```

```
    for j=1:s
      if Pd21_new(j,i)>0
        outputs(k,1)=Pd21_new(j,i);
        inputs(k,1)=confidence(1,j);
        inputs(k,2)=F(i);
        k=k+1;
      end
    end
end
for i=1:N
    for j=1:s
      if Pd31_new(j,i)>0
        outputs(k,1)=Pd31_new(j,i);
        inputs(k,1)=confidence(1,j);
        inputs(k,2)=F(i);
        k=k+1;
      end
    end
end
for i=1:N
    for j=1:s
      if Pd41_new(j,i)>0
        outputs(k,1)=Pd41_new(j,i);
        inputs(k,1)=confidence(1,j);
        inputs(k,2)=F(i);
        k=k+1;
      end
    end
end
for i=1:N
    for j=1:s
      if Pd51_new(j,i)>0
        outputs(k,1)=Pd51_new(j,i);
        inputs(k,1)=confidence(1,j);
        inputs(k,2)=F(i);
        k=k+1;
      end
    end
end
a=6.5;
b=0.5;
c=4;
A=189.9;
Tc=12.75;
pf1= [0.5 0.95 0.05 0.8 0.2 0.6 0.4];
Tr=[1.5 2 5 10 50 100 500];
```

```matlab
P=1-(1.*(Tr(:)).^-1);
for j=1:length(pf1)
    for i=1:length(P)
        in=[pf1(j),P(i)];
        in=transpose(in);
        [Z1(i,j)] = myNeuralNetworkFunction_general(in);
        Q(i,j)= (277*a*b*Z1(i,j)*0.001*A)*(c*Tc)^-1;
    end
end
Tr=[1 2 5 10 25 50 100];
Q1=[181.63 265.09 309.83 338.29 371.78];
T1=[2 10 25 50 100];
Q2=[118.25 167.07 204.21 240.13 289.90 337.22];
T2=[2 5 10 20 50 100];
Q3=[183.87 233.65 262.2 295 317.62 339];
T3=[2 5 10 25 50 100];
figure()
area(Tr,Q(:,2),'FaceColor','#d88f8f','EdgeColor','red','LineStyle',':');
hold on
area(Tr,Q(:,4),'FaceColor','#fcce76','EdgeColor','#d48c00','LineStyle',':');
hold on
area(Tr,Q(:,6),'FaceColor','#0ea7ff','EdgeColor','blue','LineStyle',':');
hold on
area(Tr,Q(:,7),'FaceColor','#fcce76','EdgeColor','blue','LineStyle',':');
hold on
area(Tr,Q(:,5),'FaceColor','#d88f8f','EdgeColor','#d48c00','LineStyle',':');
hold on
area(Tr,Q(:,3),'FaceColor','white','EdgeColor','red','LineStyle',':');
hold on
plot(Tr,Q(:,1),"Color",'black','LineWidth',1.5);
hold on
plot(T1,Q1,'LineStyle','--','Marker','o','MarkerFaceColor','red','MarkerEdgeColor','black');
hold on
plot(T2,Q2,'LineStyle','--','Marker','diamond','MarkerFaceColor','red','MarkerEdgeColor','black');
hold on
plot(T3,Q3,'LineStyle','--','Marker','square','MarkerFaceColor','red','MarkerEdgeColor','black','Color','black');
hold off
xlabel('Tr')
ylabel('Q (m^3/s)')
legend('95% confidence','80% confidence','60% confidence','','','','Mean value','Q=aA^b adjusment','Rational method','Rainfall frequency analysis','Location','eastoutside')
[X,Y] = meshgrid(0:0.025:1,0:0.025:1);
m=length(X);
for i=1:m
    for j=1:m
```

145

```
    in=[X(i,j) Y(i,j)];
    in=transpose(in);
    [Z(i,j)] = myNeuralNetworkFunction_general(in);
   end
end
pf= [0.5 0.9 0.1];
pf3d=zeros(N,3);
for i=1:N
   pf3d(i,:)=pf;
end
Fe1=zeros(106,3);
for i=1:3
   Fe1(:,i)=F;
end
surf(Y,Z,X,'FaceAlpha',0.5,'LineStyle',"-")
xlabel('Probability');
ylabel ('Precipitation (mm)');
zlabel('confidance (%)');
```

ANNEX B – CHAPTER 4

This annex contains the MATLAB code for the reliability assessment of the practical cases divided into three different files: i) Generation of random variables using LHS; ii) Data processing from DIANA datafiles results (.tb). iii) Robustness indicator estimation.

i) RandomNormalVariables.m

```matlab
clc
clear
%Example Bridge A
sp = 200;
A=zeros(300,1);
str=string(A);
for i=1:300
    str(i,1)="filename_"+i;
end
%mean=nominal*BIAS
%std^2=mean*COV
%C, D = concreto (fcm, E)
% mean = 43Mpa ---> concreto 35/45
C =lhsnorm (4.3E+01,5.76^2,sp);
%Ecm --> formula eurocodigo
E =lhsnorm((22*((43*0.1)^0.3))*1000,(22*((43*0.1)^0.3))*1000*0.08,sp);
%Ecm para compresion
E04 =(E(:).*0.4);
%fsy
B =lhsnorm (5.6E+02,2.8E+01^2,sp);
%area acero
A1=lhsnorm(2.49364E+03,4.98728E+01^2,sp);
A2=lhsnorm(1.99517E+04,3.99034E+02^2,sp);
M=[str,C,E,E04,B,A1,A2];
xlswrite ('LatinHS1.xlsx',M);
```

ii) DataProcessing_tb.m

```matlab
clc;
clear;
NF=200;
LoadFactorFinal=zeros(NF);
M=zeros(NF);
N=zeros(NF);
for j=1:NF
 %Change output file name
    filenameA = sprintf('%s%d.tb','Portuguese_Bridge2_Analysis',j);
    fid = fopen(filenameA,'rb');
```

```matlab
cellRead = textscan(fid, '%s', 'delimiter', '\n');
fileRead = cellRead{1,1};
emptyCells = cellfun(@isempty,fileRead);
fileRead(emptyCells) = [];
fclose(fid);
q = length (fileRead);
final=zeros(round(q/7),1);
a=4;
d=4;
b=0;
c=3;
while a<q
    for i=1:6
        loadstep=textscan(fileRead{a},'%s');
        loadstep=loadstep{1};
        loadstep1=loadstep{3};
        b=b+1;
        final(b,1) = str2double(loadstep1);
        a=a+d;
        loadstep=textscan(fileRead{a},'%s');
        loadstep=loadstep{1};
        loadstep1=loadstep{3};
        final(b,2) = str2double(loadstep1);
        a=a+c;
        if a>q
            break
        end
    end
    a=a+1;
end
i=2;
k=0;
while i<b
    if final(i,1)<0
        break
    end
    if k==5
        break
    end
    M(i,j)=final(i,1);
    N(i,j)=final(i,2);
    if final(i,1)-final(i-1,1)<0
        k=k+1;
    end
    i=i+1;
end
```

```matlab
        LoadFactorFinal(j)=max(final(:,1));
end
k=1;
l=1;
for i=1:NF
    for j=1:length(M)
        if M(j,i)~=0
            datosLF(k,1)=M(j,i);
            k=k+1;
        end
        if N(j,i)~=0
            datosD(l,1)=N(j,i);
            l=l+1;
        end
    end
end
%Probabilistic Analysis
sq=1000;
z = zeros(1000,NF);
for w =1:NF
    m = LoadFactorFinal(w)*1.2;
    v = (LoadFactorFinal(w)*0.15)^2;
    mu = log((m^2)/sqrt(v+m^2));
    sigma = sqrt(log(v/(m^2)+1));
    z(:,w) = lognrnd (mu,sigma,1,sq);
end
x = zeros(100000:1);
for s = 1:NF
    r = (s-1)*1000;
    for e = 1:1000
        x(r+e,1) = z (e,s);
    end
end
histfit (x,100)
desviacionStandar= std(x)
MediaM= mean(x)
xlabel ('Load Factor','FontName','TimesNewRoman','fontweight','bold');
ylabel ('Frequency','FontName','TimesNewRoman','fontweight','bold');
title ('Probabilistic Load Factor Distribution');
legend ('Histogram','FDP Adjusted')
beta=(MediaM-1)/sqrt((desviacionStandar^2)+(0.15^2))
%scatter(datosD,datosLF);
```

iii)   RobustnessIndicator_discrete.m

```
clc
clear
I45 = [45 45];
R45 = [0 1];
%Bridge A
S1 = [4.68 4.57 4.36 1.06 0];
S2 = [4.61 4.49 3.62 0.67 0];
S3 = [3.89 3.57 1.12 0.31 0];
M1 = [0 15 45 75 100];
M2 = [0 15 45 70 80];
M3 = M2;
plot(M1,S1,M2,S2,M3,S3,'Marker',"*","LineStyle","-","MarkerSize",5)
ylabel('Reliability index [-]');
xlabel ('Damage magnitude [%]');
legend('Scenario 1','Scenario 2', 'Scenario 3');
box 'on'
axis square;
S1 = normalize(S1,"range");
S2 = normalize(S2,"range");
S3 = normalize(S3,"range");
Ir = cumtrapz(M1,S1);
Ir1=[Ir(1,3), Ir(1,5)]
Ir = cumtrapz(M2,S2);
Ir2=[Ir(1,3), Ir(1,5)]
Ir = cumtrapz(M3,S3);
Ir3=[Ir(1,3), Ir(1,5)]
area(M1,S1,'FaceAlpha',0.5)
hold on
area(M2,S2,'FaceAlpha',0.5)
hold on
area(M3,S3,'FaceAlpha',0.25)
hold on
plot(I45,R45,'LineStyle','--','Color','black','LineWidth',0.25)
hold off
ylabel('Reliability index normalized[-]');
xlabel ('Damage magnitude [%]');
legend('Scenario 1','Scenario 2', 'Scenario 3');
box 'on'
axis square;
%Bridge
S1 = [5.35 3.2 1.14 0.49 0];
S2 = [6.05 5.92 4.87 1.43 0.61];
S3 = [4.86 2.34 0.48 0.12 0];
plot(M1,S1,M2,S2,M3,S3,'Marker',"*","LineStyle","-","MarkerSize",5)
ylabel('Reliability index [-]');
```

```matlab
xlabel ('Damage magnitude [%]');
legend('Scenario 1','Scenario 2', 'Scenario 3');
box 'on'
axis square;
S1 = normalize(S1,"range");
S2 = normalize(S2,"range");
S3 = normalize(S3,"range");
Ir = cumtrapz(M1,S1);
Ir1=[Ir(1,3), Ir(1,5)]
Ir = cumtrapz(M2,S2);
Ir2=[Ir(1,3), Ir(1,5)]
Ir = cumtrapz(M3,S3);
Ir3=[Ir(1,3), Ir(1,5)]
area(M1,S1,'FaceAlpha',0.5)
hold on
area(M2,S2,'FaceAlpha',0.5)
hold on
area(M3,S3,'FaceAlpha',0.25)
hold on
plot(I45,R45,'LineStyle','--','Color','black','LineWidth',0.25)
hold off
ylabel('Reliability index normalized[-]');
xlabel ('Damage magnitude [%]');
legend('Scenario 1','Scenario 2', 'Scenario 3');
box 'on'
axis square;
```

ANNEX C – CHAPTER 5

This annex contains the MATLAB code for the reliability assessment of the Leça bridge divided into five different files: i) Data processing from DIANA datafiles considering soil results (.tb) ii) Sampling of random variables applying UQLab library; iii) Machine learning code applying UQLab library iv) probability of failures; v) robustness calculation.

i)   DataProcessingLeçabridge_tb.m

```matlab
clear;
clc;
NF=200;
LoadFactorFinal=zeros(NF);
P=zeros(NF);
O=zeros(NF);
A=zeros(NF);
B=zeros(NF);
for j=1:NF
  %Change output file name
  filenameA = sprintf('%s%d.tb','NumericModel_V2_Analysis',j);
  fid = fopen(filenameA,'rb');
  cellRead = textscan(fid, '%s', 'delimiter', '\n');
  fileRead = cellRead{1,1};
  emptyCells = cellfun(@isempty,fileRead);
  fileRead(emptyCells) = [];
  fclose(fid);
  q = length (fileRead);
  final=zeros(46,1);
  a=4;
  d=8;
  b=0;
  c=15;
  h=54;
  n=0;
  while a<q
    %LoadFactor
    loadstep=textscan(fileRead{a},'%s');
    loadstep=loadstep{1};
    loadstep1=loadstep{3};
    b=b+1;
    final(b,1) = str2double(loadstep1);
    a=a+d;
    if a>h
      h=h+54;
      if n==0
```

```matlab
        n=1;
        a=a+2;
    else
        n=0;
        a=a+1;
    end
end
loadstep=textscan(fileRead{a},'%s');
loadstep=loadstep{1};
loadstep1=loadstep{3};
final(b,2) = str2double(loadstep1);
if final(b,2)>1
    if n==0
        n=1;
        a=a+2;
    else
        n=0;
        a=a+1;
    end
    loadstep=textscan(fileRead{a},'%s');
    loadstep=loadstep{1};
    loadstep1=loadstep{3};
    final(b,2) = str2double(loadstep1);
    h=h+54;
end
%Stress arch
a=a+c;
if a>h
    h=h+54;
    if n==0
        n=1;
        a=a+2;
    else
        n=0;
        a=a+1;
    end
end
loadstep=textscan(fileRead{a},'%s');
loadstep=loadstep{1};
loadstep1=loadstep{3};
final(b,3) = str2double(loadstep1);
%strain soil
a=a+c;
if a>h
    h=h+54;
    if n==0
```

```
            n=1;
            a=a+2;
        else
            n=0;
            a=a+1;
        end
    end
    loadstep=textscan(fileRead{a},'%s');
    loadstep=loadstep{1};
    loadstep1=loadstep{4};
    final(b,4) = str2double(loadstep1);
    %Stress soil
    a=a+c;
    if a>h
        h=h+54;
        if n==0
            n=1;
            a=a+2;
        else
            n=0;
            a=a+1;
        end
    end
    loadstep=textscan(fileRead{a},'%s');
    loadstep=loadstep{1};
    loadstep1=loadstep{4};
    final(b,5) = str2double(loadstep1);
    a=a+7;
    if a>h
        h=h+54;
        if n==0
            n=1;
            a=a+2;
        else
            n=0;
            a=a+1;
        end
    end
    if a>q
        break
    end
end
%arch data
t=1;
while t<46
    if final(t,5)<-0.99
```

```matlab
            LoadFactorFinal(j)=final(t,1);
            break
        end
        t=t+1;
    end
    if LoadFactorFinal(j)==0
        LoadFactorFinal(j)=max(final(:,1));

    end
    if LoadFactorFinal(j)<=1
        LoadFactorFinal(j)=0;
    end
    for i=1:46

        P(i,j)=final(i,2);
        O(i,j)=final(i,3);
    end


end
%plot code
k=0;
l=0;
for i=1:NF
    for j=1:46
        if P(46-j+1,i)~=0
            M(46-k,i)=P(46-j+1,i);
            k=k+1;
        end
        if O(46-j+1,i)~=0
            N(46-l,i)=O(46-j+1,i);
            l=l+1;
        end
    end
    k=0;
    l=0;
end
plot(M,N)
```

ii)   Sampling.m

```matlab
rng(1,'twister')%Controls random number generation
uqlab %starts UQLab
%Random Variables
%Masonry_ElasticityM [MPa]
InputOpts.Marginals(1).Name = 'E_m';
InputOpts.Marginals(1).Type = 'Gaussian';% Uniform/Gaussian/Lognormal
```

```
InputOpts.Marginals(1).Parameters = [2150 215];%Mean std
%Masonry_Cohesion [MPa]
InputOpts.Marginals(2).Name = 'C_m';
InputOpts.Marginals(2).Type = 'Gaussian';% Uniform/Gaussian/Lognormal
InputOpts.Marginals(2).Parameters = [0.450 0.068];%Mean std
%Soil_ElasticityM [MPa]
InputOpts.Marginals(3).Name = 'E_s';
InputOpts.Marginals(3).Type = 'Gaussian';% Uniform/Gaussian/Lognormal
InputOpts.Marginals(3).Parameters = [10000 1000];%Mean std
%Soil_Cohesion [MPa]
InputOpts.Marginals(4).Name = 'C_s';
InputOpts.Marginals(4).Type = 'Gaussian';% Uniform/Gaussian/Lognormal
InputOpts.Marginals(4).Parameters = [0.03 0.005];%Mean std
%Soil_FrictionAngle [Deg]
InputOpts.Marginals(5).Name = 'FA_s';
InputOpts.Marginals(5).Type = 'Gaussian';% Uniform/Gaussian/Lognormal
InputOpts.Marginals(5).Parameters = [20 2];%Mean std
InputOpts.Name = 'independent marginals' ;
myInput = uq_createInput(InputOpts);%Create inputs
uq_print(myInput)%Print
uq_display(myInput)%Graph
```

iii)   MachineLearningCode.m

```
LHS=readmatrix("DIANA_results.xlsx");
sf=[1.6 1.7 1.8 1.9 2 2.10 2.20 2.50 3.0];%Sf values
PD = zeros(9,2);
Y_MC=zeros(10000,9);
for i=0:8
  if i==0
    X=LHS(1:400,1:5);%Random variables
    Y=LHS(1:400,6);%Loading capacity only 4
  end
  if i>=1 && i<7
    X=LHS(100*(3*i)+101:100*(3*i+3)+100,1:5);%Random variables
    Y=LHS(100*(3*i)+101:100*(3*i+3)+100,6);%Loading capacity only 4
  end
  if i==7
    X=LHS(2200:2600,1:5);%Random variables
    Y=LHS(2200:2600,6);%Loading capacity only 4
  end
  if i==8
    X=LHS(100*(3*i)+201:100*(3*i+3)+200,1:5);%Random variables
    Y=LHS(100*(3*i)+201:100*(3*i+3)+200,6);%Loading capacity only 4
  end
  % Define kriging metamodel
```

```matlab
    MetaOpts.Type = 'Metamodel';
    MetaOpts.MetaType = 'Kriging';
    MetaOpts.ExpDesign.Sampling = 'User';
    MetaOpts.ExpDesign.X = X;
    MetaOpts.ExpDesign.Y = Y;
    % Create kriging metamodel matern-5_2
    myKriging = uq_createModel(MetaOpts);
    % Print and display matern-5_2
    uq_print(myKriging)
    X_MC =uq_getSample(10000, 'MC');%Sampling
    Y_MC(:,i+1) = uq_evalModel(myKriging,X_MC);%Evaluate model
    pd = fitdist(Y_MC(:,i+1),'ev')
    parmhat = evfit(Y_MC(:,i+1))
    PD(i+1,1)=parmhat(1,1);
    PD(i+1,2)=parmhat(1,2);
end
figure
subplot(3,3,1)
histfit(Y_MC(:,1),40,'kernel')
title('Sf = 1.6 m')
subplot(3,3,2)
histfit(Y_MC(:,2),40,'ev')
title('Sf = 1.7 m')
subplot(3,3,3)
histfit(Y_MC(:,3),40,'ev')
title('Sf = 1.8 m')
subplot(3,3,4)
histfit(Y_MC(:,4),40,'generalized extreme value')%
title('Sf = 1.9 m')
subplot(3,3,5)
histfit(Y_MC(:,5),40,'ev')
title('Sf = 2.0 m')
subplot(3,3,6)
histfit(Y_MC(:,6),40,'generalized extreme value')%
title('Sf = 2.1 m')
subplot(3,3,7)
histfit(Y_MC(:,7),40,'generalized extreme value')
title('Sf = 2.2 m')
subplot(3,3,8)
histfit(Y_MC(:,8),40,'ev')
title('Sf = 2.5 m')
subplot(3,3,9)
histfit(Y_MC(:,9),40,'generalized extreme value')%
title('Sf = 3.0 m')
```

iv) ProbabilityofFailure.m

```matlab
ModelOpts1.mString = 'X(:,1) - X(:,2)';
ModelOpts1.isVectorized = true;
myModel = uq_createModel(ModelOpts1);
InputOpts1.Marginals(1).Name = 'R';
InputOpts1.Marginals(1).Type = 'KS';% Gumbel
InputOpts1.Marginals(1).Parameters = Y_MC(:,1);
InputOpts1.Marginals(2).Name = 'S';
InputOpts1.Marginals(2).Type = 'Gaussian';% Uniform/Gaussian/Lognormal
InputOpts1.Marginals(2).Parameters = [1 0.15];%Mean std
myInput = uq_createInput(InputOpts1);%Create inputs
uq_print(myInput)%Print
uq_display(myInput)%Graph
SubsetSimOpts.Type = 'Reliability';
SubsetSimOpts.Method = 'Subset';
SubsetSimAnalysis = uq_createAnalysis(SubsetSimOpts);
uq_print(SubsetSimAnalysis)
uq_display(SubsetSimAnalysis)
B_Result=SubsetSimAnalysis.Results;
B(1)=B_Result.Beta;
Pf(1)=B_Result.Pf;
InputOpts2.Marginals(1).Name = 'R';
InputOpts2.Marginals(1).Type = 'Gumbel';% Gumbel
InputOpts2.Marginals(1).Moments = [PD(2,1) PD(2,2)];
InputOpts2.Marginals(2).Name = 'S';
InputOpts2.Marginals(2).Type = 'Gaussian';% Uniform/Gaussian/Lognormal
InputOpts2.Marginals(2).Parameters = [1 0.15];%Mean std
myInput = uq_createInput(InputOpts2);%Create inputs
uq_print(myInput)%Print
uq_display(myInput)%Graph
SubsetSimOpts.Type = 'Reliability';
SubsetSimOpts.Method = 'Subset';
SubsetSimAnalysis = uq_createAnalysis(SubsetSimOpts);
uq_print(SubsetSimAnalysis)
uq_display(SubsetSimAnalysis)
B_Result=SubsetSimAnalysis.Results;
B(2)=B_Result.Beta;
Pf(2)=B_Result.Pf;
InputOpts3.Marginals(1).Name = 'R';
InputOpts3.Marginals(1).Type = 'Gumbel';% Gumbel
InputOpts3.Marginals(1).Moments = [PD(3,1) PD(3,2)];
InputOpts3.Marginals(2).Name = 'S';
InputOpts3.Marginals(2).Type = 'Gaussian';% Uniform/Gaussian/Lognormal
InputOpts3.Marginals(2).Parameters = [1 0.15];%Mean std
myInput = uq_createInput(InputOpts3);%Create inputs
```

```matlab
uq_print(myInput)%Print
uq_display(myInput)%Graph
SubsetSimOpts.Type = 'Reliability';
SubsetSimOpts.Method = 'Subset';
SubsetSimAnalysis = uq_createAnalysis(SubsetSimOpts);
uq_print(SubsetSimAnalysis)
uq_display(SubsetSimAnalysis)
B_Result=SubsetSimAnalysis.Results;
B(3)=B_Result.Beta;
Pf(3)=B_Result.Pf;
InputOpts4.Marginals(1).Name = 'R';
InputOpts4.Marginals(1).Type = 'Gumbel';% Gumbel
InputOpts4.Marginals(1).Moments = [PD(4,1) PD(4,2)];
InputOpts4.Marginals(2).Name = 'S';
InputOpts4.Marginals(2).Type = 'Gaussian';% Uniform/Gaussian/Lognormal
InputOpts4.Marginals(2).Parameters = [1 0.15];%Mean std
myInput = uq_createInput(InputOpts4);%Create inputs
uq_print(myInput)%Print
uq_display(myInput)%Graph
SubsetSimOpts.Type = 'Reliability';
SubsetSimOpts.Method = 'Subset';
SubsetSimAnalysis = uq_createAnalysis(SubsetSimOpts);
uq_print(SubsetSimAnalysis)
uq_display(SubsetSimAnalysis)
B_Result=SubsetSimAnalysis.Results;
B(4)=B_Result.Beta;
Pf(4)=B_Result.Pf;
InputOpts5.Marginals(1).Name = 'R';
InputOpts5.Marginals(1).Type = 'Gumbel';% Gumbel
InputOpts5.Marginals(1).Moments = [PD(5,1) PD(5,2)];
InputOpts5.Marginals(2).Name = 'S';
InputOpts5.Marginals(2).Type = 'Gaussian';% Uniform/Gaussian/Lognormal
InputOpts5.Marginals(2).Parameters = [1 0.15];%Mean std
myInput = uq_createInput(InputOpts5);%Create inputs
uq_print(myInput)%Print
uq_display(myInput)%Graph
SubsetSimOpts.Type = 'Reliability';
SubsetSimOpts.Method = 'Subset';
SubsetSimAnalysis = uq_createAnalysis(SubsetSimOpts);
uq_print(SubsetSimAnalysis)
uq_display(SubsetSimAnalysis)
B_Result=SubsetSimAnalysis.Results;
B(5)=B_Result.Beta;
Pf(5)=B_Result.Pf;
InputOpts6.Marginals(1).Name = 'R';
InputOpts6.Marginals(1).Type = 'Gumbel';% Gumbel
InputOpts6.Marginals(1).Moments = [PD(6,1) PD(6,2)]; InputOpts6.Marginals(2).Name = 'S';
```

```
InputOpts6.Marginals(2).Type = 'Gaussian';% Uniform/Gaussian/Lognormal
InputOpts6.Marginals(2).Parameters = [1 0.15];%Mean std
myInput = uq_createInput(InputOpts6);%Create inputs
uq_print(myInput)%Print
uq_display(myInput)%Graph
SubsetSimOpts.Type = 'Reliability';
SubsetSimOpts.Method = 'Subset';
SubsetSimAnalysis = uq_createAnalysis(SubsetSimOpts);
uq_print(SubsetSimAnalysis)
uq_display(SubsetSimAnalysis)
B_Result=SubsetSimAnalysis.Results;
B(6)=B_Result.Beta;
Pf(6)=B_Result.Pf;
InputOpts7.Marginals(1).Name = 'R';
InputOpts7.Marginals(1).Type = 'Gumbel';% Gumbel
InputOpts7.Marginals(1).Moments = [PD(7,1) PD(7,2)];
InputOpts7.Marginals(2).Name = 'S';
InputOpts7.Marginals(2).Type = 'Gaussian';% Uniform/Gaussian/Lognormal
InputOpts7.Marginals(2).Parameters = [1 0.15];%Mean std
myInput = uq_createInput(InputOpts7);%Create inputs
uq_print(myInput)%Print
uq_display(myInput)%Graph
SubsetSimOpts.Type = 'Reliability';
SubsetSimOpts.Method = 'Subset';
SubsetSimAnalysis = uq_createAnalysis(SubsetSimOpts);
uq_print(SubsetSimAnalysis)
uq_display(SubsetSimAnalysis)
B_Result=SubsetSimAnalysis.Results;
B(7)=B_Result.Beta;
Pf(7)=B_Result.Pf;
InputOpts8.Marginals(1).Name = 'R';
InputOpts8.Marginals(1).Type = 'Gumbel';% Gumbel
InputOpts8.Marginals(1).Moments = [PD(8,1) PD(8,2)];
InputOpts8.Marginals(2).Name = 'S';
InputOpts8.Marginals(2).Type = 'Gaussian';% Uniform/Gaussian/Lognormal
InputOpts8.Marginals(2).Parameters = [1 0.15];%Mean std
myInput = uq_createInput(InputOpts8);%Create inputs
uq_print(myInput)%Print
uq_display(myInput)%Graph
SubsetSimOpts.Type = 'Reliability';
SubsetSimOpts.Method = 'Subset';
SubsetSimAnalysis = uq_createAnalysis(SubsetSimOpts);
uq_print(SubsetSimAnalysis)
uq_display(SubsetSimAnalysis)
B_Result=SubsetSimAnalysis.Results;
B(8)=B_Result.Beta;
```

```matlab
Pf(8)=B_Result.Pf;
InputOpts9.Marginals(1).Name = 'R';
InputOpts9.Marginals(1).Type = 'Gumbel';% Gumbel
InputOpts9.Marginals(1).Moments = [PD(9,1) PD(9,2)];
InputOpts9.Marginals(2).Name = 'S';
InputOpts9.Marginals(2).Type = 'Gaussian';% Uniform/Gaussian/Lognormal
InputOpts9.Marginals(2).Parameters = [1 0.15];%Mean std
myInput = uq_createInput(InputOpts9);%Create inputs
uq_print(myInput)%Print
uq_display(myInput)%Graph
SubsetSimOpts.Type = 'Reliability';
SubsetSimOpts.Method = 'Subset';
SubsetSimAnalysis = uq_createAnalysis(SubsetSimOpts);
uq_print(SubsetSimAnalysis)
uq_display(SubsetSimAnalysis)
B_Result=SubsetSimAnalysis.Results;
B(9)=B_Result.Beta;
Pf(9)=B_Result.Pf;

plot(sf,B,'Marker',"*","LineStyle","-","MarkerSize",5)
ylabel('Reliability index [-]');
xlabel ('Scour depth [m]');
box 'on'
axis square;
%ticks off
set(gca,'Ticklength',[0 0])
%white background
set(gcf,'color','w');
```

v)   RobustnessCalculation.m

```matlab
B1=zeros(10,1);
sf1=zeros(10,1);
B1(1,1)=15.8031; %Virgin reliability index
sf1(1,1)=0;
for i=1:9
    B1(i+1,1)=B(i);
    sf1(i+1,1)=(sf(i)/3)*100;
end
B_Normalized=normalize(B1,'range');
[logitCoef,dev] =glmfit(sf1,B_Normalized,"binomial","link","comploglog");
%[logitCoef,dev] = glmfit(sf1,B_Normalized,'binomial','link','probit');
logitFit = glmval(logitCoef,sf1,"comploglog");
prueba = 0:100;
logitFit = glmval(logitCoef,prueba,"comploglog");
Ir = cumtrapz(prueba,logitFit);
Ir1=[Ir(46,1), Ir(101,1)]
```

```matlab
plot(prueba,logitFit,'Color','black')
hold on
area(prueba,logitFit,'FaceAlpha',0.25,'FaceColor','blue','EdgeColor','none');
hold on
plot(sf1,B_Normalized,'LineStyle','none','Marker','o','MarkerFaceColor','red','MarkerEdgeColor','black','MarkerSize',4.2)
hold off
ylabel('Reliability index [-]');
xlabel ('Damage magnitude [%]');
axis([0 100 0 1.05])
legend('GLM fitting fuction','','adjusted data')
plot(sf1,B_Normalized,'Marker','o','MarkerFaceColor','red','MarkerEdgeColor','black','MarkerSize',4.2);
ylabel('Reliability index [-]');
xlabel ('Damage magnitude [%]');
axis([0 100 0 1.05])
for i=1:9
   xverts(1,i)=sf1(i);
   xverts(2,i)=sf1(i);
   xverts(3,i)=sf1(i+1);
   xverts(4,i)=sf1(i+1);
   yverts(1,i)=0;
   yverts(2,i)=B_Normalized(i);
   yverts(3,i)=B_Normalized(i+1);
   yverts(4,i)=0;
end
p = patch(xverts,yverts,'b','LineWidth',0.5,'FaceAlpha',0.25,'EdgeAlpha',0.25,'LineStyle','--');
Ir = trapz(sf1,B_Normalized)
I45 = [45 45];
R45 = [0 1];
plot(sf1,B_Normalized,'LineStyle','none','Marker','o','MarkerFaceColor','red','MarkerEdgeColor','black','MarkerSize',4.2)
hold on
area(sf1,B_Normalized,'FaceAlpha',0.5)
hold on
plot(I45,R45,'LineStyle','--','Color','black','LineWidth',0.25)
hold off
ylabel('Reliability index normalized[-]');
xlabel ('Damage magnitude [%]');
box 'on'
axis square;
```